EXPERIMENTAL STUDY ON HUMAN ARM REACHING WITH AND WITHOUT A REDUCED MOBILITY FOR APPLICATIONS IN MEDICAL HUMAN-INTERACTIVE ROBOTICS

A Dissertation

by

HYO-SANG MOON

Submitted to the Office of Graduate and Professional Studies of
Texas A&M University
in partial fulfillment of the requirements for the degree of

DOCTOR OF PHILOSOPHY

Chair of Committee,	Reza Langari
Co-Chair of Committee,	Nina P. Robson
Committee Members,	Swaroop V. Darbha
	John J. Buchanan
Head of Department,	Andreas Polycarpou

August 2014

Major Subject: Mechanical Engineering

ABSTRACT

Along with increasing advances in robotic technologies, there are now significant efforts under way to improve the quality of life especially those with physical disabilities or impairments. Control of such medical human-interactive robotics (HIR) involves complications in its design and control due to uncertain human factors. This dissertation makes its efforts to resolve three main challenges of an advanced HIR controller development: 1) detecting the operator's motion intent, 2) understanding human motor behavior from the robotic perspective, and 3) generating reference motion for the HIR. Our interests in such challenges are limited to the point-to-point reaching of the human arm for applications of their solutions in the control of rehabilitation exoskeletons, therapeutic haptic devices, and prosthetic arms.

In the context of human motion intent detection, a mobile motion capture system (MCS) enhanced with myoprocessors is developed to capture kinematics and dynamics of human arm in reaching movements. The developed MCS adopts wireless IMU (inertial measurement unit) sensors to capture ADL (activities of daily life) motions in the real-life environment. In addition, measured muscle activation patterns from selected muscle groups are converted into muscular force values by myoprocessors. This allows a reliable motion intent detection by quantify one of the most frequently used driving signal of the HIR, EMG (electromyography), in a standardized way.

In order to understand the human motor behavior from the robotic viewpoint, a computational model on reaching is required. Since such model can be constituted by

experimental observations, this dissertation look into invariant motion features of reaching with and without elbow constraint condition to establish a foundation of the computational model.

The HIR should generate its reference motions by reflecting motor behavior of the natural human reaching. Though the accurate approximation of such behavior is critical, we also need to take into account the computational cost, especially for real-time applications such as the HIR control. In this manner, a higher order kinematic synthesis of mechanical linkage systems is adopted to approximate natural human hand profiles.

Finally, a novel control concept of a myo-prosthetic arm is proposed as an application of all findings and efforts made in this dissertation.

DEDICATION

To my mother, Hyesook Kong, in loving memory of her.

ACKNOWLEDGEMENTS

First, I thank God who allows me a talent in engineering and science to accomplish this research. For his everlasting guidance and grace on my life, I would like to glorify him by continuous dedication to solve various engineering problems that can make this world better.

I would like to thank my committee chair, Dr. Langari, co-chair, Dr. Robson and my committee members, Dr. Buchanan and Dr. Swaroop, for their guidance and support throughout the course of this research.

Thanks also go to my church, Korean church of A&M. It was a great experience for me to live a faithful life with my church friends and to take care of each other as a spiritual union. I also want to extend my gratitude to all my friends in my lab, in Texas A&M University and in my home country Korea.

Finally, thanks to my father Hojoon Moon and my sister Hyojin Moon for their endless love and encouragement and to my fiancée Yeonhee Kim for her patience and unconditional love.

NOMENCLATURE

ADL	Activities of Daily Life
ALPF	Adaptive Low-Pass Filter
BCI	Brain-Computer Interface
BMI	Brain Machine Interface
CNS	Central Nervous System
COM	Center of Mass
DOF	Degrees of Freedom
EC	Elbow Constraint
EEG	Electroencephalogram
EMG	Electromyogram
ENU	Earth North Up
ETC	Extrinsic Task Coordinates
FQA	Factored Quaternion Algorithm
HIR	Human-Interactive Robotics
HPLI	Hand Path Length Index
IJC	Intrinsic Joint Coordinates
INS	Inertial Navigation System
IMU	Inertial Measurement Unit
KTR	Kinetic Torque Ratio
LKE	Least Kinematic Effort

MCP	Motor Coordination Principles
MCS	Motion Capture System
MJ	Minimum Jerk
MRSE	Mean of Root Squared Error
NC	Non-Constraint
NAP	Neural Activation Pattern
NED	North East Down
NLP	Number of Local Peak
OSM	Obstacle Set Method
PCC	Pearson's Correlation Coefficient
PL	Power Law
ROM	Range of Motions
SID	Dissimilarity Index
TMR	Targeted Muscle Reinnervation
TVCF	Time Varying Complementary Filter
UV	Unexplained Variance
VHP	Visible Human Project
VR	Virtual Reality
ZC	Zero Crossing

TABLE OF CONTENTS

Page

LIST OF FIGURES

Page

LIST OF TABLES

Page

1. INTRODUCTION

1.1. Overview on the Human Interactive Robotics for Medical Purposes

Along with increasing advances in robotic technologies, there are now significant efforts under way to improve the quality of life especially of those with physical disabilities or impairments. The human interactive robotics (HIR) is an emerging field of study that enables a human body to restore or to augment motor capabilities via physical interactions with a robotic system. Rehabilitation exoskeletons, advanced artificial limbs and end-effector type haptic devices for therapeutic purposes are representative applications of the HIR in physical therapy and medicine. Though each of their specific functions and technical details are different, they all fall into the medical HIR category under a common purpose: restoration of a subject's damaged motor functions that are essential for one's activities of daily life (ADL).

From walking to dexterous hand manipulations, there are a number of core motor functions that are necessary to sustain a human subject's independent ADL. As we categorize such motor functions into their major roles, lower limb motor activities such as walking, ascending/descending stairs, sitting and standing contribute to the mobility portion of the ADL, while the upper limb motor functions take charge in the actual task portion. Due to their periodic characteristics, mobility functions can be modeled as repetitive cycles of patterned motor primitives (e.g., walking as a repetition of a gait cycle). On the other hand, the actual task portion of the ADL are more arbitrary compared to the mobility portion to meet complicated task requirements in the ADL with enough

versatility. Upper limb tasks are generally initiated by an arm reaching that maneuvers the end-effector (i.e., the hand) to the targeting location and end up with detailed and dexterous hand manipulations such as grasping. This dissertation limits its all interests and efforts in arm reaching motions for exploring human motor coordination principles that enables the central nervous system (CNS) to perform versatile and natural reaching movements in an optimal fashion against complex redundant mapping problems.

Every HIR involves two independent system loops (i.e., a musculoskeletal system controlled by the human CNS and a robotic system controlled by its own controller) coupled together as shown in Figure 1. It makes additional complications in the HIR's design compared to the conventional robotics due to the human related factors that need to be taken into account for safety and comfort reasons. For example, biomechanics of human body and ergonomics can help an upper limb exoskeleton design to allow natural arm reaching movements within anatomical joint range of motions (ROM). Nef *et al*., [1] modeled the shoulder girdle motion as a function of the humeral elevation angle to allow for their exoskeleton to closely mimic the natural human *shoulder complex* kinematics.

The problem becomes even more complex in the HIR's control since the robotic controller needs to achieve desired motion kinematics and dynamics under the presence of the uncertain human motion that can either be a reference or a disturbance to the robotic control loop. For example, a sensed human motion kinematics can be a reference signal for the HIR controller to generate synergistic movements in assistive robotic applications while the same human motion may be considered as an involuntary disturbance that needs to be attenuated in rehabilitation robots. Challenges in control of the HIR can be addressed

as how to: 1) determine the targeting motion effects in accordance to the detailed purpose of the device (e.g., assistance, rehabilitation or augmentation), 2) induce the desired motion kinematics and dynamics of the human loop by physical interactions that are indirect to sense and control, and 3) realize the desired robotic motion kinematics and dynamics against mechanical impedance of the robotic hardware. In the following subsection, state of the art HIR applications in physical therapy and medicine are introduced. Also, a survey on previous efforts to resolve such challenges in the HIR control is presented.

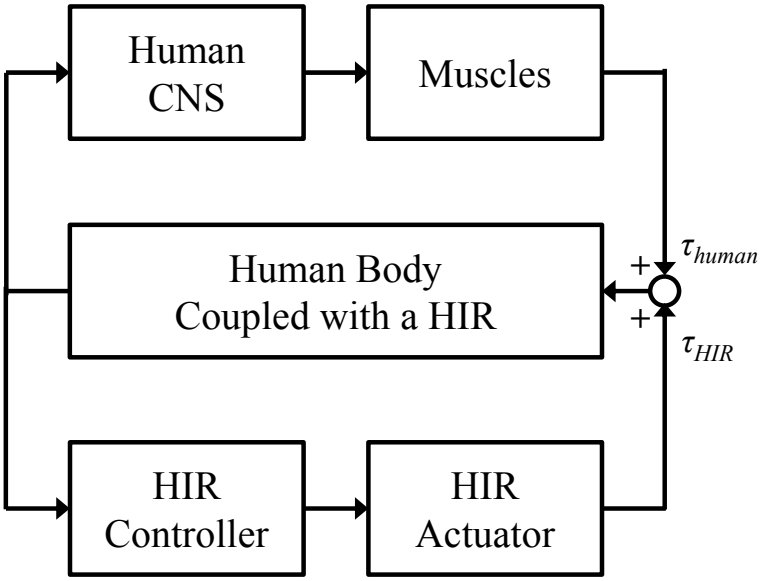

Figure 1. Conceptual control structure of a HIR (modified from [2])

1.2. State of the Art: Survey on Medical HIR Applications and Their Control

1.2.1. End-effector type rehabilitation robots

The haptic master, a 3 degrees-of-freedom(DOF) robot, is implemented in the GENTLE/S neuro-rehabilitation system (see Figure 2(a)) and is designed to apply a force to the human arm [3, 4]. Two ropes hold the weight of the forearm and upper arm against gravity while the wrist's position is controlled by admittance control. MIT-MANUS is the most commonly used arm therapy robot developed by Hogan *et al*., [5]. This device enables shoulder and elbow joint motions on the horizontal plane by employing impedance control. It has been clinically evaluated in studies with more than 100 stroke patients [6-9]. For its commercial version, two separate systems are developed for assisting arm and wrist motions (see Figure 2(b) and Figure 2(c)).

(a) GENTLE/S [3] **(b) InMotion Arm [10]** **(c) InMotion Wrist [11]**

Figure 2. End-effector type rehabilitation robots

1.2.2. Exoskeleton type rehabilitation robots

Recently, the interest in the medical HIR research has shifted towards exoskeleton type systems due to their ability to target controlled force/torque on specific joints or muscles

for training. Lo and Xie [12] have reviewed the work on state of the art in upper-limb exoskeletons. As shown in Figure 3(a), ArmeoSpring (Hocoma AG, Switzerland) is the commercialized version of T-WREX (Therapy Wilmington Robotic Exoskeleton) developed by Sanchez *et al*., [13]. This ergonomically designed passive system is integrated with springs for the arm weight support. By the installed kinematic and force sensors, the patients can train their arm motions in the virtual reality (VR) environment with immediate performance feedback.

ArmeoPower (Hocoma AG, Switzerland) is the most advanced commercialized exoskeleton for upper limb neuro-rehabilitation (see Figure 3(b)). It is the commercialized version of ARMin III which has 7 active DOF controlled by electric motors. In order to realize a natural human arm motion, it is designed to follow not just the glenohumeral joint motion but also the shoulder girdle (i.e. inner shoulder) motions based on the anatomical kinematics of human shoulder complex [1]. For its so-called *path control*, a reference trajectory is computed according to the minimum angular jerk model; then a virtual force tunnel is generated along the trajectory, which guides the patient's motion [14]. The reaching and/or hand trainings are formulated as an ADL simulation within a VR environment to induce the patient's motivation and to maximize the generalized motor recovery.

Among other exoskeleton developments, Perry *et al*., [15] developed a 7-DOF upper limb exoskeleton CADEN-7 (see Figure 3(c)) which is driven by an electric motor with cables and pulleys for each joint actuation. In order to control this machine according to the subject's intention, EMG (electromyography) signal is captured from the subject's

muscles relevant to the joint DOF motions and the muscular force is estimated from the developed real-time myo-processor, which is an adapted version of the Hill-based muscle model [16, 17].

RUPERT IV (Robotic Upper Extremity Repetitive Trainer) is a light-weight upper extremity exoskeleton to assist repetitive therapy tasks related to ADL [18] (see Figure 3(d)). Although this device does not provide gravity compensation, due to its light-weight and portability, it is expected to be worn very easily. Also the developers insist that absence of gravity compensation would be more realistic for patients to train real ADL. From a safety perspective, pneumatic muscle actuators are implemented to drive five joint DOF (i.e. shoulder elevation, humeral external rotation, elbow flexion, forearm supination and wrist extension) and a closed loop controller combining a PID-based feedback controller and a ILC (Iterative Learning Controller)-based feed forward controller is designed to produce the required motion.

GA (Maryland-Georgetown-Army) Exoskeleton depicted in Figure 3(e), is a haptic interface for functional training in VR environment [19]. In its design, scapula rotation DOF is considered to maximize the shoulder range of motion by mimicking the elevation/depression of the shoulder girdle. Each joint motion is controlled independently via sub-controllers, which can be operated in impedance, admittance or position mode.

MEDARM (see Figure 3(f)) is an upper limb robotic exoskeleton for rehabilitation of stroke patients [20]. In its design stage, the developers considered that the failure to replicate the shoulder girdle motion is a major contributor of limited functions of existing upper limb rehabilitation exoskeletons. Therefore, they employed 2 additional DOF on the

shoulder mechanism to realize the sternoclavicular joint motions (i.e. a total of 5 DOF in the shoulder mechanism: 2 DOF for sternoclavicular motion and 3 DOF for glenohumeral joint).

Most rehabilitation robots are focused on the restoration of proximal DOF (i.e. shoulder and elbow) functions. Although sophisticated hand functions are required to complete the ADL, the control on the muscle contractions related to the hand DOFs does not get enough attention in the design of rehabilitation robots. IntelliArm (see Figure 3(g)) is designed to control the whole arm motion including hand opening and closing mechanism [21]. It has four active DOFs and two passive DOFs at shoulder: 3 active DOFs for glenohumeral joint motion, 1 active DOF for the vertical displacement of the gelnohumeral center, 2 passive DOFs for anterior/posterior and medial/lateral displacement of the glenohumeral center. As the research team stressed the importance of hand functional restoration, one active DOF was designed to drive the synchronized hand opening/closing motion.

Unlike the other exoskeletons, mPower arm brace (see Figure 3(h)) is more focused on the lightweight and portable aspects of rehabilitation or assistive device rather than whole arm training with intricate design and control [22]. This elbow brace type exoskeleton weighs 846 grams (1 lbs 14 oz) and it captures EMG signal from the subject's biceps and triceps muscles to determine the assistive torque for the elbow flexion/extension motion.

(a) ArmeoSpring [23]

(b) ArmeoPower [23] and ARMin III [14]

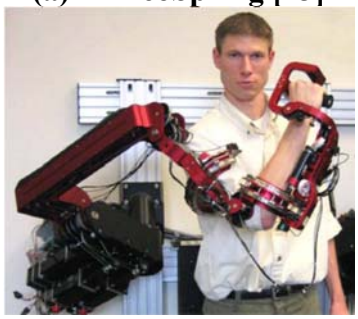

(c) CADEN-7 [15]

(d) RUPERT IV [18]

(e) MGS Exoskeleton [19]

(f) MEDARM [20]

(g) IntelliArm [21]

(h) mPower arm brace [22]

Figure 3. Exoskeleton type rehabilitation robots

1.2.3. Prosthetic limbs

In order to restore missing limb functions and improve the amputees' quality of life, better designs and controls of artificial limbs were constantly studied. In the design perspective, general objectives are 1) compensating missing limbs' DOF, 2) sufficient load bearing, 3) safety guaranteed motion, 4) light weight and 5) cosmesis. Advanced material and

mechanical design techniques allowed some leading groups to develop the state–of–the–art upper limb prostheses.

The Luke–Arm developed by the DEKA Corporation is shown in Figure 4(a). The device, which was named after the Luke Skywalker in the movie Star Wars, has 18 DOF to enable natural human arm and hand motions, and it weighs only 3.6 Kg [24]. The initial version adopted both EMG electrodes and mechanical switches fit into the user's shoe sole to control the device. Later version incorporated more advanced control technology, targeted muscle reinnervation, by cooperating with a medical team in Rehabilitation Institute of Chicago [25].

(a) Luke-arm

(b) Modular Prosthetic Limb (MPL)

Figure 4. Advanced prosthetic arms

The Modular Prosthetic Limb (MPL) developed by the Johns Hopkins University Applied Physics Laboratory (APL) has 22 DOF, which is identical to the human natural limb's DOF (see Figure 4(b)) [26]. The MPL offers nearly as much dexterity as a natural human limb including independent movement of each finger while it weighs only 9 pounds (i.e. close to natural limb weight). As a next level, APL has developed implantable micro–arrays to capture a brain signal from motor cortex region.

1.2.4. Control algorithms involving detection of the human motion intent

One of fundamental concerns that the control of the HIR is on capturing the operator's intention: capturing what action the human operator is trying to do and how the HIR can help this action in a rehabilitation manner. To resolve this concern, a variety of sensor modalities, such as gaze tracking [27], vision tracking [28], force sensing [29], electromyogram (EMG) [30, 31] and electroencephalogram (EEG) [32], have been studied by multiple research groups. For examples, the gaze tracking and the machine vision can help to identify a position of a targeting object that the patient is trying to reach while force sensors can measure the magnitude and the direction of interactive forces that contains the patient's motion intent. Similar information can be acquired from bio-potential signals such as, EMG and EEG. The EMG signal represents muscle activities that its magnitude is proportional to the muscle's voluntary contraction force value [33]. For this reason, many HIR systems adopt multi channels of the EMG signal to generate a control command in accordance to the human subject's voluntary motion intent that is projected on one's skeletal muscles [34]. Also, brain wave signals (EEG) can be used to

extract the motion intent by analyzing patterns of electrical potentials arise on motor cortex area.

Novak and Riener [27] implemented a gaze tracking technology to identify a targeting object in reaching actions (see Figure 5(a)). In this research, it is assumed that human subjects would make their gaze to stay on their point of interest in their visual field, i.e., a targeting object. With this assumption, the targeting object position is defined in a virtual reality (VR) environment by projecting the captured gaze direction. Once the targeting position is defined in the VR, the exoskeleton robot guides the human operator's motion to reach to the captured targeting position.

Loconsole *et al*., [28] adopt a machine vision technique to perform reaching motions with their exoskeleton, L-Exos, in the real environment instead of a VR (see Figure 5(b)). In the proposed system, a Microsoft Kinect sensor and a machine vision algorithm is utilized to capture the scene and to extract object features. This enables the exoskeleton to localize and to track the 3D position of the targeting object in the capturing scene. The captured 3D position of the targeting object is computed in the robot's coordinate system to control the exoskeleton to provide guidance forces.

Gopura and Kiguchi [30] adopted EMG signals from selected muscles to control their 3-DOF upper limb exoskeleton (see Figure 5(c)). In order to generate assistive torques in accordance to the operator's motion intent, the root mean square (RMS) of EMG signals were used to determine the input to a fuzzy-neuro controller. The implemented neural network was designed to be adaptive to resolve the EMG signal's different characteristics for different subjects.

In order to detect the subject's intentional reaching direction, Huo *et al*., [29] utilized force transducers to avoid some disadvantages of EMG signals: 1) the performance of surface EMG sensors is vulnerable to surrounding changes such as, the perspiration and the position of electrodes, and 2) relatively complex signal processing architecture of EMG signals. Their proposed system includes force sensing resisters (FSR) on the inner surface of each wearable ring (or brace) where physical interactions occur. Contacting forces that are captured from the FSR are used to identify the human operator's intentional reaching direction.

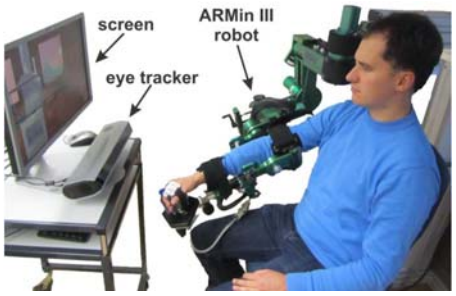

(a) ARMin III with eye tracker [27]

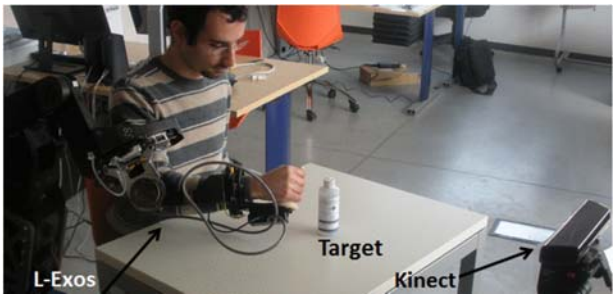

(b) L-Exos and Kinect [28]

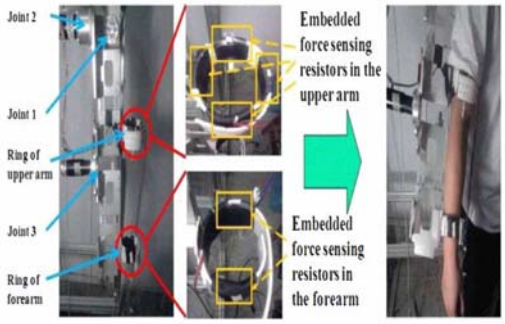

(c) Exoskeleton with FSRs [30]

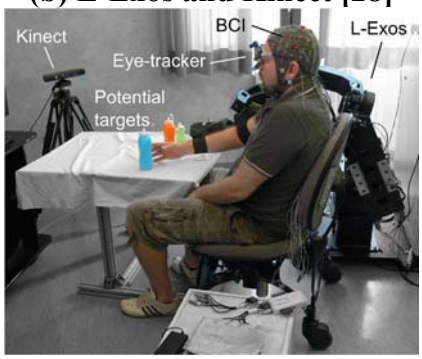

(d) Gaze-BCI-driven exoskeleton [32]

Figure 5. HIR robot controllers

Frisoli *et al*., [32] introduced a complex system to control their exoskeleton, L-Exos, to realize a rehabilitation training in a real environment (see Figure 5(d)). In order to capture the human operator's motion intent, a gaze tracker and a machine vision technology are used to point out a targeting object in the operator's visual field and compute the 3D position of it in the robot's coordinate system. Plus, a Brain-Computer Interface (BCI) is integrated to modulate moving parameters such as, the velocity and the acceleration by the operator's intention projected on EEG signals.

1.3. Problem Statement and Idea Representation

As described in Section 1.1, challenges of the HIR control are mainly due to the uncertain human loop. Detecting systems of the human motion intent introduced in Section 1.2.4 are considered to overcome such challenges. In this context, this dissertation considers an EMG based approach. As described in Section 1.2.4, some intrinsic problems of the EMG signal need to be resolved to realize the motion intent detection from the surface EMG signals. In this context, a mobile motion capture system (MCS) that is enhanced with myoprocessors of selected major arm muscle groups is developed in this dissertation. The myoprocessor quantifies the EMG measurement as muscular force values of selected muscle groups as introduced in Section 2.5. From this standardized way of EMG interpretation, it is expected that the proposed mobile MCS can be utilized as a tool for detecting the human motion intent in point-to-point reaching actions.

Let us assume that the operator's motion intent is successfully captured. Then what is the missing link between the captured motion intent and an actual control command

generated by the HIR controller? For instance, though the motion intent can be captured as a targeting position in the robotic coordinate system, there still remains a question of how the reference motion kinematics or dynamics should be specified to meet the HIR's purpose. In this context, this dissertation proposes that principles of human motor coordination need to be modeled and implemented in the robotic loop. As the robotic loop can understand how the human loop behaves under a certain goal of motion (that is detected as a motion intent), the HIR controller can 1) emulate human motion profiles to determine its action in accordance to the desired resultant motion for assistive purpose, or 2) provide a guidance (i.e., how the human subject's limb is supposed to move to achieve the goal) to the human loop when its motor function is limited by any physical impairments.

Though it seems that modeling behaviors of the human loop is very challenging due to its versatility and complexity, it is still plausible up to a certain degree of predictability. This can be supported by the fact that the kinematics and dynamics of human motions are highly patterned for well-trained cases. This explains that the human CNS is organized in a way that its motor coordination ability is relying on a number of governing rules (either innate or learned), and the detailed motor commands are generated according to them (see Section 3.2 for detailed explanations). This dissertation seeks to identify those governing rules by observing experimental data. By comparing motion data with and without a joint constraint condition, such governing rules will be explained as invariant features of motion kinematics and dynamics.

From the understanding on observed human motor behaviors, the final outcome of a HIR controller are eventually the desired motion command for the HIR. Among almost an infinite number of possible ways of applications, the end-effector trajectory generation of a human-arm-like robotic manipulator is considered in this dissertation. Since the human arm can be assumed as a serial linkage chain, recent theories on mechanical linkage kinematics can be utilized to approximate the natural human motion profile. In this dissertation, a human reaching hand profile approximation scheme is developed based on a recent linkage synthesis to take into account hand contact conditions at the initial and the final hand locations.

1.4. Dissertation Overview

This dissertation addresses efforts to develop a computational model on human arm reaching coordination for a medical HIR controller design. As a tool for capturing human motion intent, a mobile motion capture system (MCS) enhanced with myoprocessors is developed as shown in Section 2. The developed mobile MCS is also utilized as an experimental apparatus to acquire rich experimental data on human arm reaching. In Section 3, experimental observations are presented with and without the elbow joint constraint condition to identify motor coordination principles by identifying common motion features. As an example of the desired HIR motion profile generation based on the finding described in Section 3, an approximation method of natural human hand profiles is developed in Section 4. The approximation scheme is based on a linkage synthesis with higher order motion derivatives to take hand contact conditions into account. In Section

5, a novel prosthetic arm controller is described as a future application of the results of this dissertation. An overview of this dissertation and major contributions are presented in the final section.

2. A MOBILE MOTION CAPTURE SYSTEM ENHANCED WITH MYOPROCESSORS FOR CAPTURING KINEMATICS AND DYNAMICS OF HUMAN ARM REACHING

2.1. A Survey on Motion Capture Systems

Human motions have been studied in various fields of research to identify its optimal and robust performance even against varying external conditions. Especially for those in robotics and mechatronics fields of study, gracefulness, efficiency and optimality of human movements attract enough interests to attempt implementation of such characteristics in control systems (e.g., robotic motion control with artificial cerebellum [35, 36]). As described in the Section 1, understanding the underlying principles of human reaching coordination and its computational model development are beneficial for controlling a HIR system. In order to identify such motor coordination principles (MCP) from experimental observations, a motion capture system (MCS) is required to collect large amount of motion data performed in ADL.

2.1.1. Motion kinematics

Vicon (Vicon Motion Systems Ltd., UK) is the most widely known MCS commercial product (see Figure 6(a)). This optical MCS involves multiple high-resolution cameras with infrared emitters and a computer interface box that can transfer large amount of captured data to a host PC in real-time. Each camera captures infrared light reflected from markers attached on a human body and can calculate spatial positions with respect to pre-defined coordinates by the triangulation principle. The Optotrak Centus (Northern Digital

Inc., Canada) is another optical MCS that utilizes IRED (infra-red light emitting diodes) markers with a stereo-camera (see Figure 6(b)). Those optical MCS can acquire fast motions with the highest accuracy. However, their expensive costs and special settings (e.g., no reflective objects should be around and a proper light condition should be met for clear identification of markers in the capturing volume) limit their practicability. In addition, in cases when the number of cameras is not enough or some of markers are occluded from the sight of cameras by the subject's own body, reconstructing the human motion kinematics is almost impossible due to those missing data points. The MotionStar (Ascension Technology Co., Burlington, VA) is a tethered MCS which uses static magnetic fields (see Figure 6(c)). Each receiver attached on a body segment can compute its position and orientation with respect to a static magnetic field transmitter from sensed magnetic flux variations. The magnetic MCS can capture the motion without occlusions. However, its data can be strongly disturbed by electromagnetic fields around ferromagnetic or electromagnetic objects. The Kinect (Microsoft Co., Redmond, WA) is a machine vision based MCS that contains a RGB camera, a depth sensor and a multi-array microphone. Based on the range camera technology originally developed by an Israel company, PrimeSense Ltd., the Kinect can recognize the gesture and human figure from the captured image data. Despite pros of listed MCS, they all have limited capturing volume (or space) which is undesirable for the ADL motion capture in real-life environments.

(a) Vicon

(b) Optotrak

(c) MotionStar

(d) Kinect

Figure 6. Conventional Motion Capture Systems (MCS)

There are wearable mobile MCS developed to resolve the spatial limitations and the mobility issues. The Shapewrap III (Measurand Inc., Canada) is a mechanical type MCS that utilizes fiber optic based band type shape sensor arrays (see Figure 7(a)). Though it is developed as a lightweight and wearable suit to achieve a wireless MCS, the system has no means to aware its absolute location with respect to any fixed external coordinates. Recently, as the MEMS (microelectro-mechanical system) technology advances, MEMS IMU (inertial measurement unit) based mobile MCS have been developed. Generally, IMU contains of an accelerometer, a rate gyroscope and a magnetometer that all can measure three axes data. From the sensor reading, the orientation of the sensor can be computed relative to directions of the gravity and the local earth magnetic field vectors. On the other hand, the sensor orientation can also be

estimated by integrating the angular rate signal from a known initial orientation. Due to noisy accelerometer readings and the slow response rate of the magnetometer, the former method is reliable for low frequency movements while the later scheme is suitable for high frequency motions due to a drift effect that arises during the gyroscope output integration. Therefore, two estimation results are fused in a complementary manner to get the best estimation. This technology allows us to develop untethered and mobile MCS that are practical enough to use for our original purpose. The IGS-180 (Animazoo Ltd., UK) is a full body motion capture suit that equips military grade IMUs on each body segment (see Figure 7(b)). The MVN Awinda (Xsens, Netherland) is a similar type motion capture suit that allows a complete wireless and source-less motion capture (see Figure 7(c)). For its complete mobility and descent accuracy without an occulusion problem, the IMU based mobile MCS is selected as the ideal solution for our original purpose, the ADL motion capture.

(a) Shapewrap III **(b) IGS-180** **(c) MVN Awinda**

Figure 7. Wearable type MCS

2.1.2. Motion dynamics

Some of the MCS allow extensive measurements on motion dynamics such as joint torque values. In most cases, the joint torque is computed by integrating the captured motion kinematics into the inverse dynamics of the subject's body. Since the inverse dynamics model involves an external contact force term, force plates are typically used to propagate the inverse dynamics computation from the ankle joint to more proximal joints. Jung *et al*., [37] introduced a mobile MCS integrated with smart shoes that can function as a mobile version of a force plate under each foot. Upper limb joint torque values can also be estimated in a similar manner. In case of free arm reaching movements, the external contact force term can be ignored with an assumption of no contact condition.

As mentioned in Section 1.1, the task portions of core motor functions in ADL involve hand manipulations that allows for interactions with the external environment. Tactile force sensing gloves can be a solution to capture the interactive force vector at the hand. However, this method needs to resolve a redundancy in the inverse dynamics problem to convert the interactive hand force into joint torques. In the control of exoskeleton type HIR, interactive joint torque values can provide rich information to extract the human subject's motion intent or to assess the motor performance. Generally, electromyography (EMG) is used as an intrinsic measure of such interactions in joint or muscle levels. The EMG is a projection of neural signal from the CNS, and it can be measured as an electrical pulse signal generated from muscle fibers when they contract. Though the EMG has a known property that its magnitude is proportional to the muscle's isometric contractile force (or its resultant joint torque) as shown in [38], its signal

nonlinearities and irregularities limit its direct applications in HIR systems. For this reason, extracted feature values normally mediate the sensed EMG and the control input of the HIR. Such features allows the system to quantify the neural command from the acquired EMG in a standardized way. Lee *et al*., [39] compute a virtual torque at a joint from EMG signals of the agonist and antagonist muscle pair with a recursive least square algorithm. Kiguchi *et al*., [40] designed a neuro-fuzzy controller to determine control inputs for their upper limb exoskeleton robot from measured EMG signals. Among various features, however, the actual muscular force estimation based on a physiological model seems the most standardized way to quantify the EMG signal. Cavallaro *et al*., [17] proposed such technique called a myoprocessor that can estimate the muscular contractile force from the EMG signal in real-time. The myoprocessor consists of a human arm kinematic model, which converts anatomical joint angles into the muscle kinematics, and a modified Hill-based muscle model (see [41]).

2.2. Idea Representation: Overall System Structure

This dissertation adopts the myoprocessor technique to compute the tension of selected muscle groups to enhance the proposed mobile MCS. The integration of the wireless IMU based mobile MCS and the wireless EMG sensor based myoprocessors allows us to capture rich kinematic and dynamic information of the human arm reaching in real-life environments. Figure 8 shows the overall system structure of the proposed mobile MCS enhanced with myoprocessors. The system mainly consists of wireless IMU and EMG

sensor hardware (Figure 8(a)), IMU based motion capture algorithms (Figure 8(b)) and Myoprocessors (Figure 8(c)).

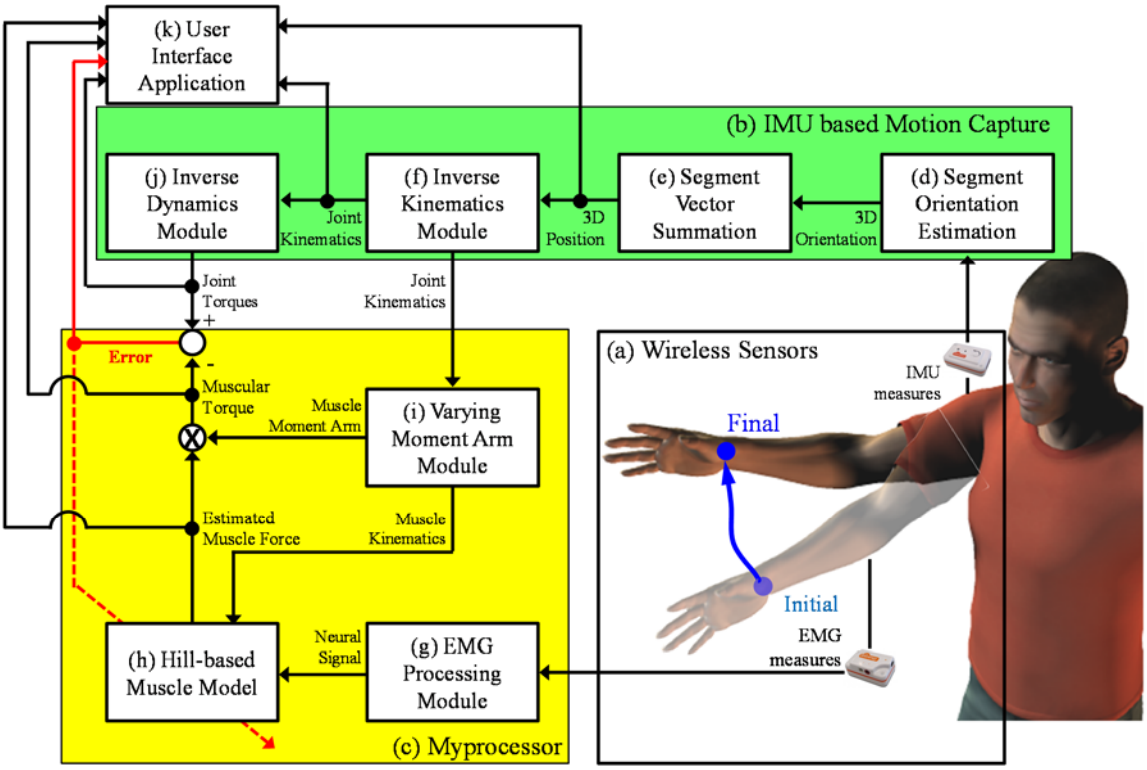

Figure 8. Overall system structure of the proposed mobile MCS enhanced with myoprocessors.

From the sensor output of a wireless IMU attached, the orientation of the corresponding arm segment in space is estimated with respect to the Earth coordinates (Figure 8(d)). Since the human arm kinematics can be approximated by a series of rigid linkages, 3D spatial positions of each joint (i.e., shoulder, elbow and wrist) can be computed as a consecutive vector sum of each segment with the estimated orientation

(Figure 8(e)). From the geometry of the arm configuration, anatomical joint angles are derived by an inverse kinematics module (Figure 8(f)).

Each wireless EMG sensor collects an activation signal of a selected muscle. The raw EMG measurement is processed by filters to condition its signal and to recover the neural signal projected from the CNS (Figure 8(g)). As an empirical model, the Hill-based muscle model (Figure 8(h)) can approximate a muscular force value with two inputs: the neural signal from the EMG measurement and the muscle kinematics (i.e., the change of muscle length, its rate of change and the moment arm). Due to complex anatomical structures inside the human body and redundancies of skeletal muscles acting on a joint, a muscle length cannot be modeled as a linear function of the corresponding joint angles. The varying moment arm module takes such complexities into account and computes a precise muscle kinematics (Figure 8(i)). From a simple multiplication of the moment arm and the estimated muscle force, a muscular joint torque can be computed.

Since the human arm can be considered as a series of rigid links, the required joint torque can be estimated from the captured motion via an inverse dynamics module (Figure 8(j)). As a result, the proposed mobile MCS can obtain two different estimations of the joint torque. The error between the two estimations contributes the major novelty of the proposed system compared to previous MCS. The Hill-based muscle model contains many physiological parameters, and most of them are not measurable (e.g., cross-sectional area of the muscle, tendon slack length and optimal fiber length). Though physiological data can provide nominal values, those parameters need to be tuned for each individual for the best estimation result. For this purpose, a parameter optimization scheme is adopted to

find the best physiological parameter values by fitting the model with a reference, i.e., the inverse dynamics based torque estimation (see dashed red arrow in Figure 8, it represents an offline parameter optimization procedure). Once the Hill-based model is best tuned, ideally the two estimation results will have the same value. This allows us to capture a discrepancy between two estimations that can be possibly a quantified measure of physical interaction with external environments. In other words, the Hill-based muscle model based joint torque estimation measures actual value while the inverse dynamics based estimation only accounts for the wearer's arm dynamics, and therefore the external contact force term amount can be inferred from the deviation between two estimations. This new feature can be utilized to detect the physical interaction and possibly the human operator's motion intent within the HIR systems. In the following subsections, detailed information about the sensor hardware specifications, the IMU based motion capture algorithms and the myoprocessors are presented.

2.3. Sensor Hardware Specifications

Shimmer 9 DOF IMU and EMG sensors are selected to constitute the proposed mobile MCS prototype. Each IMU module can sense three axes angular rate (up to ±500°/s) and three axes magnetic flux (±0.7~4.5 Ga adjustable range) [42]. The EMG module can acquire a single channel signal through bipolar surface electrodes with the device volume of $53 \times 32 \times 23$ (mm^3) [42]. Each module (or daughter board) is assembled with a wireless sensor unit, which has three axes accelerometer (±1.5 g or ±6 g selectable range) in it [42]. Each platform can be connected to a host PC through a built-in Bluetooth radio. Shimmer

sensors can be interfaced with various supporting software such as LabVIEW, MATLAB and Android operating system. Figure 9 shows each IMU and EMG sensor with their dimensions.

(a) 9 DOF IMU sensor **(b) Single channel EMG sensor**

Figure 9. Shimmer wireless sensors [42]

2.4. IMU based Motion Capture Algorithms

2.4.1. Rigid body orientation estimation

2.4.1.1. Background knowledge

Two unparalleled vectors that are fixed in a global coordinate system allow to geometrically measure a 3D orientation of a moving frame with respect to the global frame. In this context, the earth's gravity and magnetic field vector have been used for navigating air/water transportations with a dead reckoning algorithm (see [43, 44] for examples). Within the inertial navigation system (INS), an accelerometer and a magnetometer respectively function as an inclinometer and a compass to read the vehicle's attitude information with respect to the earth frame normally defined as the NED (North East Down). The INS also includes a gyroscope reading for enhancing the orientation

estimation and absolute position aiding sensors such as GPS (global positioning system) to reduce dead reckoning errors.

As the MEMS (micro-electro-mechanical system) technology advances, the size of IMU has been dramatically decreased, and it triggered various efforts to adopt the INS into the human MCS development as presented in Section 2.1. Accuracies of the MEMS IMU, however, are lower compared to mechanical inertial sensors due to significant measurement noise level, which amplifies drift errors in the dead reckoning algorithm. Moreover, the scale of measuring movement is much smaller in the MCS application than the conventional INS navigation, which induces critical degeneracy of the position estimation with the MEMS IMU. Therefore in general, only the rigid body orientation estimation, which is relatively accurate even within the MEMS IMU setup, is utilized to capture the human motion rather than using the full dead reckoning based position tracking algorithm in the MCS application.

In order to get the best orientation estimation, various sensor fusion methods have been proposed. Sabatini [45] used a rate gyroscope integration that is fused with aiding sensors (i.e., an accelerometer and a magnetometer) in an extended Kalman filter (EKF) structure to get the best estimation. In his work, measurement covariance matrix is modulated according to monitored magnitudes of measured acceleration and magnetic flux to discard the sensor input when it is highly contaminated by motion induced accelerations or magnetic disturbances. Yun *et al*., [46] developed another EKF structure that takes a quaternion estimation from accelerometer and magnetometer inputs through the QUEST (QUaternion ESTimator) algorithm (see [47] for details) as an input. In their

work, the quaternion dynamics updated by the gyroscope input is set as the system process model and the estimated quaternion input from the QUEST is used for the corrective phase of the EKF.

Luinge and Veltink [48] adopted an accelerometer to measure inclination angle of the body within a complementary Kalman filter (CKF) structure. They further developed their idea to get a 2 DOF orientation (i.e., pitch and roll) estimation with higher accuracy by integrating a rate gyro input to the CKF setup [49]. Later, in order to read the heading (i.e., yaw) information, Roetenberg *et al*., [50] updated the CKF by adopting a magnetometer reading with a magnetic disturbance compensation scheme. While the EKF linearizes a nonlinear system dynamics with a first order approximation, the CKF can reduce the approximation error by modeling the error dynamics which can be considered more linear than the system dynamics. Recently, Schepers *et al*., [51] developed a mobile inertial MCS that involves a mobile magnetic transmitter and its receivers to aid estimated absolute position and orientation information. It seems that this prototype became commercialized as the Xsens MVN motion capture suit shown in [52].

Though the Kalman filter gets the optimal estimation in the least square sense, it may not be optimal in the real-life situations since measurement and process noise distributions are mostly not Gaussian but varying according to circumstances. In this sense, a complementary filter (CF) is widely used for its robustness and simplicity. The CF takes advantage of complementary frequency characteristics of IMU readings in a model free setup. Young *et al*., [53] fuse the high-pass filtered gyroscope integration with the low-pass filtered vector observations on gravity and earth magnetic field vectors in a CF

structure. Since the cutoff frequency of the complementary filter design is critical to the performance of the orientation estimation, Calusdian *et al*., [54] developed an adaptive-gain CF that can switch the cutoff frequency according to the motion dynamics. Chang-Siu *et al*., [55] proposed a time-varying complementary filter design that can continuously change its cutoff frequency according to the magnitude of the accelerometer input in a fuzzy logic format. One of the most recent advances in the CF for the MCS application can be found in [37]. Its simple architecture for the cutoff frequency adaptation enables the proposed time varying complementary filter (TVCF) to estimate the 3D orientation of a rigid body with descent accuracy in a wide range of motions. For this reason, this dissertation adopts the TVCF introduced in [37] for estimating arm segment orientations with slight modifications.

2.4.1.2. Factored Quaternion Algorithm (FQA) for the static quaternion estimation

The Factored Quaternion Algorithm (FQA) was introduced by Yun *et al*., [56] to measure the orientation of a static or a slow-moving rigid body from the gravity and the local magnetic field vectors. Compared to the optimal solution for the Wahba's problem [57] (i.e., the QUEST algorithm [47]), the FQA is driven by simpler formulas that is more suitable for a real-time setup. Also, by using only the horizontal components of the magnetic field vector, the estimation of yaw is separated from roll and pitch estimations. This protects roll and pitch estimations from magnetic disturbances and the yaw estimation from motion-induced accelerations, respectively. In what follows, detailed derivation of the FQA, which is slightly modified from the original work by Yun *et al*., [56] to fit the specific setting of the proposed MCS, is presented.

From the pre-defined IMU sensor local coordinates shown in Figure 9(a), each Euler angle ϕ (roll or bank), θ (elevation or pitch) and ψ (azimuth or yaw) is defined as a respective rotation about its *x*-axis, *y*-axis and *z*-axis. The orientation of the sensor frame is defined as consecutive rotations in the ZXY (azimuth-roll-elevation) order from the reference state where the sensor frame is perfectly aligned with the earth coordinates, ENU (East North Up). Note that though the sensor frame makes an azimuth rotation, it does not affect the computation of roll and elevation angles. After an azimuth rotation, a consecutive roll rotation ϕ makes the resulting gravity reading as:

$$\begin{aligned} a_y &= -g\sin\phi, \\ a_z &= -g\cos\phi, \end{aligned} \tag{1}$$

where the gravity acceleration is g = 9.81 m/s^2. Note that the *y*-axis component is not changing even after the following elevation rotation θ. Therefore, only the *y*-axis component in equation (1) is utilized for the roll quaternion computation. Also, for a quasi-static movement, the magnitude of the acceleration is close to g. By normalizing the accelerometer signal and applying a trigonometric identity,

$$\begin{aligned} \sin\phi &= -\overline{a}_y, \\ \cos\phi &= \sqrt{1-\sin^2\phi}, \end{aligned} \tag{2}$$

where $\overline{a}_y$ indicates the normalized *y*-axis component of the accelerometer reading. As we assign the positive sign for cosϕ, the range of the roll angle is limited within $-\pi/2 \le \phi \le \pi/2$. From the configuration of the Shimmer IMU sensor attachment, the roll ϕ corresponds to the humeral rotation and the forearm pronation/supination DOF of the upper arm and the forearm segments, respectively. According to a literature survey on shoulder range of motion (ROM) by Anderton *et al*., [58] the published average ROM of the humeral rotation DOF is within the internal rotation of 74˚ and the external rotation of 83˚ which are within the defined roll angle limits. Also, the ROM of the forearm rotation DOF falls into the same range (i.e., average supination 77˚ and pronation 61˚ in [59]). The roll quaternion q_r is derived from (2) as [56]:

$$q_r = \left[\cos\frac{\phi}{2} \quad \sin\frac{\phi}{2} \quad 0 \quad 0 \right], \tag{3}$$

where by the trigonometric half angle formula,

$$\begin{aligned} \sin\frac{\phi}{2} &= \operatorname{sign}(\sin\phi)\sqrt{\frac{1-\cos\phi}{2}}, \\ \cos\frac{\phi}{2} &= \sqrt{\frac{1+\cos\phi}{2}}. \end{aligned} \tag{4}$$

After the roll, the elevation θ results in the following accelerometer reading:

$$\begin{aligned} a_x &= g\cos\phi\sin\theta, \\ a_z &= -g\cos\phi\cos\theta. \end{aligned} \tag{5}$$

Note that the sign of each component can be different from [56] since the ENU earth coordinate is defined in this dissertation instead of the NED. From the normalized accelerometer signal, (5) can be rewritten as:

$$\begin{aligned} \sin\theta &= \frac{\overline{a}_x}{\cos\phi}, \\ \cos\theta &= \frac{-\overline{a}_z}{\cos\phi}. \end{aligned} \tag{6}$$

In the case where the roll $\phi = \pm\pi/2$, the elevation quaternion riches a singularity. Except the singularity case, the elevation quaternion q_e is derived by the same half angle formulas shown in (4):

$$q_e = \begin{bmatrix} \cos\frac{\theta}{2} & 0 & \sin\frac{\theta}{2} & 0 \end{bmatrix}, \tag{7}$$

where the range of elevation angle is limited by $-\pi \le \theta \le \pi$ by convention.

In order to compute the azimuth quaternion q_a, the magnetometer input in the sensor frame, m, is rotated by roll and elevation quaternions, to align its horizontal components on the ENU frame:

$$M = q_r \otimes q_e \otimes m, \tag{8}$$

where M is the rotated magnetometer input vector in the ENU frame, and $\otimes$ refers to the quaternion multiplication. The azimuth ψ is the angle between the rotated vector M and the local earth magnetic field vector n on the ENU's horizontal plane within the range $-\pi \leq \psi \leq \pi$. Therefore, by applying the law of cosine on horizontal components of those two vectors,

$$\begin{aligned} \cos\psi &= \frac{M_x n_x + M_y n_y}{\sqrt{M_x^2 + M_y^2} \cdot \sqrt{n_x^2 + n_y^2}}, \\ \sin\psi &= \sqrt{1-\cos^2\psi} = \frac{M_x n_y - M_y n_x}{\sqrt{M_x^2 + M_y^2} \cdot \sqrt{n_x^2 + n_y^2}}, \end{aligned} \tag{9}$$

where subscripts $_x$ and $_y$ depict the x and y components of a vector, respectively. With the same half angle formulas shown in (4), the azimuth quaternion is derived as:

$$q_a = \left[\cos\frac{\psi}{2} \quad 0 \quad 0 \quad \sin\frac{\psi}{2} \right]. \tag{10}$$

From the obtained quaternions, (3), (7) and (10), the static quaternion estimation q_s of the sensor frame can be represented as following sequential multiplications:

$$q_s = q_a \otimes q_r \otimes q_e. \tag{11}$$

In order to avoid the singularity situation, magnetometer and accelerometer readings are rotated by the offset roll quaternion q_α when the cosϕ becomes smaller than a pre-defined threshold value as shown in [56]. With the rotated sensor readings, the altered quaternion q_{alt} is derived by (11) then it is rotated back to the true estimation q_s given by

$$q_s = q_{alt} \otimes q_\alpha. \tag{12}$$

2.4.1.3. Time varying complementary filter (TVCF) for the data fusion

The FQA is designed for estimating the quasi-static/static quaternion q_s. When a human motion becomes dynamic, the FQA cannot read the true gravity direction since the accelerometer signal contains a motion induced acceleration. For this reason, the dynamic quaternion q_d is estimated from the gyroscope input by a linear approximation of the quaternion dynamics [60],

$$\dot{q}_d = \frac{1}{2} q_d \otimes \omega, \tag{13}$$

where ω is the angular velocity vector in the sensor frame (i.e., gyroscope input vector). Therefore, the dynamic quaternion at the k-th time step can be derived as

$$q_{d,k} = q_{d,k-1} + \frac{T}{2} q_{d,k-1} \otimes \omega_k, \tag{14}$$

where T indicates the sampling time.

Every time step, the static and dynamic quaternions are estimated from the IMU readings. Due to different signal characteristics of IMU inputs, their estimations have different reliabilities for different frequency regions. The dynamic quaternion q_d is more reliable for highly dynamic movements due to a fast response time of the gyroscope while the static quaternion q_s is more accurate for quasi-static movements since it is derived from readings on absolute vectors (i.e., the gravity and the local earth magnetic field vector). As a relative estimation from a known initial value, q_d has an avoidable drift error problem due to the integration process shown in (14). On the other hand, q_s suffers a noise problem since it is computed from raw accelerometer and magnetometer signals. Note that the integration functions as a filter for the gyroscope input. In addition, q_s is limited to track dynamic motions due to a slow response rate of the magnetometer. In order to fuse two estimations and get the best of each, the time varying complementary filter (TVCF) introduced by Jung *et al*., [37] is adopted in this dissertation. In the following paragraph, the derivation of the TVCF design described in [37] is reviewed.

In order to filter a low frequency response of the static quaternion, a second order Butterworth low-pass filter in the frequency domain, introduced in [61], is designed as

$$G(s) = \frac{1}{\left(\frac{s}{\omega_c}\right)^2 + \sqrt{2}\frac{s}{\omega_c} + 1}, \tag{15}$$

where ω_c is the filter cutoff frequency. By the bilinear transformation with the sampling time T, the Butterworth low-pass filter can be transformed into the discrete time domain,

$$G(z)=\frac{\omega_c^2T^2(z+1)^2}{\left(\omega_c^2T^2+2\sqrt{2}\omega_cT+4\right)z^2+2\left(\omega_c^2T^2-4\right)z+\left(\omega_c^2T^2-2\sqrt{2}\omega_cT+4\right)}. \quad (16)$$

The TVCF is constituted by the define low pass filter and its complementary filter given by:

$$\bar{G}(z)=1-G(z), \quad (17)$$

which becomes a second order high pass filter with the same cutoff frequency. As the TVCF needs to modulate its cutoff frequency ω_c according to the captured motion dynamics, the cutoff frequency at the k-th sample, $\omega_c(k)$ is formulated in a smart way:

$$\omega_c(k)=\omega_{low}+\left(\omega_{high}-\omega_{low}\right)S(k), \quad (18)$$

where the sensitivity function $S(k)$ is defined as:

$$S(k)=\exp\left(-s\left(\left|a(k)\right|-g\right)^2\right), \quad (19)$$

where $|a(k)|$ refers to the accelerometer measurement magnitude at the k-th sample, and s is a scalar that determines the bandwidth of $S(k)$ as represented in Figure 10. As a result, the cutoff frequency ω_c becomes closer to the low frequency bound ω_{low} only when the magnitude of the accelerometer measurement is close to the gravity acceleration (i.e., when a motion induced acceleration is close to zero). By this ω_c modulation, the designed TVCF can adjust the weight of the static quaternion in the data fusion process given by

$$Q(z) = \bar{G}(z)Q_d(z) + G(z)Q_s(z), \tag{20}$$

where $Q_d(z)$ and $Q_s(z)$ are z-transformed signal of q_d and q_s, respectively. The detailed structure of the TVCF is shown in Figure 11.

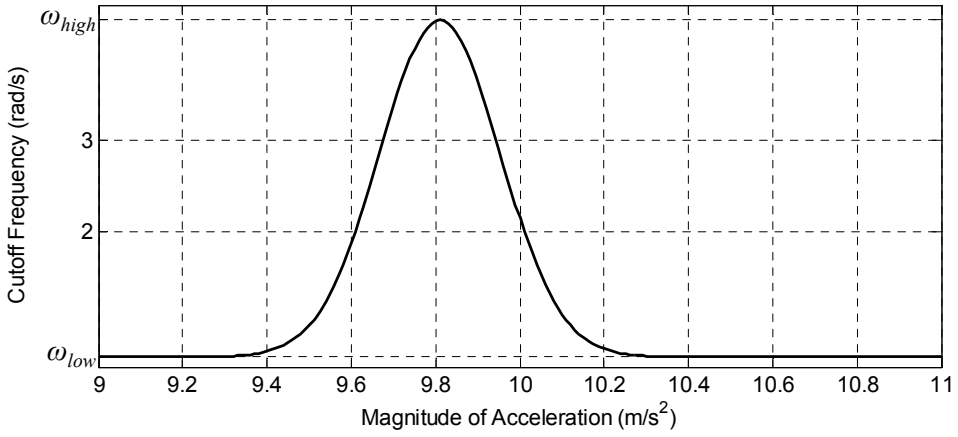

Figure 10. TVCF cutoff frequency modulation with respect to the accelerometer measurement magnitude (regenerated by referring [37])

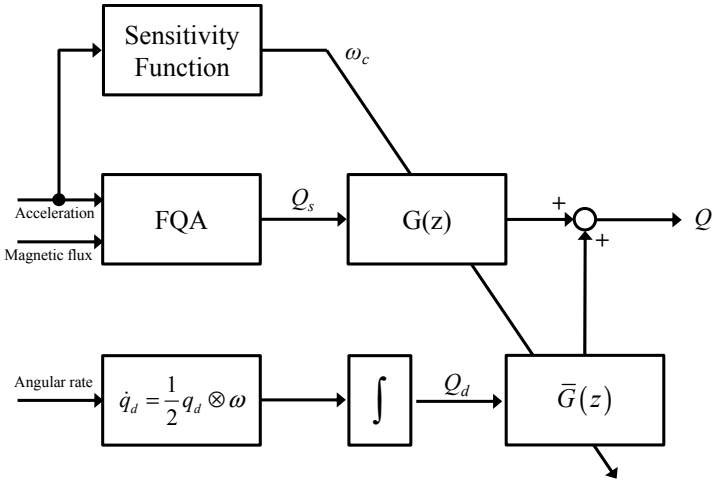

Figure 11. Detailed structure of the TVCF

For the actual implementation of the TVCF, three parameters ω_{low}, ω_{low} and s need to be specified. Since those parameter values are critical to the performance of the TVCF, an arbitrary arm motion experiment is performed to select the optimal parameter values. As the purpose of the proposed MCS is for capturing arm reaching movements, a Shimmer IMU was attached on a human subject's wrist region and captured an arbitrary arm motion. On the Shimmer IMU, three reflective markers were attached as shown in Figure 12(a) to acquire its true orientations via Vicon optical MCS. From the three reflective markers, the sensor frame was defined to be geometrically aligned with the IMU sensor measurement frame shown in Figure 12(b). First, the *y*-axis was defined as a vector connecting two reflective markers attached on the *y*-axis direction of the IMU (see *y* in Figure 12(a)). Next, *x*-axis was approximated as in a similar way to obtain the *x*-*y* plane (see *x*' in Figure 12(a)). The *z*-axis vector was derived by a vector cross product of *x* and *y* axis vectors (see *z* in Figure 12(a)). Then the *x*-axis vector value was finalized by another vector cross product

of y and z-axis vectors. The orientation estimation from the TVCF was compared to the measurement of the Vicon. For a direct comparison, the Vicon position data was transformed into the ENU earth frame by a calibration quaternion q_{cal} given by:

$$q_{cal} = q_{IMU,0} \otimes q_{vicon,0}, \tag{21}$$

where $q_{IMU,0}$ and $q_{vicon,0}$ indicate initial orientation quaternions of the sensor frame in the ENU and the Vicon fixed frames, respectively. It was assumed that the experimental movement was quasi-static at the initial time step to justify this frame alignment.

(a) Marker attachment **(b) IMU sensor frame [42]**

Figure 12. Experimental setup for the TVCF parameter optimization

From the acquired experimental data, the optimal TVCF parameter values were selected to minimize a root mean square cost function J:

$$J = \sqrt{\frac{1}{N}\sum_{k=1}^{N}\left(\mathbf{e}(k)\bullet\mathbf{e}^{\mathrm{T}}(k)\right)}, \tag{22}$$

where N refers the total number of data points and $\mathbf{e}$ is an error vector defined as

$$\mathbf{e}(k) = \Theta_{vicon}(k) - \Theta_{TVCF}(k), \tag{23}$$

where $\Theta_{vicon}(k)$ and $\Theta_{TVCF}(k)$ represent Euler angles of the sensor frame at the k-th time step obtained by the Vicon and the TVCF, respectively. The optimization is achieved by the genetic algorithm built-in function in MATLAB, ga.m, for its better chance to find a global minimum than the nonlinear programming, fmincon.m, that was utilized in [37].

The resulting optimized parameter values are listed in Table 1. The optimized TVCF is applied to another set of experimental data to verify its performance as shown in Figure 13. Estimated orientation from the TVCF is compared with the vicon measurement as Euler angles as shown in Figure 13(a). The deviation of the estimation from the reference is quantified as a mean of the root squared error (MRSE):

$$\mathrm{MRSE}(k) = \frac{1}{3}\sqrt{\mathbf{e}^{\mathrm{T}}(k)\bullet\mathbf{e}(k)}. \tag{24}$$

The TVCF estimation gets larger MRSE value when the motion induced acceleration gets large (see the magnitude of acceleration presented in Figure 13(c)). It can be noticed that

the resulting cut-off frequency ω_c of the TVCF shown in Figure 13(d) is changing according to the magnitude of the acceleration.

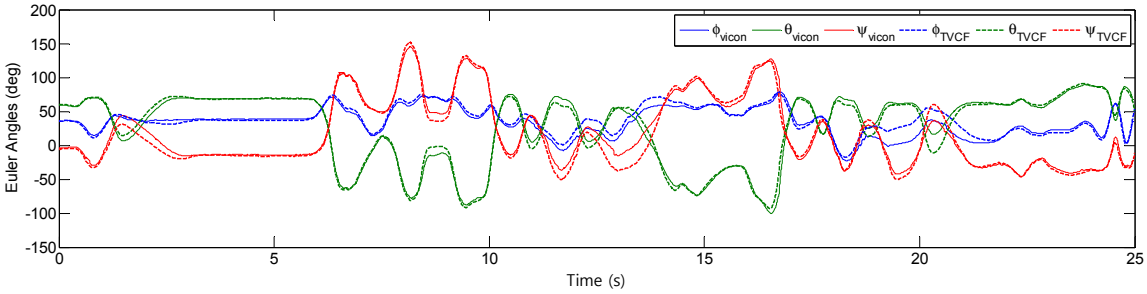

(a) Orientation comparison

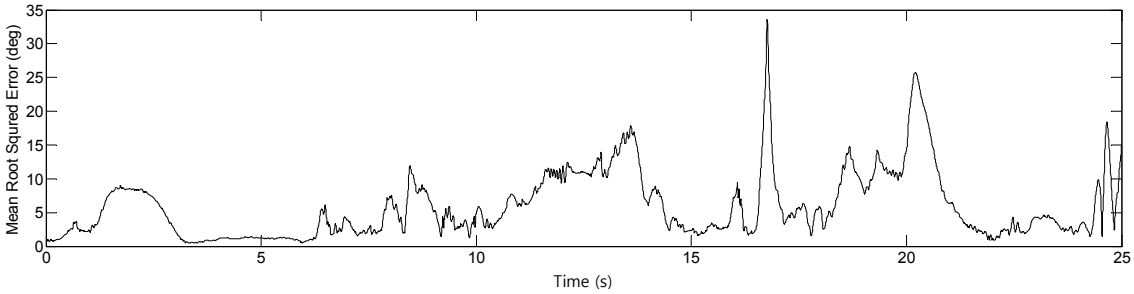

(b) Mean Root Squared Error (MRSE)

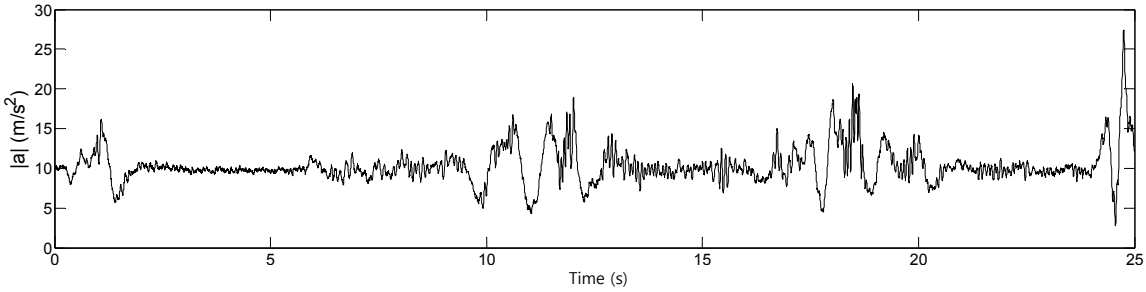

(c) Acceleration magnitude

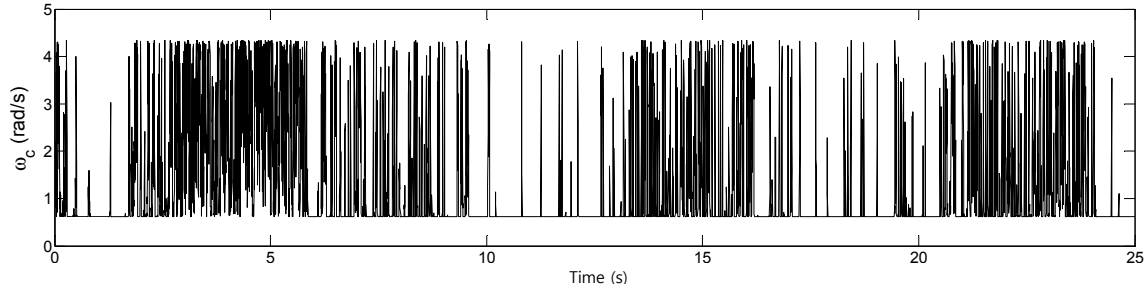

(d) Cut-off frequency ω_c of the TVCF

Figure 13. Experimental verification of the optimized TVCF

Table 1. TVCF parameter values

Parameter	Initial value	Optimized result
ω_{low} (rad/s)	0.5	0.6117
ω_{high} (rad/s)	1	4.336
s	20	24.64

2.4.2. Recovering captured limb kinematics

2.4.2.1. Segment vector summation

The proposed mobile MCS prototype attaches an IMU on a human subject's trunk, upper arm and forearm segments (only the right arm is considered in this dissertation) to capture their orientations with respect to the earth frame, ENU. As the human arm kinematics is approximated by a serial chain of rigid links, the 3D position of each joint center can be recovered from captured segment orientations by consecutive vector summations as introduced in [37].

Each segment vector is defined as a vector connecting two local frames each centered at the segment's proximal and distal joints. In order to closely approximate the human anatomy, the digital cadaver data of the VHP (visible human project) [62] is used to determine the location of each local frame with respect to its proximal segment frame at the rest posture, as presented in Table 2 (see Figure 14(a)). Since the VHP data is specified by a single cadaver, the absolute position of each local frame needs to be individually adjusted. For this purpose, position vectors in Table 2 are normalized by corresponding link lengths in the VHP data and then multiplied by each individual's link length measurements. In case of any difficulties for the link length measurement,

anthropometric rules introduced in [63] can be utilized to determine each link length as a ratio compared to the subject's height H (see Table 3).

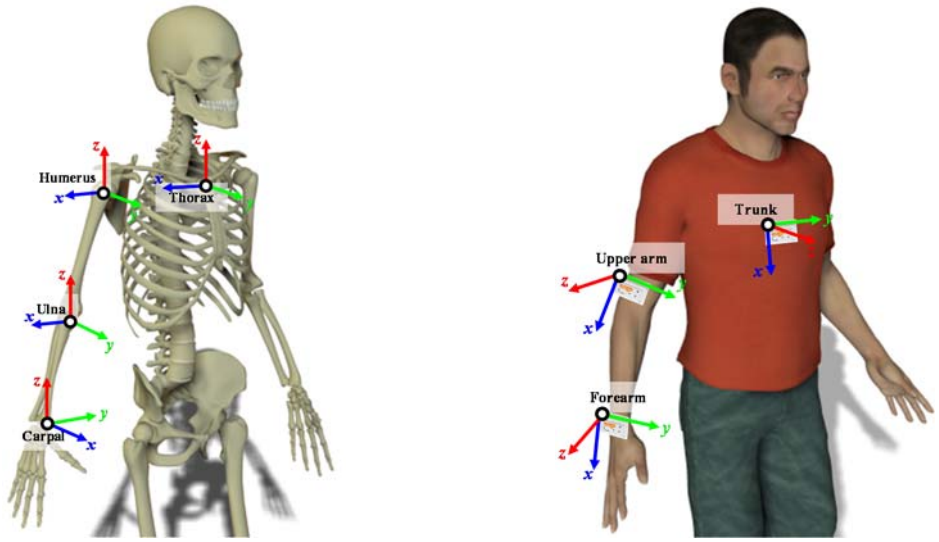

(a) Anatomical frames **(b) IMU (sensor) frames**

Figure 14. Segment frames at the rest posture

Table 2. Each anatomical frame position with respect to its proximal frame [62]

Frame	Anatomical Location	Position of Origin [mm]
Thorax	Sternoclavicular (SC) joint center	in Thorax Frame (0, 0, 0)
Humerus	Glenohumeral (GH) joint center	in Thorax Frame (180.77, -63.80, 27.84)
Ulna	Humeroulnar (HU) joint center	in Humerus Frame (0.81, 25.18, -303.29)
Carpal	Radiocarpal (RC) joint center	in Ulna Frame (5.48, -0,34, -278.11)

Table 3. Anthropometric rules for link lengths [63]

Link	Anatomical Interpretation	Anthropometric Rules
Trunk width	SC joint to GH joint	0.129 H
Upper arm	GH joint to HU joint	0.186 H
Forearm	HU joint to RC joint	0.146 H

Finally, arm motions can be restored as 3D positions of the shoulder, elbow and wrist joint centers in the ENU frame, $\mathbf{P}_j$, by a consecutive vector summation as:

$$\mathbf{P}_j = \sum_{j=1} q_j \otimes \mathbf{p}_j, \tag{25}$$

where j refers the index of a local frame listed in Table 4, q_j is the quaternion representation of the segment orientation in the ENU frame (see (20)), and $\mathbf{p}_j$ is the anatomical segment vector with respect to its proximal frame (i.e., position data shown in Table 2 adjusted for each individual subject).

Table 4. Index of local frames and limb segments

Index	Frame	Limb Segment
$j = 0$	NEU fixed frame	
$j = 1$	Trunk (thorax) frame	Trunk width
$j = 2$	Upper arm (humerus) frame	Upper arm
$j = 3$	Forearm (ulna) frame	Forearm

2.4.2.2. Inverse kinematics of the human arm

The human arm kinematics can be simplified as a seven DOF serial SRS (Spherical-Revolute-Spherical) chain (i.e., one DOF hinge joint at the elbow and three DOF ball and socket joints at the wrist and the shoulder). The captured 3D positions of each joint enable to fully describe the arm configuration in Cartesian coordinates. Taking advantage of it, the same limb movement can be interpreted in joint articulation angles. In this dissertation,

shoulder azimuth α (horizontal motion of the upper arm on the XY plane), shoulder elevation β (vertical rotation of the upper arm), humeral rotation γ (axial rotation of the upper arm) and elbow flexion δ are defined as shown in Figure 15. In order to compute joint angles, an inverse kinematics is defined from the geometry of the arm configuration as introduced in [64]:

$$\begin{bmatrix} \alpha \\ \beta \\ \gamma \\ \delta \end{bmatrix} = \begin{bmatrix} \operatorname{atan2}(x_e, y_e) \\ \operatorname{acos}\left(\dfrac{-z_e}{l_u}\right) \\ \operatorname{atan2}\left(l_u(x_e y_h - x_h y_e), y_e(y_e z_h - y_h z_e) - x_e(z_e x_h - z_h x_e)\right) \\ \operatorname{acos}\left(\dfrac{x_h^2 + y_h^2 + z_h^2 - l_u^2 - l_f^2}{2 l_u l_f}\right) \end{bmatrix}, \tag{26}$$

where $\mathbf{x_e}=[x_e, y_e, z_e]^T$ and $\mathbf{x_h}=[x_h, y_h, z_h]^T$ represent 3D positions of elbow and hand in a fixed frame XYZ centered at the shoulder joint (it is identical to the humerus frame at the rest posture), and l_u and l_f are the respective link lengths of the upper arm and the forearm. For more details, see the IJC (Intrinsic Joint Coordinates) introduced in 3.4.2.

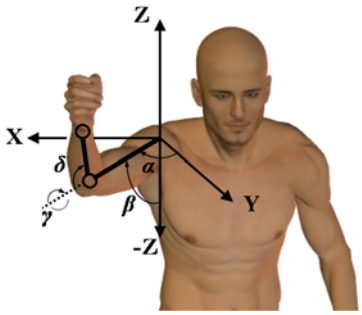

Figure 15. Schematic plot of the joint articulation DOF

Each joint ROM is constrained by complex anatomical structures in our body. From the geometry of arm configuration, each joint ROM is determined for covering an arbitrary reaching movement within the reachable workspace such as:

$$\begin{gathered} -0.25\pi \le \alpha \le \pi, \\ 0 \le \beta \le \pi, \\ \gamma_{\text{ext}}(\alpha,\beta) \le \gamma \le \gamma_{\text{int}}(\alpha,\beta), \\ 0 \le \delta \le \pi, \end{gathered} \tag{27}$$

where the humeral rotation ROM is bounded by two functions, $\gamma_{\text{ext}}(\alpha, \beta)$ and $\gamma_{\text{int}}(\alpha, \beta)$. From their experimental study, Wang *et al*., [65] found out that the humeral rotation ROM is varying according to the elbow position. They derived surface fitting models of the humeral external/internal rotation bounds as functions of latitude and longitude of the elbow position. By representing elbow latitude and longitude in equivalent shoulder azimuth and elevation angles, two bound functions can be obtained as third and fourth order polynomials, respectively:

$$\begin{aligned} \gamma_{\text{int}}(\alpha,\beta) &= \sum_{i=0}^{3} a_i P_i(x,y), \\ \gamma_{\text{ext}}(\alpha,\beta) &= \sum_{i=0}^{4} a_i P_i(x,y), \end{aligned} \tag{28}$$

where polynomial $P_j(x, y)$ is given by:

$$P_i(x,y)=\sum_{m=0}^{i} b_{im}x^{i-m}(\alpha,\beta)\,y^{m}(\alpha,\beta), \tag{29}$$

which utilizes transformations of elbow latitude and longitude as:

$$\begin{aligned} x(\alpha,\beta)&=\left(\frac{\pi}{2}-\alpha\right)\cos\left(\beta-\frac{\pi}{2}\right),\\ y(\alpha,\beta)&=\beta-\frac{\pi}{2}. \end{aligned} \tag{30}$$

Note that the transformed longitude $x(\alpha, \beta)$ becomes insensitive to the transformed latitude $y(\alpha, \beta)$ when it is pointing poles (i.e., $\beta = 0$ or $\beta = \pi$) [65]. In (29), $b_{i0} = 1$ for each i, and $P_0(x, y) = 1$. Note that the resulting γ angle bounds are in degrees while input angles are in radians. Table 5 and Table 6 list polynomial coefficients that constitute (28) and (29). Figure 16 shows the resultant surfaces of $\gamma_{int}(\alpha, \beta)$ and $\gamma_{ext}(\alpha, \beta)$ within feasible ranges of α and β. Note that all joint ROM defined in (27) cover required mean joint ROM for the ADL collected by Magermans *et al*., [66].

Table 5. Polynomial coefficients of $\gamma_{int}(\alpha, \beta)$ [65]

i	a_i	b_{im}		
	m	1	2	3
0	-139.270			
1	18.652	-2.235		
2	4.092	7.251	-0.654	
3	-2.081	0.069	-10.035	-1.642

Table 6. Polynomial coefficients of $\gamma_{ext}(\alpha, \beta)$ [65]

i	a_i	b_{im}			
	m	1	2	3	4
0	-2.459				
1	9.299	-1.690			
2	3.428	8.615	-2.149		
3	-2.987	0.859	-8,025	0.514	
4	0.331	-13.771	-17.172	35.460	2.189

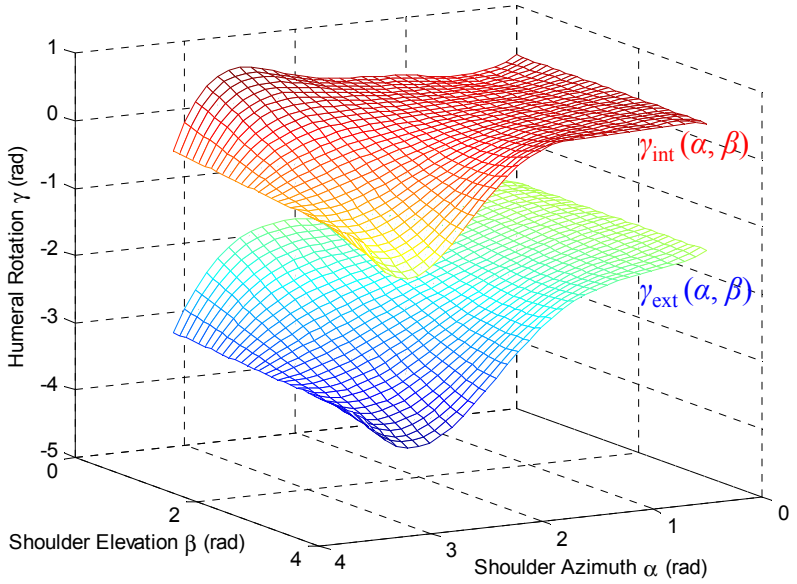

Figure 16. Humeral rotation ROM fitting surface drawn from data shown in [65]

2.4.2.3. Inverse dynamics module

The human arm dynamics can be approximated via serial rigid links model. In this dissertation, following conditions are assumed: 1) each link of the arm is rigid and has a cylindrical shape, and 2) the mass of each link is evenly distributed. Since the wrist DOF are not considered, the human arm is modeled as a serial chain consisting of two rigid links, upper arm and forearm with a hand. In order to determine the physical parameter

values, anthropometric rules shown in Table 7 are adopted [63]. The data enables unmeasurable parameters to be expressed as ratios of measurable ones (e.g., weight and height).

The inverse dynamics module (see Figure 8(j)) is constituted by the joint torque $\tau_{ID,i}$ for each *i*-th joint derived from the Lagrangian mechanics:

$$\tau_{ID,i} = \frac{d}{dt}\left(\frac{\partial(T-V)}{\partial \dot{q}_i}\right) - \frac{\partial(T-V)}{\partial q_i}, \tag{31}$$

where q_i is the generalized coordinates, which is identical to the anatomical joint DOF defined in Figure 15. The term V is the sum of potential energy for each *i*-th link:

$$V_i = m_i g x_{z,i}, \tag{32}$$

where m_i is the link mass and $x_{z,i}$ refers to the vertical position component of the link's center of mass (COM). Finally, T indicates the sum of all kinetic energy term for each *i*-th link,

$$T_i = \frac{1}{2} m_i \mathbf{v}_\mathbf{i}^\mathrm{T} \mathbf{v}_\mathbf{i} + \frac{1}{2} \boldsymbol{\omega}_\mathbf{i}^\mathrm{T} I_i^0 \boldsymbol{\omega}_\mathbf{i}, \tag{33}$$

where $\mathbf{v_i^T}$ and $\boldsymbol{\omega_i^T}$ are the translational and angular velocity vectors of the link's COM, respectively. Here, the moment of inertia I_i^0 with respect to the global frame can be converted from the local frame value, I_i^l, as:

$$I_i^0 = \left(R_i^0\right)^T I_i^l \left(R_i^0\right), \tag{34}$$

where R_i^0 is the rotation matrix from the global frame to the local frame of the i-th link.

Table 7. Anthropometric rules for the inverse dynamics module [63]

Parameters	Definition	Value
m_u	Mass of the upper arm	0.028M[5)]
m_f	Mass of the forearm with hand	0.022M
l_u	Length of the upper arm	0.186H[6)]
l_f	Length of the forearm with hand	0.254H
r_u	Radius[1)] of the upper arm	Measurement
r_f	Radius of the forearm with hand	Measurement
λ_u	Relative position[2)] of the COM[3)] in the upper arm	0.436
λ_f	Relative position of the COM in the forearm with hand	0.682
μ_u	Radius of gyration of the upper arm at the COM[4)]	0.322
μ_f	Radius of gyration of the forearm with hand at the COM	0.486

[1)] Mean value of the measured radius on proximal, medial and distal regions
[2)] (Length from proximal joint to the COM) / (Length of the entire link)
[3)] Center of mass
[4)] (Radius of gyration at the COM) / (Length of the entire link)
[5)] M = total body weight
[6)] H = Height of the human subject

2.4.3. Calibration for IMU frame alignments with anatomical frame vectors

Note that each IMU attached on a limb segment captures the limb orientation in the ENU frame. Therefore, a calibration protocol is required to map physiological motions

represented in anatomical frames defined in Table 2 from 3D orientations estimated in IMU frames. Ricci *et al*., [67] introduced a simple calibration method that utilizes a least square optimization to identify the rotation matrix between sensor frames and human limb functional frames. This dissertation adopts a part of their calibration method with a slight modification to output alignment quaternions.

A series of single axis movements are designed for the calibration procedure. At first, trunk flexion/extension, lateral flexion and axial rotation motions that are respectively corresponding to rotation about *x*-, *y*- and *z*- axis of the thorax frame are asked to be performed by each subject. For the upper arm segment, shoulder flexion/extension, abduction/adduction and humeral rotation movements are performed to acquire *x*, *y* and *z* single axis rotation data of the humerus frame. For the forearm segment, elbow flexion/extension and forearm supination/pronation that correspond to *x* and *z* axis of the ulna frame, respectively. Since there is no anatomically feasible motion for the *y* axis rotation of the forearm, the same data of the shoulder abduction/adduction is used to identify the ulna *y* axis.

In order to identify the main axis of the IMU frame that is corresponding to the single axis calibration movement of the anatomical frame, singular value decomposition (SVD) is applied to the normalized gyroscope readings:

$$\boldsymbol{\Omega}_{IMU} = \mathbf{U}\boldsymbol{\Sigma}\mathbf{V}^{T}, \tag{35}$$

where $\boldsymbol{\Omega}_{IMU} \in \mathbb{R}^{N\times 3}$ is the gyroscope reading vector, $\mathbf{U} \in \mathbb{R}^{N\times N}$ and $\mathbf{V} \in \mathbb{R}^{3\times 3}$ are orthogonal matrix outcomes of the SVD, and $\boldsymbol{\Sigma} \in \mathbb{R}^{N\times 3}$ is a diagonal matrix with singular values σ_i, i = 1,2,3. For each calibration movement, the main axis of the anatomical frame is determined as the right singular vector within **V** corresponding to the highest singular value (i.e., σ_1). By this SVD, a robust discrimination between the useful information (i.e., sensor outputs from actual anatomical motion) and disturbances (e.g., sensor noise and misalignment of the IMU frame and the anatomical frame) is achieved [67]. In addition, computed singular values are used to quantify the reliability of the identified reference axis as a ratio compared to the sum of all singular values [67]:

$$\rho = \frac{\sigma_1}{\sum_{i=1}^{3} \sigma_i}. \tag{36}$$

In the following subsection, identified reference axes and reliability indices are utilized to constitute estimated IMU frame axis vectors and weighting value matrix of the least square optimization, respectively.

For each limb segment, an alignment quaternion is defined to map the anatomical frame shown in Table 2 (see also Figure 14(a)) to its corresponding IMU frame (see Figure 14(b)). As the identified main axis of each calibration movement represents the anatomical frame axis vector with respect to the IMU frame, the mapping between two frames of the i-the limb segment is derived by the alignment quaternion q_i^{align}:

$$\mathbf{v}_i^{IMU} = q_i^{align} \otimes \mathbf{v}_i^{limb}, \tag{37}$$

where $\mathbf{v}_i^{IMU} = \left[\mathbf{x}_i^{IMU}, \mathbf{y}_i^{IMU}, \mathbf{z}_i^{IMU} \right]^{\mathrm{T}} \in \mathbb{R}^{9\times 1}$ and $\mathbf{v}_i^{limb} = \left[\mathbf{x}_i^{limb}, \mathbf{y}_i^{limb}, \mathbf{z}_i^{limb} \right]^{\mathrm{T}} \in \mathbb{R}^{9\times 1}$ are concatenations of axis vectors of IMU and anatomical frames, respectively. Ideally, $\mathbf{v}_i^{limb}$ contains the orthonormal axis vectors: i.e., $\mathbf{x}_i^{limb} = [1, 0, 0]^{\mathrm{T}}$, $\mathbf{y}_i^{limb} = [0, 1, 0]^{\mathrm{T}}$ and $\mathbf{z}_i^{limb} = [0, 0, 1]^{\mathrm{T}}$. We are looking for the best estimation of the q_i^{align} that maps $\mathbf{v}_i^{limb}$ to its corresponding axis vectors in the IMU frame $\mathbf{v}_i^{IMU}$ that is a concatenation of the main axis identified from calibration movements.

The Levenberg-Marquardt least square algorithm is utilized to find the optimal alignment quaternion that minimizes a cost function:

$$C = \boldsymbol{\varepsilon}^{\mathrm{T}} \mathbf{W} \boldsymbol{\varepsilon}, \tag{38}$$

where the error function $\boldsymbol{\varepsilon}$ is defined as:

$$\boldsymbol{\varepsilon} = \mathbf{v}_i^{IMU} - q_i^{align} \otimes \mathbf{v}_i^{limb}, \tag{39}$$

and the weighting value matrix $\mathbf{W}$ is a diagonal matrix constituted by the reliability indices from (36) [67]:

$$\mathbf{W} = \begin{bmatrix} \rho_x \mathbf{I}_{3\times3} & & \\ & \rho_y \mathbf{I}_{3\times3} & \\ & & \rho_z \mathbf{I}_{3\times3} \end{bmatrix} \in \mathbb{R}^{9\times9}, \tag{40}$$

where $\mathbf{I}_{3\times3}$ indicates a 3 × 3 identity matrix. To achieve the optimization, a MATLAB built-in function, lsqnonlin.m, is used.

2.5. Myoprocessor

The myoprocessor is proposed by Cavallaro *et al*., [17] for controlling their upper limb exoskeleton with a neural signal, which is quantified as muscular force value, based on the Hill-based muscle model first introduced by Hill [68]. It is designed to quantify the voluntary actions, captured from the surface electromyography (EMG), as a standardized muscular force. This enables more reliable detection of the subject's motion intent compared to a processed EMG signal, which is highly nonlinear and irregular for different conditions. In order to capture the voluntary motion dynamics within the proposed mobile MCS, this dissertation adopts the myoprocessor design shown in [17] with some modifications to suit the MCS prototype (see Figure 8(c)).

2.5.1. EMG processing module

The Hill based muscle model refined by Winter [41] is one of the most widely known and used solution for approximating the muscular force from two inputs: 1) neural activation pattern (NAP) and 2) muscle kinematics (or joint kinematics). Since the measured EMG signal is a projection of the neural command within the CNS to coordinate an arm motion, the NAP can be extracted from the EMG as a normalized signal $a(t) \in [0, 1]$, where two

boundary values, $a = 0$ and $a = 1$ refer to no activation and maximum voluntary activation, respectively [17]. In order to extract $a(t)$ from an envelope of the EMG signal, a cascade of digital filters are applied to condition the raw EMG signal: 1) high-pass filter (4^{th} order Butterworth filter), 2) full wave rectification and 3) low-pass filter. In their multi-scale physiological muscle model, Hayashibe and Guiraud [69] claimed that the choice of cut-off frequency of the low-pass filter is critical since the envelop of the Hill-based model's estimated force is almost determined by it. Note that the cut-off frequency of the low-pass filter determines a tradeoff between a reliability of the NAP amplitude and an ability of capturing fast contractions [69]. Therefore, the cut-off frequency of the low-pass filter needs to be selected depending on the motion dynamics. According to the SENIAM (Surface EMG for Non-Invasive Assessment of Muscles) project, the European recommendation for slow and fast motions are 2 Hz and 6 Hz, respectively [70].

In order to determine the optimal value according to the motion dynamics, an adaptive low-pass filter (ALPF) is designed in the same manner of the TVCF (see Section 2.4.1.3). The 4^{th} order Butterworth low-pass filter can be derived in the frequency domain [61],

$$G_{ALPF}(s) = \frac{1}{\left(\frac{s^2}{\omega_c^2} - \frac{2s}{\omega_c}\cos\frac{5}{8}\pi + 1\right)\left(\frac{s^2}{\omega_c^2} - \frac{2s}{\omega_c}\cos\frac{7}{8}\pi + 1\right)}. \quad (41)$$

By using the bilinear transformation and approximating coefficients in (41), the ALPF can be obtained in the discrete time domain as

$$G_{ALPF}(z) = \frac{1}{\left(\frac{4(z-1)^2}{\omega_c^2 T^2 (z+1)^2} + \frac{1.531(z-1)}{\omega_c T (z+1)} + 1\right)\left(\frac{4(z-1)^2}{\omega_c^2 T^2 (z+1)^2} + \frac{3.696(z-1)}{\omega_c T (z+1)} + 1\right)} \quad (42)$$
$$= \frac{\omega_c^4 T^4 (z+1)^4}{C_1 z^4 + C_2 z^3 + C_3 z^2 + C_4 z + C_5},$$

where coefficients of the denominator are given by

$$\begin{aligned} C_1 &= 3.696\omega_c^3 T^3 + 9.659\omega_c^2 T^2 + 20.91\omega_c T + 16, \\ C_2 &= 8.392\omega_c^3 T^3 + 1.531\omega_c^2 T^2 - 37.82\omega_c T - 64, \\ C_3 &= 3\omega_c^3 T^3 - 17.79\omega_c^2 T^2 - 4\omega_c T + 96, \\ C_4 &= -4.392\omega_c^3 T^3 - 1.531\omega_c^2 T^2 + 37.82\omega_c T - 64, \\ C_5 &= -2.696\omega_c^3 T^3 + 8.050\omega_c^2 T^2 - 16.91\omega_c T + 16,. \end{aligned} \quad (43)$$

The cut-off frequency ω_c is adapted according to the motion dynamics, which can be quantified by the magnitude of the accelerometer input. Note that the relation between the cut-off frequency ω_c and the acceleration magnitude needs to be an up and down mirror image of Figure 10. For this purpose, the cut-off frequency modulation equation *equation reference goes here* is modified in the ALPF as:

$$\omega_c(k) = \omega_{high} + (\omega_{low} - \omega_{high}) S(k), \quad (44)$$

where ω_{low} and ω_{high} are assigned as 2 Hz and 6 Hz, respectively.

After the cascade of filters, the EMG signal is normalized with respect to the maximum isometric contraction EMG amplitude [17]. This normalized EMG can be assumed as a reasonable approximation of the NAP $u(t)$. As described by Buchanan *et al*., [71], however, a generated muscular force is saturated even though the frequency of motor unit still increases. This induces a nonlinearity that is not characterized by the normalized EMG and a mismatch of Hill-based muscle model estimation especially at low activation level [69]. In order to resolve this problem, Lloyd and Besier [72] proposed a nonlinear scaling formula as

$$a(t) = \frac{e^{Au(t)} - 1}{e^{A} - 1}, \tag{45}$$

where $u(t)$ is the normalized EMG signal (i.e., unscaled NAP) and the nonlinear shape factor A is constrained to $-3 < A < 0$, with $A = 0$ being a linear relationship between $u(t)$ and $a(t)$.

For the proposed mobile MCS prototype, four muscle groups that are responsible for the anatomical joint DOF motions are selected to measure their surface EMG: 1) biceps brachii (elbow flexion), 2) triceps (elbow extension), 3) anterior deltoid (shoulder elevation and azimuth) and 4) posterior deltoid (shoulder elevation and azimuth). Since the resulting force of each selected muscle group is mainly coordinating its distal limb segment with respect to its proximal limb segment, the acceleration magnitude for the each ALPF is derived as:

$$acc_j(t) = \left\|\mathbf{a}_j(t)\right\| - \left\|\mathbf{a}_{j-1}(t)\right\| + g, \tag{46}$$

where $\mathbf{a}_j(t)$ is the accelerometer measurement vector of the j-th limb segment IMU (see Table 4) and $\mathbf{a}_{j\text{-}1}(t)$ is the one for its proximal limb segment IMU. For example, for the biceps brachii muscle, $\mathbf{a}_j(t)$ and $\mathbf{a}_{j\text{-}1}(t)$ are readings from the forearm IMU and the upper arm IMU, respectively. The cut-off frequency ω_c of the ALPF is reasonably determined by only taking the biceps brachii muscle's resulting motion (i.e., elbow flexion) dynamics into account. In order to attach surface EMG electrodes at the most effective sites, an anatomical guide written by Perotto [73] is referenced. Figure 17 shows the detailed structure of the EMG processing module.

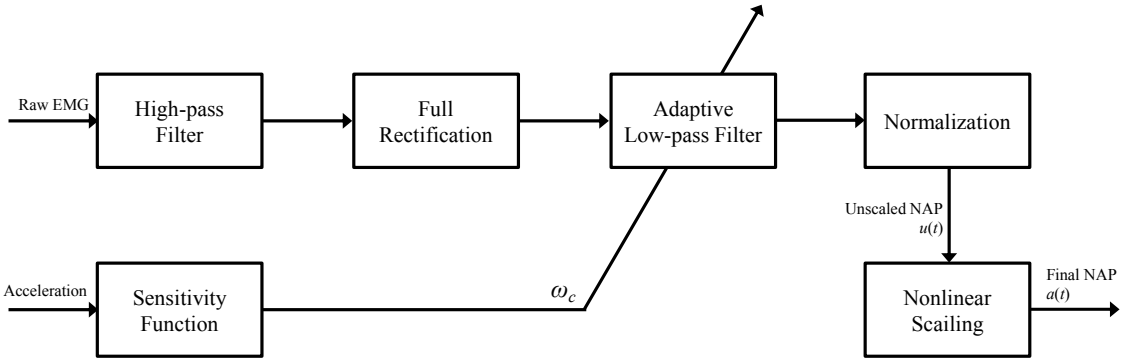

Figure 17. Detailed structure of the EMG processing module shown in Figure 8(g)

2.5.2. Varying moment arm module

The varying moment arm module (see Figure 8(i)) computes the muscle kinematics (i.e., muscle length and its rate of change) and the moment arm for each joint DOF spanned by

the muscle. It is obvious that those outputs are directly related to the captured joint DOF configurations. Some empirical models were proposed to represent the moment arm (or the muscle length) as a function of joint angles by using the polynomial fitting technique [74-76]. However, such models are limited to some selected muscle's average behavior in a single joint articulation. Blemker and Delp [77] developed a three dimensional finite element muscle model from magnetic resonance images to represent muscle geometries as accurate as possible. Since the proposed mobile MCS ultimately aims to be running in a real-time with a limited computational power of mobile devices (e.g., laptops, tablets and smart phones), the finite element model is not adequate due to its expensive computational cost.

Garner and Pandy [62, 78] developed an upper limb musculoskeletal model based on the digital cadaver data of the National Library of Medicine's visible human project (VHP). As locations of anatomical features (e.g., joint center and muscle origin/insertion points) are specified with respect to a common coordinate system within the developed musculoskeletal model, they introduced a mathematical model, called the obstacle set method (OSM) [79], to compute complex muscle path geometries. In the OSM, each muscle is assumed as an elastic band wrapping around anatomical structures (e.g., bones and other muscles) that are approximated as obstacles with equivalent geometries such as cylinders, spheres and sphere capped cylinders. Therefore, the muscle path geometry is derived as the minimum path between its origin and insertion positions through obstacle via points. The OSM is adopted in this dissertation for following reasons: 1) it can be applied to a muscle that is spanned over multiple joint DOF, 2) accurate approximation

compared to simpler models (e.g., straight line model [80]), and 3) affordable computational cost for the real-time application.

Eleven muscle bundles are selected to represent their path geometries with the OSM as shown in Table 8. In the table, spanned joint DOF of each muscle are represented as the anatomical joint DOF derived in Section 2.4.2.2 with its effective direction. All muscles are selected due to their major function in joint DOF articulations. The detailed obstacle types and their coordinates are shown in [78]. Based on the musculoskeletal model, each muscle path is computed as the minimum length path connecting the origin and the insertion points through obstacle via points by using algorithms described in [79]. From the geometry of joint DOF articulations, the moment arm of the *i*-th muscle on the *j*-th joint, b_{ij}, is defined as:

$$b_{ij} = \left(\mathbf{r}_{ij} \times \mathbf{F}_i\right) \bullet \hat{k}_j, \tag{47}$$

where $\mathbf{r}_{ij}$ is the distance vector from the *j*-th joint's rotation axis to the *i*-th muscle's insertion point. $\mathbf{F}_i$ indicates the unit vector of the muscular force direction (i.e., a unit vector pointing the closest obstacle via point from the insertion point) and $\hat{k}_j$ is the rotation axis vector of the *j*-th joint. Figure 18 represents the muscle length and the moment arm of the biceps brachii longhead (BIC$_l$) muscle computed based on the OSM for ranges of the elbow flexion δ and the shoulder elevation β where both the shoulder azimuth α and the humeral rotation γ are fixed at zero.

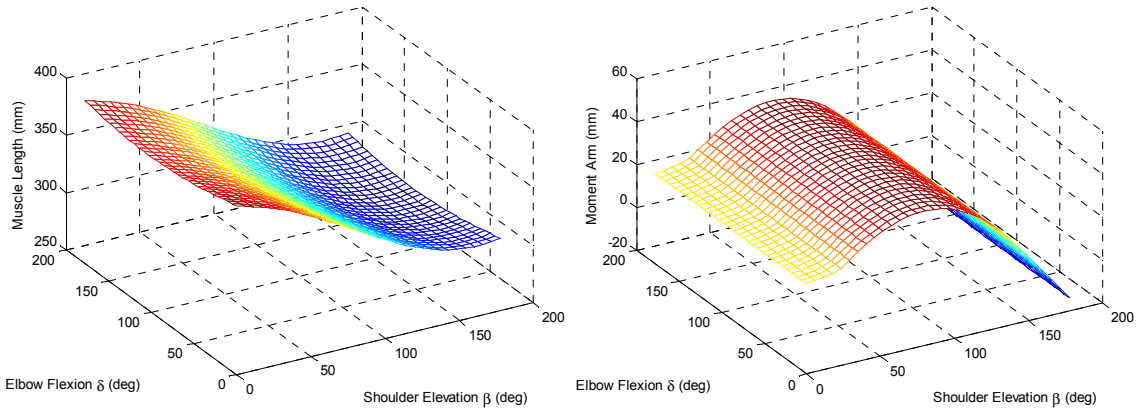

(a) Muscle length **(b) Moment arm**

Figure 18. An example result of the OSM for the BIC_l muscle

Table 8. Selected muscles within the varying moment arm module

Muscle	Spanned joint DOF	Wrapping obstacles
Pectoralis major clavicular (PMJ_c)	Shoulder azimuth (- α) Humeral rotation (+γ)	Single cylinder
Latissimus dorsi thoracic (LTD_t)	Shoulder azimuth (+ α) Humeral rotation (- γ)	Double cylinder
Deltoid clavicular (DLT_c)	Shoulder azimuth (- α) Shoulder elevation (+ β)	Sphere capped cylinder
Deltoid acromial (DLT_a)	Shoulder elevation (+ β)	Sphere capped cylinder
Deltoid scapular (DLT_s)	Shoulder azimuth (+ α) Shoulder elevation (+ β)	Sphere capped cylinder
Biceps brachii short (BIC_s)	Elbow flexion (+ δ)	Double cylinder
Biceps brachii long (BIC_l)	Elbow flexion (+ δ)	Sphere + Cylinder
Brachialis (BRA)	Elbow flexion (+ δ)	Single cylinder
Triceps brachii long (TRC_{lg})	Elbow extension (- δ) Shoulder azimuth (+ α)	Double cylinder
Triceps brachii medial (TRC_m)	Elbow extension (- δ)	Double cylinder
Triceps brachii lateral (TRC_{lt})	Elbow extension (- δ)	Single cylinder

2.5.3. Hill-based muscle model

The Hill-based muscle model is an empirical model of the skeletal muscle's physiological phenomena based on a mechanical model. In what follows, the Hill-based muscle model used in [17] is described with some modifications and detailed derivations. A muscle bundle can be mechanically modeled as paired springs with different properties. Figure 19 depicts a simplified mechanical model consisting of a passive parallel element (PE), a passive serial element (SE) and an active contractile element (CE). From the given mechanical structure, relationships among each element are given as

$$L_{PE} = L_{CE} + L_{SE}, \tag{48}$$

$$F_{SE} = F_{CE}, \tag{49}$$

$$F_{tot} = F_{CE} + F_{PE} = F_{SE} + F_{PE}, \tag{50}$$

where F and L indicate the force and the length of an element, respectively. The parallel and serial elements PE and SE generate passive forces according to their strain.

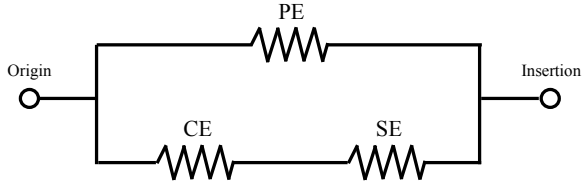

Figure 19. Simplified mechanical model of a muscle bundle

In the Hill-based muscle model, PE and SE share the same equation to compute their passive forces [17]

$$F_{PE,SE} = \left[\frac{F_{\max}}{e^{S}-1}\right]\left[e^{\frac{S\Delta L}{\Delta L_{\max}}}-1\right], \tag{51}$$

where $F_{\max}$ is the maximum force by the element when it reaches the maximum length change $\Delta L_{\max}$, S is a shape parameter related to the stiffness of the element, and ΔL is the length change with respect to the element's slack length that is computed from the OSM. The CE contracts and generates an active force that can be modeled by a product of the force-length envelop f_l and the force-velocity envelop f_l with the neural activation input a by the following equations presented in [17]

$$F_{CE} = a \cdot f_l \cdot f_v \cdot F_{CE_{\max}}, \tag{52}$$

$$f_l = \exp\left[-0.5\left(\frac{\frac{\Delta L_{CE}}{L_{CE_o}} - \phi_m}{\phi_v}\right)^2\right], \tag{53}$$

$$f_v = \frac{0.1433}{0.1074 + \exp\left[-1.3\sinh\left(2.8\frac{V_{CE}}{V_{CE_o}} + 1.64\right)\right]}, \tag{54}$$

$$V_{CE_o} = 0.5(a+1)V_{CE_{\max}}, \tag{55}$$

where $F_{CE_{\max}}$ is the maximal contracture force of the CE, ΔL_{CE} indicates the strain of the CE and L_{CE_o} is the optimal fiber length. ϕ_m and ϕ_v are parameters to form the Gaussian function f_l. V_{CE} refers the velocity of the CE and V_{CE_o} is the maximal velocity when F_{CE} = 0 that is expressed in (55) where $V_{CE_{\max}}$ becomes identical to V_{CE_o} when the NAP becomes maximum (i.e., a = 1). From [17], the following equations are described to explain some more parameters

$$V_{CE_{max}} = 2L_{CE_o}\left(1+4\eta\right), \tag{56}$$

$$F_{PE_{\max}} = 0.05 \cdot F_{CE_{\max}}, \tag{57}$$

$$\Delta L_{PE_{\max}} = L_{\max} - \left(L_{CE_o} + L_{T_s}\right), \tag{58}$$

$$F_{SE_{\max}} = 1.3 \cdot F_{CE_{\max}}, \tag{59}$$

$$\Delta L_{SE_{\max}} = 0.03 \cdot L_{T_s}, \tag{60}$$

where η and L_{T_s} indicate the percentage of fast fibers in the muscle and the tendon slack length, respectively. In (58), L_{max} is the maximum length of the muscle that can be defined as a scalar multiplication of the muscle slack length L_{PE_0}:

$$L_{max} = \left(1+\Delta L_{\max}\right) L_{PE_0}, \tag{61}$$

where the maximal extension strain of the muscle ΔL_{max} can be estimated by a linear function of the percentage of fast fibers η:

$$\Delta L_{\max} = 0.07\eta + 0.06(1-\eta). \tag{62}$$

The coefficient 0.07 and 0.06 are related to maximum extension of fast fibers and slow fibers in the muscle, respectively [81].

According to the mechanical structure of the Hill-based model shown in Figure 19, the length change of the PE, ΔL_{PE} is identical to the length change of the muscle itself that can be obtained from the OSM. By putting (57), (58), (61) and (62) into (51), F_{PE} becomes:

$$\begin{aligned} F_{PE} &= \left[\frac{F_{PE_{\max}}}{e^{S_{PE}}-1}\right]\left[e^{\frac{S_{PE}\Delta L_{PE}}{\Delta L_{PE_{\max}}}}-1\right] \\ &= \left[\frac{0.05\cdot F_{CE_{\max}}}{e^{S_{PE}}-1}\right]\left[e^{\frac{S_{PE}\Delta L_{PE}}{(1+0.07\eta+0.06(1-\eta))L_{PE_0}-\left(L_{CE_o}+L_{T_s}\right)}}-1\right]. \end{aligned} \tag{63}$$

From (48), the length change of the SE is determined as:

$$\Delta L_{SE} = \Delta L_{PE} - \Delta L_{CE}. \tag{64}$$

In the same manner as the PE, the force value of the SE can be derived by putting (59) and (60) into (51),

$$F_{SE} = \left[\frac{F_{SE_{\max}}}{e^{S_{SE}} - 1}\right]\left[e^{\frac{S_{SE}\Delta L_{SE}}{\Delta L_{SE_{\max}}}} - 1\right] = \left[\frac{1.3 \cdot F_{CE_{\max}}}{e^{S_{SE}} - 1}\right]\left[e^{\frac{S_{SE}(\Delta L_{PE} - \Delta L_{CE})}{0.03 \cdot L_{T_s}}} - 1\right]. \tag{65}$$

On the other hand, the solution of the Hill-based muscle model F_{CE} is fully represented by putting (53)-(56) into (52). The velocity of the CE can be approximated by numerical differentiations:

$$V_{CE} = \frac{\Delta L_{CE}[n] - \Delta L_{CE}[n-1]}{\Delta t}, \tag{66}$$

where Δt is the sampling time of the Hill-based muscle model code. As a result, the full description of the F_{CE} formula is given by:

$$F_{CE} = \frac{0.1433 \cdot a \cdot \exp\left[-0.5\left(\frac{\frac{\Delta L_{CE}[n]}{L_{CE_o}} - \phi_m}{\phi_v}\right)^2\right] \cdot F_{CE_{\max}}}{0.1074 + \exp\left[-1.3\sinh\left(\frac{2.8}{L_{CE_o}(a+1)(1+4\eta)} \cdot \frac{\Delta L_{CE}[n] - \Delta L_{CE}[n-1]}{\Delta t}\right) + 1.64\right]}. \tag{67}$$

Since both (65) and (67) are functions of ΔL_{CE}, by substituting (65) and (67) into (49), $\Delta L_{CE}[n]$ can be solved, which is the only unknown in the equation. In order to solve

the highly nonlinear equation, the Brent's method [82] that is a combination of bisection, secant and inverse quadratic interpolation methods is applied with a MATLAB built-in function, fzero.m. The physiological parameters required to solve the Hill-based muscle model are listed in Table 9 with their nominal values. The first four parameters are based on [78, 83] while the rest are set as described in [17]. According to Winter and Stark [83], the maximal force of the CE depends on the physiological cross-sectional area A_{pcs} and can be expressed as:

$$F_{CE_{\max}} = (0.5\text{MPa})\, A_{pcs}. \tag{68}$$

Therefore, the cross-sectional area A_{pcs} is listed in Table 9 instead of $F_{CE_{\max}}$.

Table 9. Nominal parameters of the Hill-based muscle model based on [17, 78, 83]

Muscle	A_{pcs} (cm^2)	L_{CE_o} (cm)	L_{T_s} (cm)	η (%)	ϕ_m	ϕ_v	S_{SE}	S_{PE}
DLT_c	8.41	14.68	1.64	50	0.05	0.19	3	8
DLT_a	56.38	6.69	8.56	50	0.05	0.19	3	8
DLT_s	17.19	17.02	5.93	50	0.05	0.19	3	8
BIC_s	13.99	13.07	22.98	55	0.05	0.19	2.8	9
BIC_l	11.91	15.36	22.93	55	0.05	0.19	2.8	9
TRC_{lg}	19.07	15.24	19.05	65	0.05	0.19	2.3	10
TRC_m	18.78	4.90	12.19	65	0.05	0.19	2.3	10
TRC_{lt}	38.45	6.17	19.64	70	0.05	0.19	2.3	10

2.5.4. Force sharing among synergistic muscles

Among selected muscles shown in Table 8, the surface EMG is measured only from four muscle groups (i.e., DLT_c, DLT_s, BIC_l and TRC_l) as introduced in Section 2.5.1. It is

assumed that the EMG signal pattern is identical within the same muscle group (e.g., BIC_s and BIC_l shares the same EMG pattern) with different nonlinear scale factor A [17]. Therefore from captured four channels of the EMG, forces of muscles listed in Table 9 can be estimated by the Hill-based muscle model explained in the previous section.

In order to estimate forces of remaining muscles (i.e., PMJ_c, LTD_t, DLT_a and BRA) without additional EMG channels, the force sharing method based on the maximal endurance stress criterion proposed by Crowninshield and Brand [84] is adopted. This criterion distributes force contributions among synergistic muscles (e.g., BIC_l, BIC_s and BRA) for the elbow flexion torque) in accordance to their physiological cross-sectional area A_{pcs} to minimize the average stress on those muscles. Binding *et al*., [85] improved the force sharing criterion with varying moment arm values to estimate the i-th muscle force F_i as:

$$F_i = \left(\frac{b_i}{b_\Sigma}\right)^{1/2} \left(\frac{A_{pcs,i}}{A_{pcs,\Sigma}}\right)^{3/2} F_\Sigma, \tag{69}$$

where the subscript Σ indicates the summed value of all synergistic muscles except the i-th muscle. Here, $A_{pcs,\Sigma}$ and F_Σ are derived as simple summations of parameters of each muscle while b_Σ requires an approximation to find the equivalent value given by

$$b_\Sigma = \frac{\tau_\Sigma}{F_\Sigma}, \tag{70}$$

where τ_{Σ} refers to the joint torque contributed by all synergistic muscles except the muscle *i*.

Based on the spanned joint DOF of PMJ_c, LTD_t, DLT_a and BRA muscles shown in Table 8, their force values are derived by the force sharing criterion as:

$$F_{PMJ_c} = \left(\frac{b_{PMJ_c} F_{DLT_c}}{\tau_{DLT_c}} \right)^{1/2} \left(\frac{A_{pcs,PMJ_c}}{A_{pcs,DLT_c}} \right)^{3/2} F_{DLT_c}, \tag{71}$$

$$F_{LTD_t} = \left(\frac{b_{LTD_t} \left(F_{DLT_s} + F_{TRC_{lg}} \right)}{\tau_{DLT_s} + \tau_{TRC_{lg}}} \right)^{1/2} \left(\frac{A_{pcs,LTD_t}}{A_{pcs,DLT_s} + A_{pcs,TRC_{lg}}} \right)^{3/2} \left(F_{DLT_s} + F_{TRC_{lg}} \right), \tag{72}$$

$$F_{DLT_a} = \left[\frac{b_{DLT_a} \left(F_{DLT_c} + F_{DLT_s} \right)}{\tau_{DLT_c} + \tau_{DLT_s}} \right]^{1/2} \left[\frac{A_{pcs,DLT_a}}{A_{pcs,DLT_c} + A_{pcs,DLT_s}} \right]^{3/2} \left(F_{DLT_c} + F_{DLT_s} \right), \tag{73}$$

$$F_{BRA} = \left[\frac{b_{BRA} \left(F_{BIC_l} + F_{BIC_s} \right)}{\tau_{BIC_l} + \tau_{BIC_s}} \right]^{1/2} \left[\frac{A_{pcs,BRA}}{A_{pcs,BIC_l} + A_{pcs,BIC_s}} \right]^{3/2} \left(F_{BIC_l} + F_{BIC_s} \right), \tag{74}$$

where each row is computed for the negative shoulder azimuth (- α), the positive shoulder azimuth (+ α), the shoulder elevation (+ β) and the elbow flexion (+ δ), respectively.

2.5.5. Parameter optimization of the myoprocessor

In order to get the best estimation, parameters of each myoprocessor for selected 11 muscles (see Table 8) need to be adjusted for each individual. Eleven parameters are optimized for this purpose: 1) the nonlinear scale factor of the EMG processing module, *A*, 2) a gain G_b and an offset O_b of the varying moment arm b_{ij} computed from the OSM,

and 3) eight physiological parameters of the Hill-based muscle model listed in Table 9. The optimization is achieved by the genetic algorithm as described in [17] via ga.m MATLAB built-in function for its high chance to find global minima. Upper and lower bounds for the parameters are shown in Table 10. In the table, the superscript ^{n} indicates the nominal value of the parameter. After the optimization, all parameters for the myoprocessor are substituted by the optimized value except the varying moment arm b_{ij}, which requires an additional computation:

$$\tilde{b}_{ij} = G_b b_{ij} + O_b. \tag{75}$$

Table 10.Boundary values of myoprocessor parameters based on [17]

Parameter	Lower bound	Upper bound
A	-3	0
A_{pcs} (cm^2)	$0.5A^n_{pcs}$	$1.5A^n_{pcs}$
L_{CE_o} (cm)	$0.8\,L^n_{CE_o}$	$1.2\,L^n_{CE_o}$
L_{T_s} (cm)	$0.8\,L^n_{T_s}$	$1.2\,L^n_{T_s}$
η (%)	25	75
ϕ_m	-0.1	0.1
ϕ_v	0.09	0.8
S_{SE}	$0.8\,S^n_{SE}$	$1.2\,S^n_{SE}$
S_{PE}	$0.8S^n_{PE}$	$1.2\,S^n_{PE}$
G_b	0.8	1.2
O_b (mm)	-10	10

The fitness function of the genetic algorithm optimization is determined as the root mean square of the error between estimated joint torques each from the inverse dynamics module, τ_{ID} , and the myoprocessor, τ_{Myo} (see 'Error' and a red dashed arrow in Figure 8):

$$e_{\text{rms}} = \sqrt{\frac{1}{N}\sum_{k=1}^{N}\left(\tau_{ID}[k] - \tau_{Myo}[k]\right)}, \tag{76}$$

where N is the total number of data point and k is the index of a data point. The inverse dynamics torque τ_{ID} is derived in (31) while the myoprocessor torque τ_{Myo} can be obtained by

$$\tau_{Myo,j} = \sum_{i} F_i \cdot b_{ij}, \tag{77}$$

where subscripts i and j are indices of the muscle and the joint.

In order to obtain the accurate inverse dynamics torque τ_{ID} as a reference, three calibration postures are designed as follows: 1) 90° elbow flexion (see Figure 20(a)), 2) full elbow extension with the backward shoulder elevation (see Figure 20(b)), and 3) 90° shoulder abduction (see Figure 20(c)). For each calibration posture, surface EMG signals of biceps (BIC_l), triceps (TRC_{lg}) and deltoids (DLT_c and DLT_s) are respectively acquired three times with different contraction levels: 1) natural posture, 2) maximal contraction, and 3) posture with holding 8 lbs of dumbbell. Only the posture with holding 8 lbs dumbbell is implemented in the genetic algorithm optimization and the normalized EMG input $u(t)$ is obtained to eliminate the limb dynamics

$$u(t) = \frac{|w_{8lbs}(t)| - |w_{nat}|_{avg}}{\max(|w_{\max}|)}, \tag{78}$$

where $|w_{8lbs}(t)|$ is the fully rectified value of the filtered EMG at time t. $|w_{nat}|_{avg}$ and $\max(|w_{max}|)$ present average magnitude of the EMG at natural contraction and maximum magnitude of the EMG at maximal contraction, respectively. With an assumption that all postures are static during the data acquisition, the reference joint torque is given by:

$$\tau_{ID} = 8[\text{lbs}] \cdot 0.45\left[\frac{\text{kg}}{\text{lbs}}\right] \cdot 9.81\left[\frac{\text{m}}{\text{s}^2}\right] \cdot l[\text{m}], \tag{79}$$

where l is the equivalent link length for each calibration posture (i.e., the forearm link length for the elbow flexion posture, and the whole arm length for the elbow extension and shoulder abduction postures). For the elbow flexion posture, parameters of BIC_l, BIC_s and BRA muscles are optimized while the elbow extension posture optimizes TRC_{lg}, TRC_m and TRC_{lt}. Remaining muscles, DLT_c, DLT_a and DLT_s are optimized by the shoulder abduction posture.

For a validation purpose, the described parameter optimization with the proposed calibration postures was implemented. Figure 21 shows optimization results in each calibration posture by comparing the estimated myoprocessor torque τ_{Myo} with the reference τ_{ID}. In each subfigure, a red dashed line, a blue dotted line and a black continuous line indicate the reference torque, the estimated torque with nominal

parameters and the estimated torque with optimized parameters, respectively. As shown in the figure, the estimated joint torque approximates the reference torque with higher accuracies after the optimization compared to nominal parameters.

(a) Elbow flexion (BIC_l) **(b) Elbow extension (TRC_{lg})** **(c) Shoulder abduction (DLT_c and DLT_s)**

Figure 20. Myoprocessor calibration postures

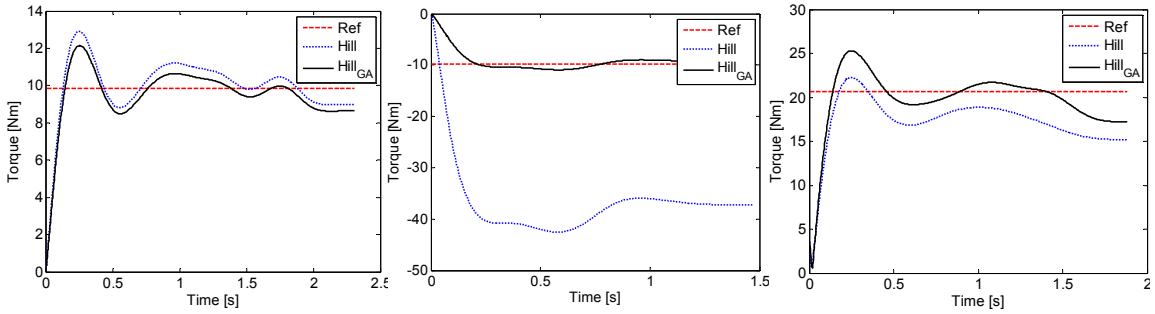

(a) Elbow flexion **(b) Elbow extension** **(c) Shoulder abduction**

Figure 21. Experimental validation of the parameter optimization

3. EXPERIMENTAL OBSERVATIONS ON HUMAN REACHING COORDINATION WITH AND WITHOUT A REDUCED MOBILITY*

3.1. Introduction

Human arms perform versatile reaching motions in daily activities to achieve complex desired position and orientation of the end-effector (i.e., hand). Although it seems effortless, producing such limb motions always involve a branch of redundant mapping problems, so-called degrees of freedom problem, described by Bernstein [86]: how does the CNS (central nervous system) solve the complex problem of motor control without conscious effort to complete skillful actions? This question can be interpreted within the human point-to-point reaching process as presented in Figure 22.

There are two redundancy problems in the overall process of the point-to-point reaching. The human subject sets the target point as the final hand location in the workspace (usually with respect to the visual coordinates) while the current configurations (e.g., hand location and arm posture) are perceived by the sensory inputs (i.e., visual and proprioceptive information). Assume that there is no external contact during the reaching

---

* Part of this section is reprinted, with permission, from "Human Arm Motion Planning Against a Joint Restriction" by H. Moon *et al*., 2012, in Proc. of the *IEEE Int. Conf. on the Biomedical Robotics and Biomechatronics*, pp. 401-406, ©2012 IEEE, "Experimental Observations on the Human Arm Motion Planning Strategy under an Elbow Joint Constraint" by H. Moon *et al*., 2012, in Proc. of the *34th Annual Int. Conf. of the IEEE Engineering in Medicine & Biology Society*, pp. 3870-3873, ©2012 IEEE, "An Experimental Study on Redundancy Resolution Scheme of Postural Configuration in Human Arm Reaching with and Elbow Joint Kinematic Constraint" by H. Moon *et al*., 2014, in Proc. of the *IEEE Middle East Conf. on Biomedical Engineering*, pp. 257-260, ©2014 IEEE, and "Experimental Observations on the Central Nervous System's Governing Strategies on the Arm Reaching with Reduced Mobility" by H. Moon *et al*., in Proc. of the ASME Int. Mechanical Engineering Congress & Exposition, vol. 2, pp. 483-492, © 2012 ASME.

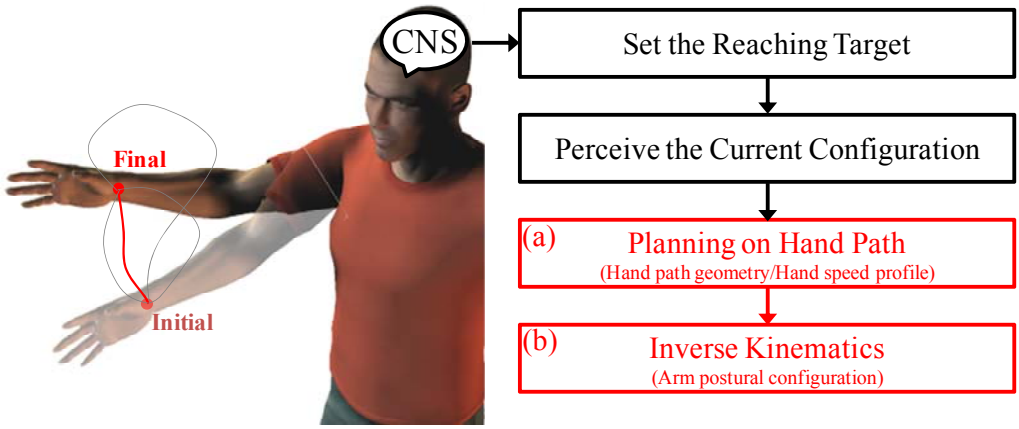

Figure 22. Schematic plot on overall procedures of the point-to-point reaching (reprinted from [87] with permission after modifications).

motion so that the subject's CNS does not need to incorporate obstacle avoidance or direct force control (i.e. controlling the contact force and moment to desired value with explicit closure of a force feedback loop [88]). Then the overall control procedure can be modeled as a position mode control of the human arm as a serial linkage manipulator. Since the main objective of the point-to-point reaching is maneuvering the end-effector to a certain position in the workspace, the subject's hand naturally gets the greatest attention of the CNS [89]. Therefore, in order to fill out the gap between the initial and the final task points in the workspace, the point-to-point reaching needs to be planned in a hand trajectory format. In this process, the first redundancy problem occurs when the geometry and the speed of hand trajectory should be selected among infinite numbers of possible ways and their combinations (see Figure 22(a). Grey hand paths indicate possible candidates while the red path describes a patterned path generated by the CNS). Once the hand trajectory is determined, the CNS needs to configure the arm posture by resolving another redundant

mapping problem (see Figure 22(b)) to generate control commands for each controlling DOF. As an example, the arm posture can be fully specified in the joint space by solving the corresponding inverse kinematics problem. Note that the number of independent joint DOF is greater than the sufficient six DOF needed to specify the hand kinematics in a spatial workspace (three positions and three orientation angles). Furthermore, on the actuation level, the redundancy of the problem is magnified due to multiple connections of skeletal muscles spanned over each joint DOF motion.

What is the best explanation for the efficient and optimal problem solving ability of the CNS? From many experimental observations, it is generally accepted that governing rules (either innate or learned) in the CNS impose some additional constraints and induce a finite set of preferred patterns (e.g., the tendency of synchronizing inter limb coordination [90]). Such governing rules can be observed from the experimental results and approximated as computational models. Multitude models have been studied to approximate behaviors of such governing rules in the point-to-point reaching actions. Most of them fall into either minimum principles or data fitting formats as presented in Section 3.3.

In the experiment, a kinematic constraint on the elbow joint DOF (i.e., elbow locked in place) is imposed for the purpose of explained in 2). This condition constraints the arm workspace on a curved surface which affects the hand trajectory formulation process. The author believes that the loss of arm mobility also affects the second redundancy problem: arm posture configuration along the hand path. Therefore, it is expected that the experimental observations in this study will enable us to tap into

fundamental principles of the human arm reaching coordination by disturbing both of redundancy problem solving processes within the CNS. Note that this study is based on the assumption that even though the imposed physical constraint can yield adaptations in resulting motions, the governing rules are preserved in the CNS and induce invariant features in the motion kinematics and dynamics. This assumption is supported by the observations on the motor recovery for reaching in stroke patients. Roby-Brami *et al*., [91] found that the stroke patients seek a way to recover the original control strategies through therapeutic arm reaching tasks against their physical impairments.

Some experimental studies have been conducted on the arm reaching on a non-planar curved surface. In their reaching experiments on a hemispheric constraint surface, Sha *et al*., [92] showed that a healthy subject preserved a bell–shaped velocity profile while the hand paths approached to the geodesic curves (i.e., shortest path on the constraint surface) by training. Liebermann *et al*., [93] characterized the hand trajectories on a similar workspace constrained on a hemisphere by a mechanical linkage system. From the similar experimental results, they came up with a different conclusion on the hand path geometry that it may follow the smoothest paths (i.e., rhumb lines on the hemispheric surface) rather than the shortest paths (i.e., geodesic curves). The temporal characteristic (i.e., smooth bell-shaped velocity profiles), however, was preserved regardless of the hand path geometry. Based on the above studies, it is considered that the CNS keeps the governing rules while it generates adapted hand paths against the constrained hand kinematics due to extrinsic factors (e.g., contact specified tasks such as surface welding). However, the reaching constrained on the curved surface only affects the first redundancy problem (i.e.,

the hand path formulation, see Figure 22(a)) due to fully applicable arm mobility in the joint DOF space.

3.2.Background Knowledge on Motor Neuroscience

In this section, an overview on the entire processes of human reaching is presented. In his work, Brooks [89] classified the CNS into two interactive functional subsystems: limbic and sensorimotor systems. For the motion generation, the limbic system deals with emotional needs (i.e., feeling and desire) by recognizing the significance of a need-initiated stimulus while the sensorimotor system governs the perception and motor functions. In his work, the link between two subsystems is explained as follow: the "*need-directed motor activity*" initially formulated in the limbic system is converted into overall plans for the "*goal-directed motor actions*" in the highest level hierarchy of sensorimotor system [89]. As two interconnected systems are recruited together in motor coordination, this dissertation tries to include a part of such interactions by the limbic system intervention in the sensorimotor system in the proposed computational model.

3.2.1. In which representation the motion is characterized? Kinematics or dynamics?

There is a question in which representation the reaching motion is characterized, kinematics or dynamics? It seems that the kinematics and dynamics of reaching motion can be independently controlled. In their study on the limb position drift during repetitive reaching, Brown, *et al*., [94] showed that the dynamics (joint torque pattern) can be independently adapted to maintain the kinematics of motion.

Without any specially imposed instructions regarding the dynamics of motion (e.g. hit the object with a certain amount of force or maintain the end–effector force vector during reaching), it can be argue that the arm reaching is first planned with respect to the kinematic representation due to its primary function, locating the hand as desired. Note that the hierarchical control structure [89] supports the idea in a way that the plant dynamics is separately controlled by the motion execution loop. However, the dynamic representation is considered equally important in the motion planning process. In his feedback error learning model, Kawato [95] explains that accurate feed forward control commands in skillful motions are due to a well-trained internal model (i.e., inverse dynamics model) of the neuromuscular system.

It is considered that the motion execution process is governed by the dynamic representation of motions. As feedback delays of sensory organs (e.g., muscle spindles, joint receptors and vision) are significant as presented in Section 3.2.3, a direct feedback control by sensory inputs (mostly kinematic information) is not dominant. On the other hand, as Desmurget and Grafton [96] proposed, forward dynamics model with an efferent copy of motor command signal can enable the CNS to control fast reaching movements by a feedback control.

3.2.2. In which coordinate system the motion kinematics is defined in the CNS?

Extrinsic or intrinsic?

In which coordinate system this motion kinematics is defined in our CNS, extrinsic (e.g. Cartesian coordinates) or intrinsic (e.g. joint or muscle coordinates)? As stated by Hogan [97], *"One way to address this question is to look for patterns or regularities in motor*

behavior". According to the Bernstein's hypothesis, the motion information formulated in higher levels of the CNS has projections of extrinsic space rather than intrinsic joints and muscles over lower levels of CNS activities [86]. Morasso [98] supports the idea from his observations on horizontal reaching experiments that the reaching pattern is relatively well organized with respect to the hand motion in the task space due to the invariant movement features, straight hand path with a single peaked velocity, while no patterns or regularities were observed in the joint space. Also, in his explanations on the consistent one peaked hand velocity profile of the reaching, Brooks [89] mentioned that *"This property is applied to the path of the object of greatest attention of the central nervous system for intended multi-joint movements"*. Since arm reaching motions are brought mainly for a final hand manipulation or a grasping task, the greatest attention of the CNS naturally occurs on the hand (i.e. end-effector) paths. In addition, regarding the joint paths, Brooks [89] described that *"They are not necessarily continuous since they are fitted to support the intended hand path"*.

On the other hands, Soechting and Lacquaniti [99, 100] report that invariant features of movements can be observed in joint coordinates that the ratio of joint angular velocities (elbow to shoulder) tends to be constant in the deceleration phase. After this finding, Soechting and his colleagues [101-103] insist the shoulder-centered coordinate system based on their observations on pointing experiments. In their earlier studies, they showed that systematic errors of pointing arise from the transformation of perceived target position in extrinsic coordinates into intrinsic coordinates, and these errors are centered at the shoulder joint [101, 102]. In a later study, they argue that there exist both head-centered

and shoulder-centered coordinates to represent the target position in the CNS from experimental error analysis results [103].

Multiple experimental studies found that the hand path curvature is depending on movement directions (e.g., forward/backward, left/right or vertical) [104-106], and it seems that joint coordinates can better explain such characteristics than task coordinates. In order to explain such phenomenon, Klein Breteler *et al*., [107] proposed that the variance of hand path curvatures can be explained more consistently with the motion planning in joint coordinates than in task coordinates. In order to explain straight hand paths in joint coordinates, Hollerbach *et al*., [108] proposed the strategy of "*staggered joint interpolation*", which approximates the straight hand path by scaling the amplitude and the duration of individual joint angular velocity profile.

Against the hypothesis that the motion is planned in joint coordinates, Hogan [97] argues that two observations are not explained with the joint coordinates hypothesis: 1) lack of patterns or regularities of motion in the joint space, and 2) common experimental observations that are against the joint coordinates hypothesis (especially the *staggered joint interpolation* [108]). Even though there are up to date opinions that support the motion planning in joint coordinates (e.g. [90, 107, 109]), the hypothesis of the motion planning in hand coordinates (or extrinsic task coordinates) is accepted in this dissertation for neuronal evidences observed from primate cortex activities along the hand motion [110-114]. Also, note that this hypothesis is in accordance with the general path planning algorithm in the conventional robotics control [115].

3.2.3. Human sensorimotor system from the control engineering viewpoint

Figure 23 represents a simplified control structure of the human sensorimotor system for a point-to-point reaching from the control engineering viewpoint. In the figure, $x_{d,final}$ indicates the final task point, $x_d(t)$ is the desired hand trajectory in the task coordinates and $\theta_d(t)$ refers to the desired trajectory in the joint coordinates. $\omega_d(t)$ and $\alpha_d(t)$ represent desired joint angular velocity and acceleration, respectively. For its control command, $u_{ff}(t)$ and $u_{fb1}(t)$ respectively indicate the feed forward and the sensory feedback control commands while $u_{fb2}(t)$ is the rapid feedback control command. The total control command $u(t)$ is equal to sum of all control commands. For its sensory inputs, $x_a(t)$ and $\theta_a(t)$ are the actual hand motion in the visual sensory input and the actual joint motion in the proprioceptive input, respectively. Motion errors, $e_x(t)$ and $e_\theta(t)$ are represented in the task coordinates and the joint coordinates, respectively. d_u is the exogenous disturbance input, ξ_x is the measurement noise in the visual input and ξ_θ is the measurement noise in the proprioceptive input. According to the diagram, the desired final task point $x_{d,final}$ is determined in a higher (or conscious) level of the CNS and is projected onto the hand path planning module (see Figure 23(a)). In this module, the desired hand trajectory $x_d(t)$ is planned as a function of time t. In order to specify the actual control command in an internal body space (joint DOF is considered in this paper), $x_d(t)$ is converted into the reference trajectory of intrinsic control coordinates by the inverse kinematics module (see Figure 23(b)). Here, the joint trajectory $\theta_d(t)$ is considered for its relative simplicity compared to the muscle length or motor neuron activities. Then the feed forward control command $u_{ff}(t)$ is computed by the internal inverse dynamics model (see Figure 23(c))

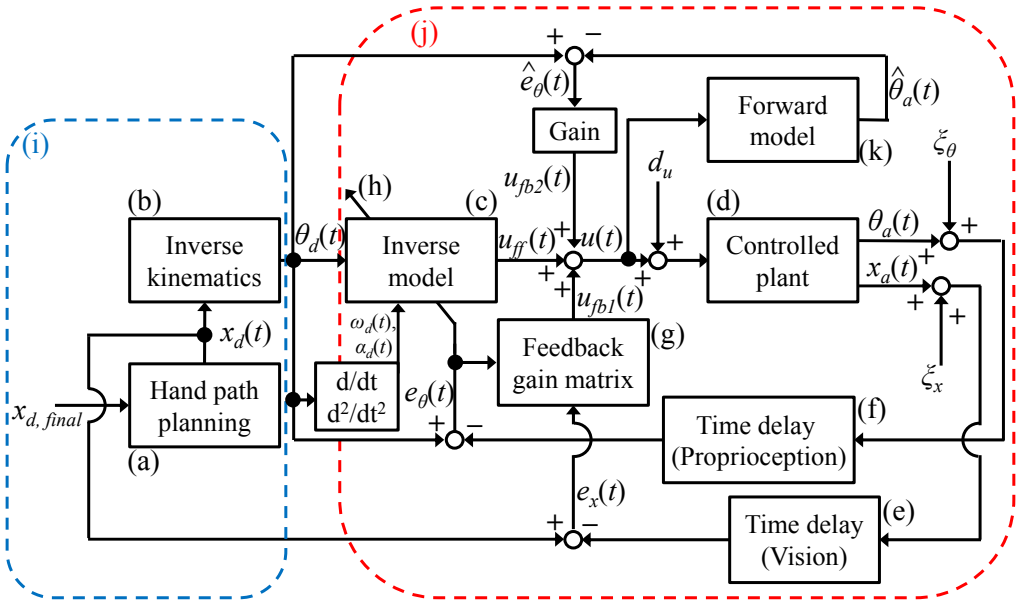

Figure 23. Simplified control structure of human sensorimotor system on point-to-point reaching (reprinted from [87] with permission after modifications).

with the given desired joint kinematics. The actual hand motion $x_a(t)$ and joint motion $\theta_a(t)$ generated from the controlled plant (i.e. human body dynamics, see Figure 23(d)) are sensed by the vision and the proprioception, respectively. The motion errors, $e_x(t)$ and $e_\theta(t)$, which become inputs of the feedback loops, are computed from the desired motion kinematics and the sensed motion output after respective time delay effects (see Figure 23(e) and Figure 23(f)): 150~250 ms for the visual feedback on $x_a(t)$ and 30~50 ms for the spinal feedback of the proprioception on $\theta_a(t)$ [116]. Due to the large delays, the magnitude of feedback gain matrix (see Figure 23(g)) cannot be large to avoid the system instability [116]. For this reason, the feed forward signal $u_{ff}(t)$ dominates the feedback signal $u_{fb1}(t)$ for well-trained movements. There are studies support the existence of the internal forward dynamics model (see Figure 23(k)) that estimates the resulting sensory inputs from the

efference copy of the motor command $u(t)$. In their review paper, Desmurget and Grafton [96] shows the possibility and the evidence of a rapid feedback control enabled by the forward dynamics model. In this study, however, we assume that such rapid feedback $u_{fb2}(t)$ cannot be physically faster than the $u_{ff}(t)$, which is reasonable in the sense of control engineering.

The overall control structure shown in Figure 23 can be classified into two main processes, motion planning process (see Figure 23(i)) and motion execution process (see Figure 23(j)), by which motion characteristics is dominant, kinematics or dynamics. Note that it is assumed that those two motion characteristics can be independently controlled in the CNS (e.g., the study of Brown *et al*., [117]). Based on this independency, it is considered that motion planning and actual execution processes are independently developed in the CNS, and the Figure 23 proposes that the point-to-point reaching is planned mostly in terms of motion kinematics while the motion execution process handles plant dynamics to realize the planned motion. Brooks [89] supports the idea with his hierarchical structure of the entire motion processes based on physiological findings. According to his concept, reaching is planned in the highest level hierarchy (i.e., motion planning process) and is executed in the middle and the lowest levels (i.e., motion execution process). However, not like conventional deterministic models surveyed in Section 3.3.2.1, governing rules are implemented in overall process without distinct separations. Instead, the degree of dominance of each governing rule is manifested according to motion specifications.

The idea is also supported by physiological, neuroimaging and experimental evidence that the cerebellum in the middle level hierarchy has a significant relationship with the formation of internal models (see Figure 23(c) for an example) within the motion execution process [118-121]. It can be considered that the governing rules are implemented mostly in the motion planning process rather than in the motion execution process for the following reasons:

1) Each module in the motion planning process (see Figure 23(a, b)) is directly linked to the corresponding redundancy problem of motion generation (see Figure 23(a, b)), and
2) From the control engineering perspective shown in Figure 23, the governing rules can keep their simplicity by being separated from the disturbances and uncertainties of the controlled plant (e.g., time varying body dynamics, noise in neural signals and changing actuator dynamics due to muscle fatigue).

However, in order to explain the sensorimotor system intervened by the limbic system in a unified way, it is assumed that governing rules are not separately implemented either in the motion planning process or the motion execution process. Instead, the degree of manifestation of each governing rule is modulated in accordance to the reaching context in the proposed computational model.

In reaching motions, the elbow joint governs the distance control of the hand, which can be explained by the fact that the hand keeps a constant distance from the shoulder when the elbow joint is locked. Therefore, the point-to-point reaching with the elbow joint constraint may require a similar control process in the CNS as for the reaching

on a frontal plane without the joint restriction. The experimental setup in this study is also designed to let the subjects focus on the hand directional control without effort on the hand distal control. In other words, the imposed elbow constraint condition does not induce much of learning or adaptation in the CNS. Recall that the feed forward control command dominates the feedback signal for well-trained motions (i.e., the internal inverse dynamics model depicted in Figure 23(c) is already established and tuned enough accurate). Therefore, in order to observe the governing rules implemented in the motion planning process, features induced by the desired motion kinematics (i.e., desired joint angle $\theta_d(t)$, joint angular velocity $\omega_d(t)$ and angular acceleration $\alpha_d(t)$) and the feed forward control signal $u_{ff}(t)$ should be extracted from the captured motion kinematics $x_a(t)$ and $\theta_a(t)$.

3.3. A Literature Survey on Computational Model on Human Arm Reaching

In order to answer the Bernstein's degree of freedom question [86], enormous studies have been elaborated with various approaches. Campos and Calado [122] present a nice review on computational models on human arm movement control. Based on their categorization, selected computational models on the point-to-point reaching are reviewed in this section.

3.3.1. Descriptive models

As human arm motions are generated in a highly stereotyped solution sets, some initial studies tried to approximate such patterns based on empirical observations. Morasso [98] found some consistent kinematic characteristics of the hand trajectories, such as straight paths with bell-shaped velocity profiles, during the point-to-point reaching on the horizontal plane.

Another empirically found regularity of the hand speed profile has been confirmed from the isogony principle in writing and drawing tasks: hand trajectory proceeds equal angles in equal times [123]. Based on this finding, Lacquaniti *et al*., [124] formulated the two-third power law that represents the instantaneous hand velocity as a power function of path curvature in 2D motions.

Fitt's law is the well-known empirical relation between the movement time and the relative difficulty of the reaching (or pointing), which can be quantified by the distance and the dimension of the target [125]. In this law, the movement time for a reaching can be estimated as a log-scale fitting model that is proportional to the index of difficulty based on the information processing theory.

3.3.2. Minimum principles

Beyond descriptions of empirical relations, later studies tried to extend the computational model work to understand the underlying principles of the CNS. From consistent experimental findings on the highly patterned kinematics of arm movements, it was considered that certain movements are preferably chosen by the CNS for satisfying some efficiency criterion. Such selections are similar to a process of cost function minimization. In this context, Engelbrecht [126] categorizes those efforts as minimum principles named after the minimum theories in a variety of science and mathematics fields.

3.3.2.1. Deterministic models

There are a number of researchers who focused on the kinematic aspect of the reaching. From their experimental observations, Flash and Hogan [127] confirmed the Morasso's finding (i.e., a straight hand path and a bell-shaped hand speed profile) and approximated

such hand kinematics in 2D reaching with a mathematical model, the minimum jerk (MJ) model. This MJ model stresses on the smoothness of natural human motions by minimizing the hand jerk along the motion profile. The authors found that the hand kinematics follows similar rules for the via-point reaching case (i.e., intermediate point passing or obstacle avoidance) as well by observing low curvature hand paths joined with a high curvature path around the via-point. Datas *et al.*, [128] supported the same idea by comparing the minimum jerk hand paths with the human experimental data of reaching on the horizontal and the vertical planes. From their model on the 3D reaching motion, Klein Breteler and Meulenbroek [90] assumed that there is a movement optimization scheme in the joint level which makes arm joint rotations in a synchronized manner instead of independently controlling each joint DOF rotation. This model derives full joint profiles by applying the MJ model in joint angular space.

The dynamic properties of arm reaching have been also considered to represent an aspect of the governing rules. By considering the motion dynamics, following models derive their solutions in intrinsic coordinates (e.g., joint or muscle). As a result, full motion outputs (e.g., hand trajectory, joint trajectory and torque) are produced simultaneously. Uno *et al*., [104] proposed the minimum torque change (MTC) model that minimizes the sum of squared joint torque rate of change over time, and compared with the MJ model on various 2D reaching motions. For the point-to-point reaching without a via-point constraint, the MTC model could mimic slightly curved hand paths with smooth speed profiles while the MJ always generated straight paths. Later, the MTC model was corrected as the minimum commanded torque change(MCTC) model by Nakano *et al*.,

[129]. Dornay *et al*., [130] introduced the minimum muscle-tension change (MMTC) model to interpret the indeterminacy problem (i.e., redundant mapping problems introduced in 3.1) in a deeper intrinsic level (i.e., skeletal muscle coordinates) than the MTC model.

Biess *et al.*, [64] introduced a unique computational model of 3D arm reaching. Unlike other optimization models, they obtain an analytic solution of the cost function minimization based on the assumption that optimization principles are separately applied at the geometric and temporal levels of control. In their model, geometric properties (i.e., hand path and posture) are specified by the joint trajectories derived from geodesic curves in the Riemannian configuration space with respect to the kinetic energy metric. Once geometric properties are derived, the temporal property (i.e., speed of the movement) is determined by another independent optimization process that minimizes the squared third time derivative of the selected hand paths' arc length.

Some research groups have focused on the resolution of the arm posture configuration problem (see Figure 22(b)). Kang *et al*., [131] considered mechanical work minimization. Kim *et al*., [132] introduced an interesting concept of effective feeding potential by maximizing a projection of the largest major axis of manipulability ellipsoid on a vector connecting hand and mouth positions. Kashi *et al*., [133] adopted a multi criteria cost function to minimize angular joint displacement and shoulder joint range availability. In order to determine the upper body posture for a given targeting hand position, Yang *et al*., [134] adopted the multi-objective optimization (MOO) scheme. In their work, the cost function is defined as a weighted sum of the joint displacement, the

delta-potential energy and discomfort index to achieve the best estimation as a Pareto-optimal solution [135].

3.3.2.2. Stochastic models

Stochastic models consider more realistic situations of human motor control: noise contaminated neural signals. Harris and Wolpert [136] introduced the minimum variance (MV) model that minimizes the final position variation. By modeling the noise, which increases its magnitude linearly with the amplitude of the motor command signal, the MV model can explain the natural variability of the positioning accuracy at the end point. The MV model successfully captures hand kinematic features such as the Fitt's law and the two-third power law in the motion planning level.

More recently, Todorov and Jordan [137] introduced a new theory, minimum intervention principle (MIP), based on the stochastic optimal feedback control approach. In their MIP, not only the motor signal dependent noise but also the measurement noise of the sensory organs are modeled. From the stochastic optimal feedback control scheme such as the Linear Quadratic Gaussian (LQG) controller, the MIP processes the motion planning and the execution all-at-once in a feedback control structure. As the performance index is defined as a linear combination of state elements (e.g., sum of state elements), the MIP allows the motion variability to be accumulated in task-irrelevant (redundant) dimension [137].

3.3.3. Statistical data fitting models

Despite of the reasonable estimation results shown in deterministic models, the assumed strategies of those approaches originate from intuitive ideas mostly in engineering

perspectives, not from observations on real human motor behaviors. Some other research groups adopted experimental identification methods to develop a machine that mimics human motor behaviors. Zanchettin *et al*., [138] synthesized object manipulation motions by applying clustering and multivariate correlation statistics on experimental results to identify the model with least squares algorithm. Kim *et al*., [139] approximated captured human motions by response surface method to control a biomimetic motion of a humanoid robot. Artemiadis *et al*., [140] modeled the dependencies among joint DOF angles by using the Bayesian network scheme and implemented in a redundant robotic manipulator to generate human-like postures. Since main objective of those experimental identification methods is on direct implementation in robotic systems, they can mimic the human-like motion generation based on probabilistic models of pre-captured data. However, they are limited in understanding and explaining actual principles of arm posture selection within the CNS in a physiological manner.

3.3.4. Computational models on constrained arms

Some previous studies applied computational models to explain reaching with a joint constraint condition. Bullock *et al*., [141] introduced a self-organizing neural model to justify the automatic corrections in the reaching with clamped joints. Rosenbaum *et al*., [142] explained the compensatory reaching motion against the elbow restriction with weighted sum of stored postures in the CNS. Furthermore, to explain the motor equivalence phenomenon (i.e., the ability to complete the desired task with different combinations of controllable DOF [142]), Saltzman and Kelso [143] focused on a task dynamic approach which regards the compensatory strategy as an implicit consequences

of the task dynamics. Mussa Ivaldi *et al*., [144] approached the issue from the equilibrium point control viewpoint.

3.4. Human Arm Model

3.4.1. Human arm kinematics

Human arm kinematics can be simplified as a seven DOF serial SRS (Spherical–Revolute–Spherical) chain (i.e., one–DOF hinge joint at the elbow and three–DOFs ball and socket joints at the wrist and shoulder) as shown in Figure 24(a). Despite its complex anatomical structure, only the glenohumeral joint motion is considered among the shoulder complex kinematics. Each joint DOF is defined as shown in Figure 24(b). Each spherical joint can be decomposed into three orthogonal revolute joints (see $\mathbf{R_{1\text{-}3}}$ for the shoulder and $\mathbf{R_{5\text{-}7}}$ for the wrist in the figure). Denavit-Hartenberg (D-H) notion consists of local frames on each joint DOF is shown in Figure 24(c). The reaching motion can be functionally classified into two tasks: 1) positioning the end-effector to a desired location and 2) finalizing the end-effector task such as, grasping or manipulating a hand held object. From the experimental findings, it is pondered that the CNS switches the focus of control from 1) to 2) when the hand is closely approached to the final goal position [89]. To focus on the first task, this paper considers only the position of the hand, which is delivered by the shoulder and elbow DOFs. The wrist DOFs are not taken into account in this study since they are dominant for the hand orientation. The hand position is defined as the position of the wrist center (see $\mathbf{O_m}$ in Figure 24(c)). When the elbow joint DOF is restricted and the trunk is constrained to move, the kinematic structure of the arm changes to a serial SS

(Spherical– Spherical) chain, characterized by a spherical workspace, centered at the shoulder joint. The reconfigured SS chain is assumed to be a virtual link with a length *d* that connects the shoulder (center of the sphere) and the wrist (hand position).

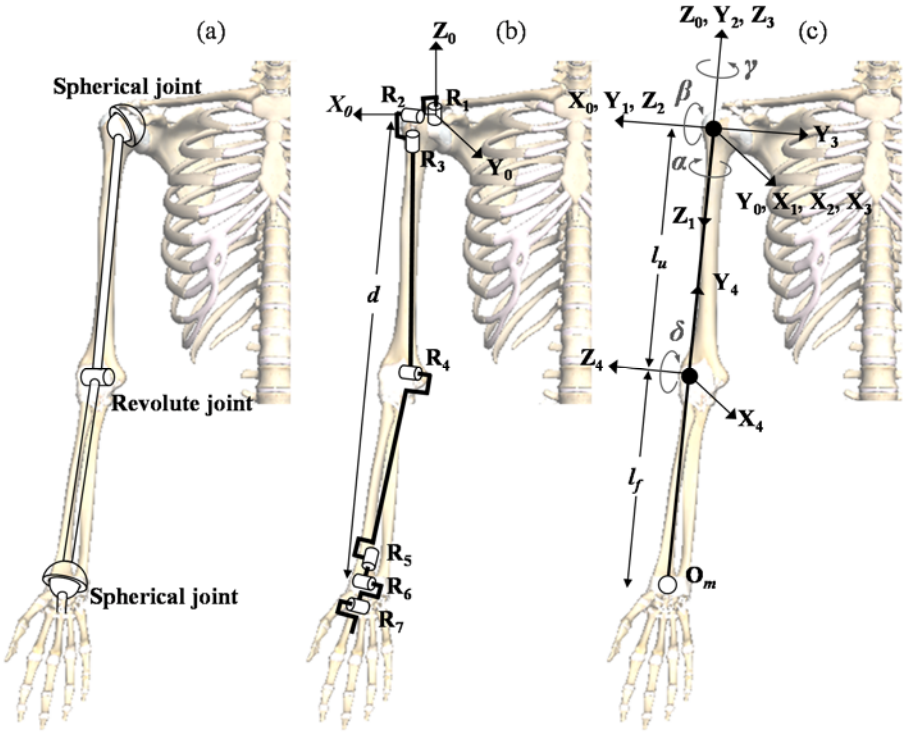

Figure 24. Simplified kinematic structure of human arm (reprinted from [87, 145] with permission after modifications).
(a) Joint mechanism configuration.
(b) Each joint DOF (degree of freedom) configuration. R_1, R_2 and R_3 represent the shoulder azimuth, elevation and humeral rotation DOFs, respectively. R_4 indicates the elbow flexion DOF. Wrist DOFs (i.e. forearm supination/ pronation, wrist flexion/extension and ulnar/radial deviations) are described by R_5, R_6 and R_7 respectively.
(c) Denavit–Hartenberg (D–H) notion for the simplified human arm kinematics. Defined end–effector position located on the center of wrist joint is represented as O_m. For the shoulder joint, α is elevation, β is azimuth and γ is humeral rotation. δ indicates the elbow flexion, l_u and l_f represent the link length of upper arm and forearm, respectively.

3.4.2. Two different coordinate systems for interpretations of motions with an elbow constrained arm

Two different coordinate systems are defined to interpret the motion kinematics with respect to the task and the body centered coordinates, respectively. As mentioned earlier, we are discussing the case where the arm reachable workspace is constrained on a spherical surface around the shoulder when the elbow joint DOF is locked. To derive the hand path geometry on the constrained workspace with the minimum number of variables, extrinsic task coordinates (ETC) are adopted as spherical coordinate system centered at the shoulder/glenohumeral joint (see Figure 25(a)). In the figure, a virtual link connecting the shoulder and the wrist position is drawn as a thick solid line and guidelines for representing spherical workspace are drawn as grey thin lines. The latitude θ is defined as the angle of the virtual link with respect to the X_0-Y_0 plane and longitude ϕ is an angle of the virtual link projected on the X_0-Y_0 plane measured from positive Y_0 axis (see Figure 25(a) for the clarification).

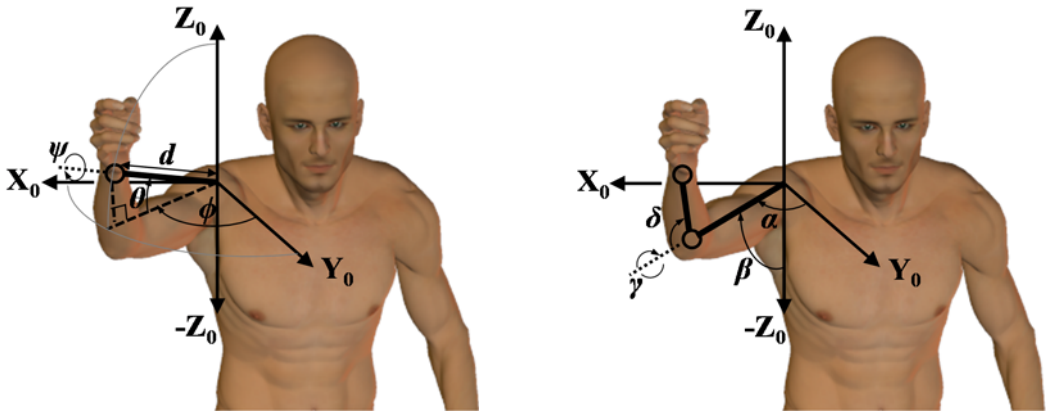

(a) Extrinsic Task Coordinates (ETC). (b) Intrinsic Joint Coordinates (IJC).

Figure 25. Two coordinate systems (reprinted from [146] with permission).

It is supported by multiple studies that reaching motions in terms of the hand kinematics are planned in task coordinates [89, 97, 98]. In addition, there is evidence that neural activities in the primate brain and hand direction are closely related in reaching motions [113, 114]. For a determined hand position, the arm posture varies with respect to the elbow position which can be laid on a circle around the virtual link connecting the shoulder and the hand [64, 147]. In ETC, the elbow swivel angle ψ (i.e., angle between the vertical plane and the arm plane) is defined to designate the arm posture by specifying the elbow position, which becomes farther from the trunk in the lateral direction as the ψ increasing positively. The hand position on the constraint workspace can be obtained using a forward kinematics, $f_{ETC,h}$: $(\theta, \phi, \psi)^{\mathrm{T}} \rightarrow (x_h, y_h, z_h)^{\mathrm{T}}$:

$$f_{ETC,h} = \begin{bmatrix} x_h(\theta,\phi) \\ y_h(\theta,\phi) \\ z_h(\theta,\phi) \end{bmatrix} = \begin{bmatrix} d\cos\theta\sin\phi \\ d\cos\theta\cos\phi \\ d\sin\theta \end{bmatrix}. \tag{80}$$

Note that the elbow swivel angle ψ does not contribute to the hand position, $\mathbf{x_h}(x_h, y_h, z_h)^{\mathrm{T}}$. This fact yields a redundant mapping problem of the inverse kinematics, i_{ETC}: $(x_h, y_h, z_h)^{\mathrm{T}} \rightarrow (\theta, \phi, \psi)^{\mathrm{T}}$ since ψ is not dependent on $\mathbf{x_h}(x_h, y_h, z_h)^{\mathrm{T}}$. The latitude θ and the longitude ϕ locate the hand in the workspace, while the elbow swivel angle ψ finalizes the arm posture. In order to fully specify the ETC angles θ, ϕ and ψ, the elbow position $\mathbf{x_e}(x_e, y_e, z_e)^{\mathrm{T}}$ needs to be additionally involved to make the inverse kinematics a unique mapping, i_{ETC}: $(\mathbf{x_h}^{\mathrm{T}}, \mathbf{x_e}^{\mathrm{T}}) \rightarrow (\theta, \phi, \psi)^{\mathrm{T}}$:

$$i_{ETC}\left(\mathbf{x}_\mathbf{h}^{\mathrm{T}}, \mathbf{x}_\mathbf{e}^{\mathrm{T}}\right) = \begin{bmatrix}\theta \\ \phi \\ \psi\end{bmatrix} = \begin{bmatrix} \operatorname{asin}\left(\frac{z_h}{d}\right) \\ \operatorname{atan2}\left(x_h, y_h\right) \\ \operatorname{sign}\left\{\left(\mathbf{n}_\mathbf{ap} \times \mathbf{n}_\mathbf{v}\right) \cdot \mathbf{x}_\mathbf{h}\right\} \operatorname{acos}\left(\mathbf{n}_\mathbf{v} \cdot \mathbf{n}_\mathbf{ap}\right) \end{bmatrix}. \tag{81}$$

From the geometrical relationship, the elbow swivel angle ψ is derived as the angle between the arm plane and the vertical plane [148]. In (81), $\mathbf{n}_\mathbf{v}$ and $\mathbf{n}_\mathbf{ap}$ refer to the unit normal vectors to the vertical plane and the arm plane, respectively, that are derived as:

$$\mathbf{n}_\mathbf{v} = \frac{\mathbf{u}_\mathbf{-z} \times \mathbf{x}_\mathbf{h}}{\left\|\mathbf{u}_\mathbf{-z} \times \mathbf{x}_\mathbf{h}\right\|} \quad \text{and} \quad \mathbf{n}_\mathbf{ap} = \frac{\mathbf{x}_\mathbf{e} \times \mathbf{x}_\mathbf{h}}{\left\|\mathbf{x}_\mathbf{e} \times \mathbf{x}_\mathbf{h}\right\|}, \tag{82}$$

where $\mathbf{u}_\mathbf{-z}$ represents the unit vector for negative Z_0 direction. For given ETC angles, the full configuration of the arm in the Cartesian space can be further completed by specifying the elbow position with another forward kinematics, $f_{ETC,e}$: $(\theta, \phi, \psi)^{\mathrm{T}} \rightarrow (x_e, y_e, z_e)^{\mathrm{T}}$:

$$f_{ETC,e} = \begin{bmatrix} x_e\left(\theta,\phi,\psi\right) \\ y_e\left(\theta,\phi,\psi\right) \\ z_e\left(\theta,\phi,\psi\right) \end{bmatrix} = \begin{bmatrix} uc_\theta s_\phi + v\left(c_\phi s_\psi + s_\theta s_\phi c_\psi\right) \\ uc_\theta c_\phi - v\left(s_\phi s_\psi - s_\theta c_\phi c_\psi\right) \\ us_\theta - vc_\theta c_\psi \end{bmatrix}, \tag{83}$$

where $\sin(\cdot)$ and $\cos(\cdot)$ are denoted as $s_{(\cdot)}$ and $c_{(\cdot)}$, respectively. The parameters u and v are geometrically derived from the arm configuration that are defined as:

$$u = \frac{l_u^2 - l_f^2 + d^2}{2d} \quad \text{and} \quad v = \frac{\sqrt{4d^2 l_u^2 - \left(l_u^2 - l_f^2 + d^2\right)^2}}{2d}, \tag{84}$$

where l_u and l_f indicate link lengths of the upper arm and the forearm, respectively. The detailed derivation of (83) and (84) follows the procedure introduced in [64]. Since the shoulder position is always fixed at the origin of the global frame (see $X_0Y_0Z_0$ in Fig. 3(c)), the elbow swivel angle ψ determines the elbow position for a given hand position $\mathbf{x_h}$ as a point lying on a circle around the virtual link connecting the shoulder and the hand [149]. The circle can be obtained as the intersection between two spheres: 1) upper arm link sphere around the shoulder with radius l_u and 2) forearm link sphere around the wrist with radius l_f. From the geometry shown in Fig. 27, the elbow position $\mathbf{x_e}$ can be derived as:

$$f_{ETC,elbow}(\theta,\phi,\psi)^{\mathrm{T}} = \mathbf{R}_{\mathbf{Z}_0}(-\phi)\,\mathbf{R}_{\mathbf{X}_0}(\theta)\left[u\mathbf{e}_{\mathbf{y}} + v\mathbf{e}_{\mathbf{r}}(\psi)\right], \tag{85}$$

where $\mathbf{R_{Zo}}$ and $\mathbf{R_{Xo}}$ refer rotation matrices about Z_0 and X_0 axes of the global frame, respectively. The unit vectors $\mathbf{e_y}=(0, 1, 0)^{\mathrm{T}}$ and $\mathbf{e_r}(\psi)=(\sin\psi, 0, -\cos\psi)^{\mathrm{T}}$ assign direction of the virtual link and the direction of the elbow position around the virtual link, respectively. From the geometry of right triangles in Figure 26, the distance u of the circle from the shoulder and the radius of the circle v can be derived as (84) by solving two equations:

$$\begin{aligned} u^2 + v^2 &= l_u^2, \\ (d-u)^2 + v^2 &= l_f^2. \end{aligned} \tag{86}$$

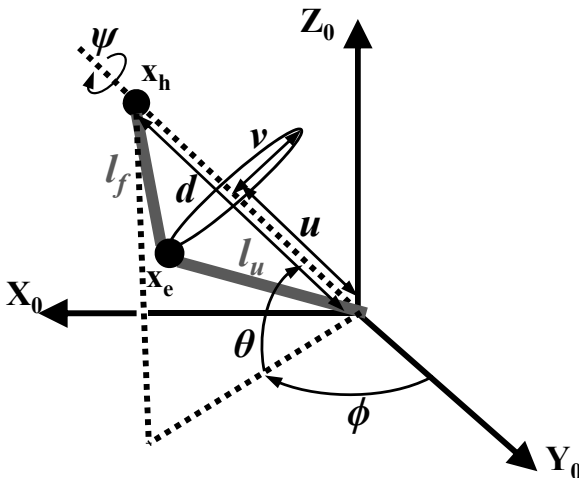

Figure 26. Elbow position x_e determination for a given hand position x_h.

From the control engineering perspective, a hand path planned in the CNS needs to be converted into a specific command signal with respect to an internal body frame to actuate the musculoskeletal system. In this sense, intrinsic joint coordinates (IJC) are defined in Figure 25(b) to represent the constraint arm motion kinematics in joint space. In the figure, two thick lines indicate the upper arm and forearm links. The IJC consist of humeral elevation α (i.e., angle between the negative Z_0 axis and the upper arm link), shoulder azimuth β (i.e., angle of the upper arm link projected on the X_0-Y_0 plane measured from the positive Y_0 axis), humeral rotation γ (angle of the upper arm link rotation about its longitudinal axis), and elbow flexion δ (angle of the forearm link measured from the extrapolation of the upper arm link). In the zero posture, the IJC angles are $\mathbf{q_0} := [\alpha, \beta, \gamma, \delta]^T = [0, 0, 0, 0]^T$, the arm is fully extended downward and the axis of elbow rotation is aligned on the medial-lateral direction of the body (see Figure 24(c) for

clarification). From the D-H parameters [150] shown in Table 11, the transformation matrix between two frames is derived by:

$$\mathbf{T}_{i-1}^{i} = \mathbf{R}_{\mathbf{Z}}(\theta_i)\mathbf{D}_{\mathbf{Z}}(d_i)\mathbf{D}_{\mathbf{X}}(a_i)\mathbf{R}_{\mathbf{X}}(\alpha_i), \tag{87}$$

where $\mathbf{R_Z}$ and $\mathbf{R_X}$ represent rotation matrices while $\mathbf{D_Z}$ and $\mathbf{D_X}$ are translation matrices, all in the extended 4-by-4 format and with respect to the current frame [151]. The hand position in the task space can be derived from the forward kinematics $f_{IJC,h}$: $(\alpha, \beta, \gamma, \delta)^{\mathrm{T}} \rightarrow (x_h, y_h, z_h)^{\mathrm{T}}$:

$$f_{IJC,h} = \begin{bmatrix} x_e \\ y_e \\ z_e \end{bmatrix} + \begin{bmatrix} l_f \left\{ \mathrm{s}_\delta \left(\mathrm{s}_\alpha \mathrm{s}_\beta \mathrm{c}_\gamma - \mathrm{c}_\beta \mathrm{s}_\gamma \right) + \mathrm{s}_\alpha \mathrm{s}_\beta \mathrm{c}_\delta \right\} \\ l_f \left\{ \mathrm{s}_\delta \left(\mathrm{s}_\alpha \mathrm{s}_\gamma + \mathrm{c}_\alpha \mathrm{c}_\beta \mathrm{c}_\gamma \right) + \mathrm{c}_\alpha \mathrm{s}_\beta \mathrm{c}_\delta \right\} \\ l_f \left(\mathrm{s}_\beta \mathrm{c}_\gamma \mathrm{s}_\delta - \mathrm{c}_\beta \mathrm{c}_\delta \right) \end{bmatrix}. \tag{88}$$

The elbow position $\mathbf{x_e}(x_e, y_e, z_e)^{\mathrm{T}}$ in (88) is obtained by another forward kinematics $f_{IJC,e}$: $(\alpha, \beta, \gamma, \delta)^{\mathrm{T}} \rightarrow (x_e, y_e, z_e)^{\mathrm{T}}$:

$$f_{IJC,e} = \begin{bmatrix} x_e \\ y_e \\ z_e \end{bmatrix} = \begin{bmatrix} l_u \sin\alpha \sin\beta \\ l_u \cos\alpha \sin\beta \\ -l_u \cos\beta \end{bmatrix}. \tag{89}$$

For clarity, refer to Figure 24(b). Note that the elbow flexion δ is a constant angle when the elbow joint is locked in place and each joint angle can be obtained using inverse kinematics, i_{IJC}: $(\mathbf{x_h}^T, \mathbf{x_e}^T) \rightarrow (\alpha, \beta, \gamma, \delta)^T$ [64] as represented in (26).

Table 11. Denavit-Hartenberg (D-H) parameters (modified from [151]).

Joint	DOF	i	α_i	a_i	d_i	θ_i
Base	0	$1_{(0\rightarrow1)}$	180º	0	0	90º
Shoulder	Azimuth	$2_{(1\rightarrow2)}$	-90º	0	0	α
Shoulder	Elevation	$3_{(2\rightarrow3)}$	-90º	0	0	β
Shoulder	Humeral rotation	$4_{(3\rightarrow4)}$	90º	0	$-l_u$	γ
Elbow	Flexion	$5_{(4\rightarrow5)}$	0	0	0	δ

3.4.3. Human arm dynamics

As described in Section 2.4.2.3, the human arm dynamics is approximated by a rigid body dynamics. Equations of motion derived in (31) to (34) are utilized except the separation of kinetic torque τ_k from the kinetic energy terms and gravitational torque τ_g from the potential energy terms. The resultant torque component equation for the i-th joint is obtained as:

$$\tau_i = \tau_{k,i} + \tau_{g,i} = \frac{d}{dt}\left(\frac{\partial (T-V)}{\partial \dot{q}_i}\right) - \frac{\partial (T-V)}{\partial q_i}, \tag{90}$$

where T and V are for the entire arm links and the generalized coordinate q_i is i-th joint DOF angle in IJC.

3.4.4. Mapping between two coordinate systems

In this paper, we consider that the concept of ETC is linked to the motor coordination in the conscious (or higher) level of the CNS. From experimental study on monkeys, Fu *et al*., [152] showed that the activations of neurons in the primary and the superior precentral premotor areas are highly correlated to the direction and distance of reaching. It supports that the positions of reaching targets and the hand are perceived in terms of the direction and the distance relative to an internal body frame within the CNS. Although it is not certain whether the hand position is controlled in the shoulder centered frame (see [101, 153, 154] for examples) in human CNS, the coordinate transformation matrix from the shoulder centered frame to an unknown true internal frame can be assumed as constant with an assumption of no considerable head movements during the reaching. Since the ETC contains the direct mapping of the hand direction on the minimum number of controllable variables (i.e., latitude θ and longitude ϕ), it is considered to be utilized in the hand path planning process shown in Figure 22(a). Also, the arm posture along the determined hand path is dominated by a single DOF (i.e., elbow swivel angle ψ) which enables the CNS to solve the second redundant mapping problem (see Figure 22(b)) without much complexity. On the other hand, the concept of IJC is more related to the motor command generation with respect to an internal body frame (e.g., muscle coordinates) in the unconscious/lower level of the CNS. In the IJC, the hand path and the arm posture are coordinated at once by specifying every joint DOF.

In order to represent the joint coordination strategy of the CNS in the hand path formulation and the arm posture selection, a mathematical mapping between two

coordinate systems is derived. Let us define a mapping, F: $(\alpha, \beta, \gamma, \delta)^{\mathrm{T}} \rightarrow (\theta, \phi, \psi)^{\mathrm{T}}$, from the IJC to the ETC:

$$F(\alpha,\beta,\gamma,\delta) = \begin{bmatrix} \theta(\alpha,\beta,\gamma,\delta) \\ \phi(\alpha,\beta,\gamma,\delta) \\ \psi(\alpha,\beta,\gamma,\delta) \end{bmatrix}. \tag{91}$$

The detailed entries of this mapping can be obtained by substituting the forward kinematics $f_{IJC,h}$ and $f_{IJC,e}$ (see (88) and (89)) into the inverse kinematics i_{ETC} represented in (81). Each row of the mapping F represents the latitude (or vertical) and the longitude (or horizontal) portions of the hand path geometry and the arm posture in terms of IJC angles. The instantaneous contribution of each IJC angular motion on each row of (91) can be quantified as follows:

1) the sensitivity of the mapping F is computed by the Jacobian

$$J(F) = \begin{bmatrix} \frac{\partial F}{\partial \alpha} & \frac{\partial F}{\partial \beta} & \frac{\partial F}{\partial \gamma} & \frac{\partial F}{\partial \delta} \end{bmatrix}, \tag{92}$$

2) the kinematic contribution amounts are determined as proportions of effective IJC angular velocities within ETC angular velocities

$$\boldsymbol{\Omega}_{\boldsymbol{\Theta}} = J(F)\boldsymbol{\Omega}_{\mathbf{A}}, \tag{93}$$

where $\mathbf{\Omega_\Theta}=[\omega_\theta,\ \omega_\phi,\ \omega_\psi]^T$, $\mathbf{\Omega_A}=[\omega_\alpha,\ \omega_\beta,\ \omega_\gamma,\ \omega_\delta]^T$ and ω indicates the angular velocity vectors in the ETC and the IJC, respectively. Each row of the computed (93) contains the IJC DOF contributions on the performed arm reaching motion (i.e., 1st and 2nd rows for the latitude and the longitude portions of the hand path geometry, and 3rd row for the arm posture configuration).

In a similar manner, the dynamic contribution of each IJC DOF joint torque on generated ETC torques can be derived. According to the operational space control concept [155], force vectors on the hand ($\mathbf{F_{HND}}$) and the elbow ($\mathbf{F_{ELB}}$) in the Cartesian space can be calculated as:

$$\mathbf{F_X} = J^{-\mathrm{T}}\left(\begin{bmatrix} f_{IJC,h} \\ f_{IJC,e} \end{bmatrix}\right)\boldsymbol{\tau}_\mathrm{A}, \tag{94}$$

where $\mathbf{F_X}=[\mathbf{F}^T_{\mathbf{HND}},\ \mathbf{F}^T_{\mathbf{ELB}}]^T$ and $\boldsymbol{\tau_A}=[\tau_\alpha,\ \tau_\beta,\ \tau_\gamma,\ \tau_\delta]^T$ represent the end-effector force in the Cartesian coordinates and the joint torque vector in the IJC, respectively. The symbol $J(.)$ refers to the Jacobian matrix and detailed entries of the forward kinematics $f_{IJC,h}$ and $f_{IJC,e}$ are derived in (88) and (89). Since the Jacobian in (92) is not a square matrix, its inverse transpose is computed as the Moore-Penrose pseudo inverse of the Jacobian transpose. Then the force vector $\mathbf{F_X}$ can be converted into an ETC angular torque vector $\boldsymbol{\tau_\Theta}=[\tau_\theta,\ \tau_\phi,\ \tau_\psi]^T$ by the same concept:

$$\boldsymbol{\tau}_\mathbf{\Theta} = J^{\mathrm{T}}\left(\begin{bmatrix} f_{ETC,h} \\ f_{ETC,e} \end{bmatrix}\right)\mathbf{F_X}, \tag{95}$$

where the forward kinematics $f_{ETC,h}$ and $f_{ETC,e}$ are defined in (80) and (83). By substituting (94) into (95), the ETC angular torque vector can be represented in terms of the IJC angular torque vector as:

$$\boldsymbol{\tau}_{\boldsymbol{\Theta}} = J^{\mathrm{T}}\left(\begin{bmatrix} f_{ETC,h} \\ f_{ETC,e} \end{bmatrix}\right) J^{-\mathrm{T}}\left(\begin{bmatrix} f_{IJC,h} \\ f_{IJC,e} \end{bmatrix}\right)\boldsymbol{\tau}_{\mathrm{A}} \tag{96}$$

Each row of equation (96) contains the amount of contribution of each IJC DOF torque on the corresponding ETC torque value. Here, $\boldsymbol{\tau}_{\mathbf{A}}$ can be separated into $\boldsymbol{\tau}_{\mathbf{A,k}}$ and $\boldsymbol{\tau}_{\mathbf{A,g}}$ by selecting the kinetic torque $\tau_{k,i}$ or the gravitational torque $\tau_{k,i}$ in (90) and their corresponding results of $\boldsymbol{\tau}_{\boldsymbol{\Theta}}$ in (96) are defined as $\boldsymbol{\tau}_{\boldsymbol{\Theta},\mathbf{k}}$ and $\boldsymbol{\tau}_{\boldsymbol{\Theta},\mathbf{g}}$, respectively.

3.5. Experimental Setup and Procedure

In order to observe governing rules of the human CNS on two main redundancy resolutions in point-to-point reaching actions (i.e., the hand path formulation and the arm posture selection), a reaching experiment is designed. During the experiment, the wrist motion was minimized by a stabilizing brace (AirCast A2 Wrist Brace, DJO Global Inc., USA) and the subject's trunk motion was restrained on a high-back chair with elastic bands to restrict the movement of the shoulder joint (i.e., center of the constraint workspace) in the space. Four target points were displayed on a computer monitor and twelve reaching directions were defined among those targets (see Figure 27(a)): 1) top horizontal left to right (THLR), 2) top horizontal right to left (THRL), 3) bottom horizontal

left to right (BHLR), 4) bottom horizontal right to left (BHRL), 5) left vertical up to down (LVUD), 6) left vertical down to up (LVDU), 7) right vertical up to down (RVUD), 8) right vertical down to up (RVDU), 9) left diagonal up to down (LDUD), 10) left diagonal down to up (LDDU), 11) right diagonal up to down (RDUD) and 12) right diagonal down to up (RDDU). The distance of the monitor was set in accordance to the subject's arm reachable workspace prior to experimental trials. The experiment was approved by the institutional review board at the Texas A&M University, College Station, Texas (TAMU IRB #2014-0230). Five volunteers (4 males and 1 female) participated the experiment to perform series of point-to-point reaching actions with and without the elbow constraint. To realize the kinematic constraint condition with minimal effects on the arm dynamics, a light weight elbow brace was adopted (Aircast Mayo Clinic Elbow Brace, DJO Global Inc., USA). The elbow joint angle was fixed at δ=60º. To induce the most natural motions, all subjects were asked to perform ten reaching trials for each defined direction in their self-selected speeds.

During the experiments the motion kinematics and the dynamics were captured by the developed mobile MCS prototype (see Section 2). Three Shimmer IMU sensors were attached on the subject's trunk, upper arm and forearm regions to capture the motion kinematics and four Shimmer EMG sensors were attached on the subject's anterior and posterior deltoids, biceps brachii and triceps brachii muscles to acquire muscle activations (see Figure 27(b) for the sensor attachment). IMU sensors and EMG sensors acquire motion data in 256 Hz and 512 Hz, respectively. The global frame was defined as the thorax frame shown in Figure 14(a).

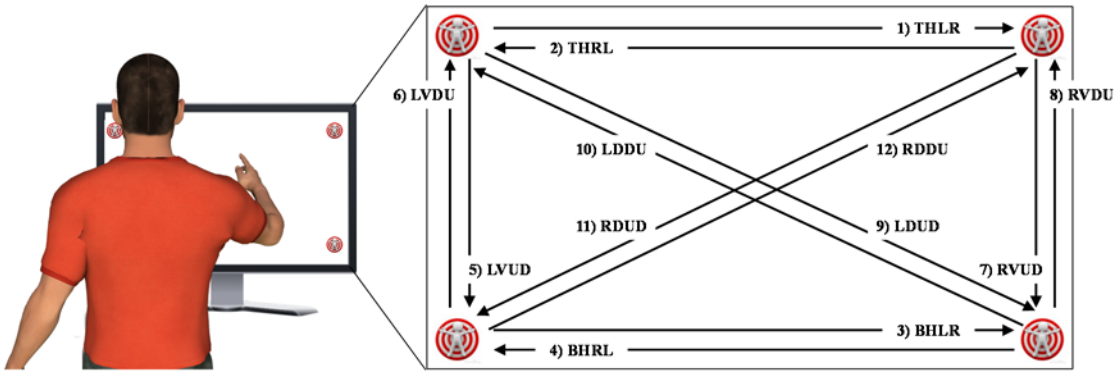

(a) Front view of the target display and reaching directions defined among four targets.

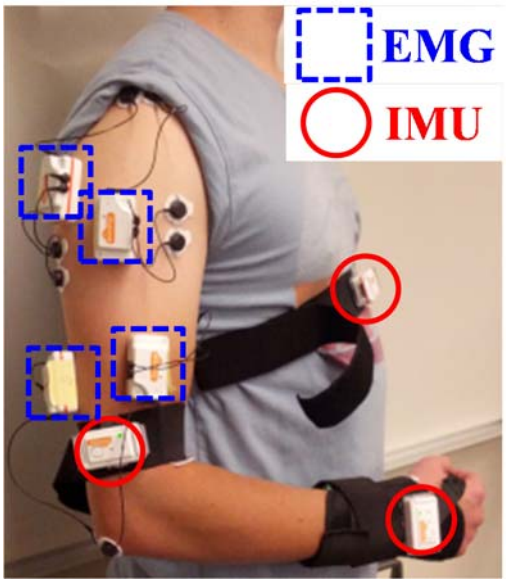

(b) Sensor attachment.

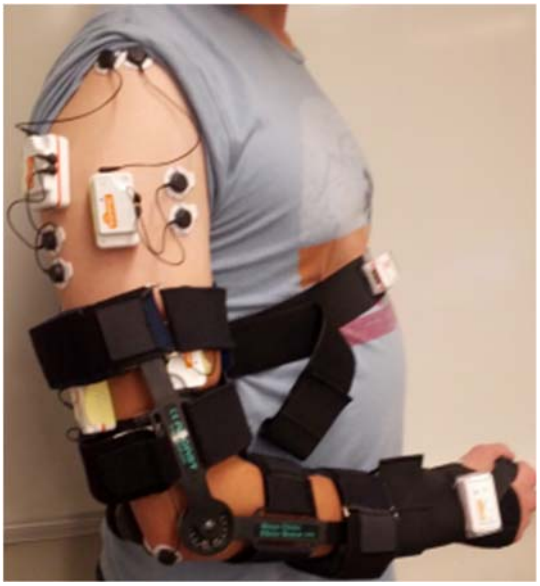

(c) Elbow brace attachment.

Figure 27. Experimental setup for point-to-point reaching motions.

3.6. Experimental Observations

3.6.1. Constraint workspace validation

Theoretically, the imposed elbow joint constraint condition restrains arm reachable workspace on a spherical surface and enables the CNS to map desired hand paths in Cartesian space to corresponding ETC angles (i.e., latitude θ and longitude ϕ) by ruling out the distance control of the hand position. In order to validate the constraint workspace

geometry, the distance between shoulder and wrist markers (see d in Figure 24(b) and Figure 25(a)) is computed for each trial either from hand marker position $\mathbf{x_h}(x_h, y_h, z_h)^T$ or from the law of cosine:

$$d = \sqrt{x_h^2 + y_h^2 + z_h^2} = \sqrt{l_u^2 + l_f^2 - 2l_u l_f \cos(\pi - \delta)}. \quad (97)$$

To observe the consistency of the elbow locked condition during the constrained reaching motions, the standard deviation σ_d for each subject is plotted in Figure 28(a) as a percentage over $\bar{d}$, which is the mean of d values within the trial. The abscissa of the distribution plot represents reaching directions categorized in three groups (H-horizontal, V-vertical, and D-diagonal) for each subject. In the figure, left (grey-colored) and right (black colored) distributions represent the non-constraint (NC) and the constraint elbow (EC) conditions, respectively. For the NC case, the extreme σ_d does not exceed 5% of the mean distance $\bar{d}$ and most of the data reside within 2%. The standard deviation σ_δ of the elbow flexion angle δ computed from (26) is represented in Figure 28(b). Most of the δ variance during the constrained elbow reaching was limited to 5°. In the figures, geometrical features of the spherical workspace (i.e., consistencies of d and δ, which represent a constant radius of the sphere) do not vary significantly for all subjects regardless of the reaching direction. It is considered that the small variations of features are due to 1) backlash in joint locking mechanism of the elbow brace and 2) measurement errors of the utilized mobile MCS. However, it is noteworthy that the EC case shows

consistently lower variances than the NC case for all subjects regardless of reaching directions.

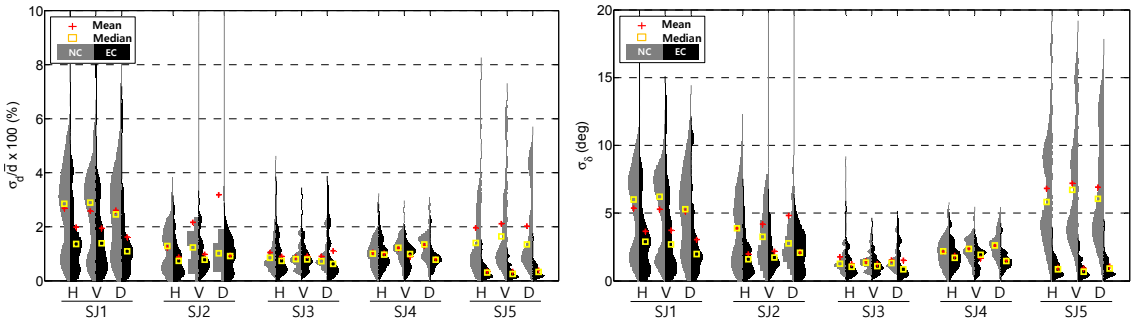

(a) Standard deviation over mean of *d* in percentage. **(b) Standard deviation of elbow flexion angle *δ*.**

Figure 28. Distribution plots of constraint workspace validation.

3.6.2. Observations on the hand path geometry formulation

It is assumed that the governing rules emphasize the efficiency of motion to resolve the redundancy problems. Since the CNS focuses on hand kinematics during reaching motions, it is hypothesized that the hand path geometry is determined to cost the least kinematic efforts (LKE). Two candidate models are considered in the ETC: the geodesic curve and the rhumb line (*loxodrome*). The Euclidean geodesic curve is the shortest path connecting two points in the workspace. It is well known that the geodesic for connecting any two points in space becomes a straight line as observed by previous studies (see Section 3.3). For the EC case, we need to define a geodesic curve that is constrained on the surface of the spherical workspace. In order to define an invariant metric of the curve, the first fundamental form is defined as:

$$\mathbf{I} = \left[J\left(f_{ETC,h} \right) \right]^T \left[J\left(f_{ETC,h} \right) \right] = d^2 \begin{bmatrix} 1 & 0 \\ 0 & \cos^2 \theta \end{bmatrix}, \tag{98}$$

where the Jacobian of the ETC's forward kinematics $f_{ETC,h}$ is:

$$\begin{aligned} J\left(f_{ETC,h} \right) &= \begin{bmatrix} \dfrac{\partial f_{ETC,h}}{\partial \theta} & \dfrac{\partial f_{ETC,h}}{\partial \phi} \end{bmatrix} \\ &= d \begin{bmatrix} -\sin\theta \sin\phi & \cos\theta \cos\phi \\ -\sin\theta \cos\phi & -\cos\theta \sin\phi \\ \cos\theta & 0 \end{bmatrix}. \end{aligned} \tag{99}$$

Note that the 3rd column of $J(f_{ETC,h})$ in (99), which contains the derivatives with respect to ψ, is ignored since it is a zero vector. Due to the fact that the columns of the $J(f_{ETC,h})$ form a basis of the tangent space (i.e., full rank), the inverse of (98) exists and we can derive the Christoffel Symbols of the second kind as:

$$\Gamma_{ij}^k = \left[\mathbf{I} \right]^{-1} \left[J\left(f_{ETC,h} \right) \right]^T \left(\frac{\partial^2 f_{ETC,h}}{\partial u_i \partial u_j} \right), \tag{100}$$

where $u=(\theta, \phi)^T$ is a redefined ETC, which excludes the elbow swivel angle ψ. Note that ψ does not contribute to the hand path formulation as shown in (80). The curve becomes a geodesic if the redefined coordinates u satisfy the differential equation:

$$\ddot{u} + \dot{u}^T \left[\Gamma_{ij}^k \right] \dot{u} = 0, \tag{101}$$

which is equivalent to the set of equations

$$\begin{aligned} \ddot{\theta} + \dot{\phi}^2 \sin\theta \cos\theta = 0, \\ \ddot{\phi} - 2\dot{\theta}\dot{\phi} \tan\theta = 0. \end{aligned} \tag{102}$$

By substituting the integral of (102) into the forward kinematics $f_{ETC,h}$ with two boundary conditions, the geodesic curve is computed in the Cartesian coordinates. This two point boundary value problem can be solved numerically by using a shooting method (e.g., bvp4c.m in MATLAB) [156]. However, it is also well known that the geodesic curve becomes identical to a great circle connecting the two points on its spherical surface for the EC case.

Though the geodesic curve represents the LKE in terms of its arc length (i.e., hand travel distance), it requires comprehensive understanding on the geometry of the constraint workspace. On the other hand, the rhumb line, which is described as the smoothest path in [93], can be derived in more intuitive manner. Let us represent the initial and the final hand positions in the redefined ETC as $u_i=(\theta_i, \phi_i, d_i)^{\mathrm{T}}$ and $u_f=(\theta_f, \phi_f, d_f)^{\mathrm{T}}$, respectively. The rhumb line becomes a straight line between two task points in the redefined coordinates u and it can be parameterized by changes of longitude $\Delta\phi$, latitude $\Delta\theta$ or distance Δd with a constant slope m as:

$$\begin{bmatrix} \theta \\ \phi \\ d \end{bmatrix} = \begin{bmatrix} \theta_i + m\Delta\phi \\ \phi_i + \Delta\phi \\ d_i + \Delta d \end{bmatrix} = \begin{bmatrix} \theta_i + \Delta\theta \\ \phi_i + \frac{1}{m}\Delta\theta \\ d_i + \Delta d \end{bmatrix} \text{ where } m = \frac{\theta_f - \theta_i}{\phi_f - \phi_i}. \quad (103)$$

Note that the rhumb line costs the LKE in terms of latitude and longitude angles in the ETC, and the distance d. Since θ, ϕ and d are intuitively matched with horizontal and vertical directions, and the distance of a reaching task, the CNS can perform the task without knowing the geometry of the reachable workspace. In the EC case, d becomes a constant as the distance control mobility is locked by the elbow constraint.

Since the hand paths are not exactly constrained on the spherical workspace for the EC case due to the varying distance d and elbow fixed angle δ (see Figure 28), their task points (i.e., initial and final hand positions) are not matching with the corresponding points of the two models. Note that the model outputs are derived in the ETC angles and their paths in the Cartesian coordinates are obtained by the forward kinematics $f_{ETC,h}$ which adopts a constant distance d (see equation (80)). In order to resolve this problem, hand paths are converted into the ETC angles by the inverse kinematics i_E (see equation (81)) then reformulated via $f_{ETC,h}$ with mean distance $\bar{d}$ for the trial. Selected experimental results of a subject with 60º elbow locked condition are compared to corresponding geodesic curves and rhumb lines in Figure 29. In the figure, THLR, LVUD, and LDUD are selected reaching directions and the black diamond indicates the shoulder marker position. The approximated spherical workspace is plotted as a shaded surface. There are barely deviations between two model outputs (i.e., geodesic curves and rhumb lines) and

the experimental data closely follow them for the EC case (see Figure 29(b)). For the NC case (see Figure 29(a)), however, experimental paths show larger deviations from two model outputs. Also, the rhumb lines are computed almost identical as the EC case while geodesic lines show different geometries from the EC case. It is due to different centric coordinate systems that each model utilizes: i.e., geodesics are computed as a straight line in Cartesian space, and rhumb lines are computed in ETC. From this, we can infer that the CNS prefers spherical coordinates rather than Cartesian coordinates for its motor coordination.

For a quantitative analysis, the hand path length index (HPLI) is defined to compare the arc lengths as:

$$\mathrm{HPLI} = \frac{S_{EXP} - S_M}{S_{EXP}} \times 100(\%), \tag{104}$$

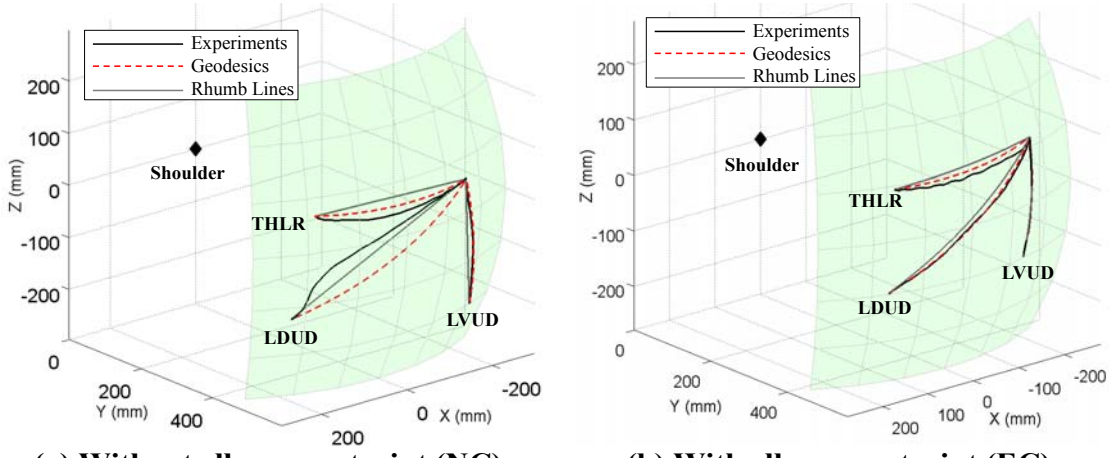

(a) Without elbow constraint (NC). **(b) With elbow constraint (EC).**

Figure 29. 3D Hand path geometry comparison on selected trials.

where S indicates the arc length and the subscripts $_{EXP}$ and $_{M}$ stand for an experimental data and a model output, respectively. Distributions of computed HPLI values across all trials for each subject are represented in Figure 30 as violin plots. The $HPLI_{GC}$ and $HPLI_{RL}$ refer to HPLI computed on geodesic curves and rhumb lines, respectively. For the NC case (see Figure 30(a)), rhumb lines show close approximation than geodesic lines in terms of their arc lengths. Notice that the range of $HPLI_{RL}$ spans to negative which means that some of hand paths are shorter than their corresponding rhumb lines. On the other hand, probability densities of geodesic curves and rhumb lines show no significant differences in terms of their arc lengths in the EC case (see Figure 30(b)). As the hand path is constrained on the spherical surface and losing its one DOF (i.e., distance control), both hand paths and model outputs get closer geometries each other. Positive HPLI values in Figure 30(b) imply that the actual hand paths are always longer than corresponding geodesic curves and rhumb lines when the elbow is constrained.

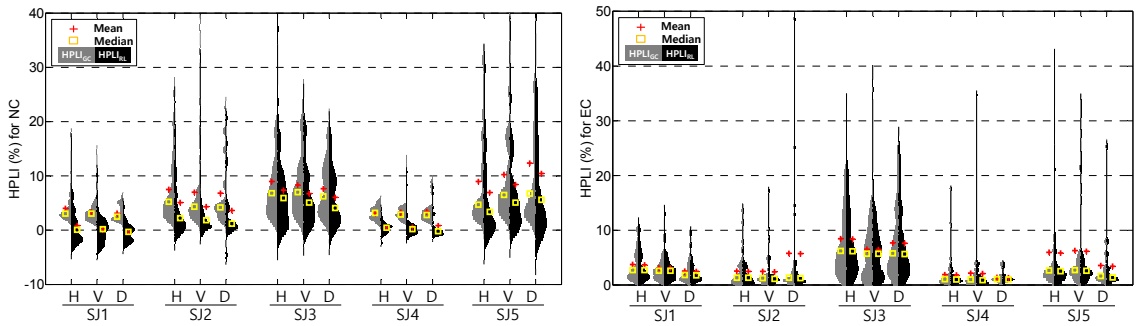

(a) Without elbow constraint (NC). **(b) With elbow constraint (EC).**

Figure 30. Computed HPLI values across all trials of each subject.

It also means that the actual hand path is more curved than corresponding two model outputs. From the inter-subject differences of HPLI values shown in Figure 30, we can infer that some subjects generally drew more curved and wavy hand paths than the others. Such curviness and waviness of hand paths can be measured by lateral motion amount compared to the tangential portion of movement. For the EC case, the measure can be specified as the lateral motion in the bionormal direction of the Frenet-Serret frame. Since the geodesic curve (i.e., the straightest path on the constraint workspace) have no such lateral component by its definition, the curviness and the waviness of the experimental hand path geometry can be measured by comparing the direction of its tangential vectors with corresponding geodesic tangential vectors. In this sense, an angle between the tangential vectors of the experimental path and the geodesic is computed at every intermediate point as:

$$\vartheta = \text{sign}\left(\mathbf{x_h} \bullet \left(\mathbf{t_{EXP}} \times \mathbf{t_{GEO}}\right)\right) \cos^{-1}\left(\mathbf{t_{EXP}} \bullet \mathbf{t_{GEO}}\right) \tag{105}$$

where $\mathbf{t_{EXP}}$ and $\mathbf{t_{GEO}}$ refer to the unit tangential vectors of the experimental hand path and the geodesic curve, respectively, at each intermediate point. Note that all intermediate points are equally spaced along the path's arc length to exclude any temporal information. Since $\mathbf{t_{GEO}}$ is always pointing the straightest direction, the angle ϑ indicates the amount of lateral offset along the hand path propagation. Figure 31 shows an example plot of selected THLR trials of the SJ1. In the figure, left and right graphs are respective results of NC and EC cases. In Figure 31(a), captured hand paths and corresponding geodesic curves are

plotted with their tangential vectors at some intermediate points. Notice that tangential vectors of the geodesic are exactly lying along the curve direction without any lateral component. In contrast, the actual hand path consists of multiple curvy and wavy segments induced by various lateral motions indicated by the directions of its tangential vectors. It is confirmed from the computed angle ϑ over the normalized arc length shown in Figure 31(b) that the angle ϑ fluctuates in accordance to the wavy path geometry regardless of the elbow constraint condition. Since the sign of ϑ is determined as the relative direction of the $\mathbf{t_{EXP}}$ compare to $\mathbf{t_{GEO}}$ in (105), 3D wavy geometry of hand paths can be projected on 2D graphs as represented in Figure 31(b).

Based on this relation, the lateral fluctuations of the hand path geometry can be quantified as the number of zero crossing points of the angle ϑ along the hand path. The violin plot of the number of zero crossing points of the angle ϑ, ZC(ϑ), is presented in Figure 32. From the distribution of the ZC(ϑ) for the EC case that is similar to the distribution of the HPLI shown in Figure 30(b) (except for SJ3: high HPLI value for the SJ3 is due to relatively small motion, i.e., the denominator S_{EXP} in (104) is small), it is supported that some subjects (SJ1 and SJ5) generate relatively longer paths compare to the others due to laterally more fluctuating path geometry. The reasons of such wavy motion will be discussed in the next subsection based on the intrinsic relationship between the temporal control and the hand path geometry. For the NC case, such relation is not obvious in distributions of the $HPLI_{GC}$ and the ZC(ϑ) since radial motion (i.e., distance control DOF) can also have such effects and make some complications for the interpretation.

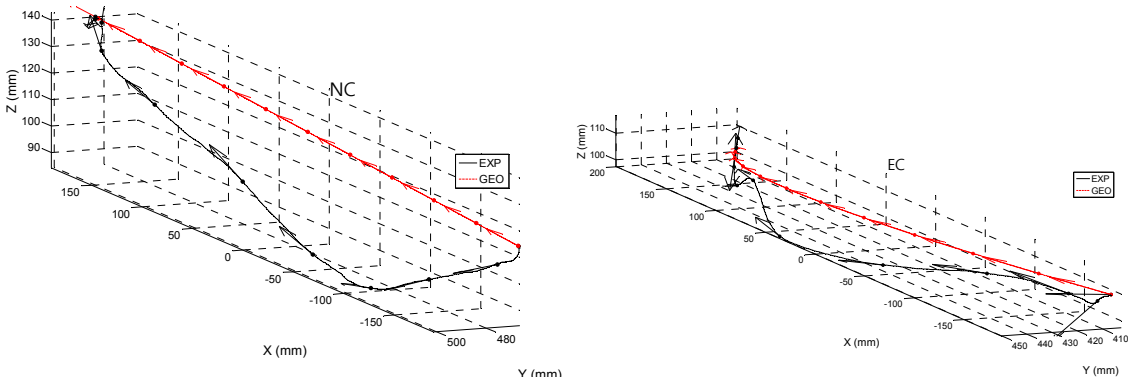

(a) 3D plot of the hand path and the geodesic curve with tangential vectors at some intermediate points.

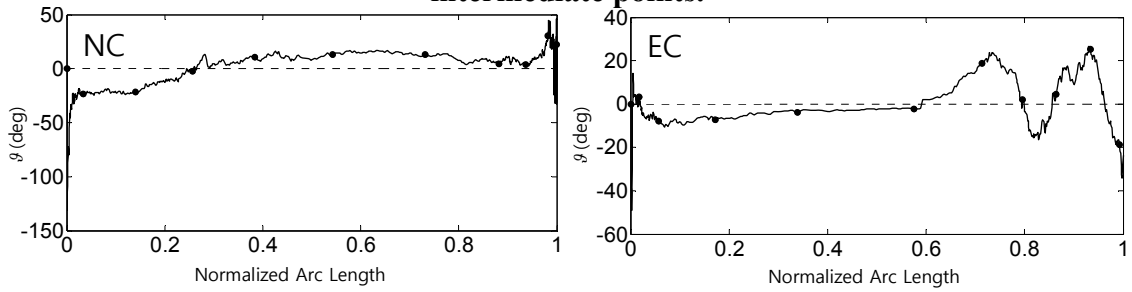

(b) Computed ϑ angle defined in (105) (Markers indicate the same intermediate points as marked in (a)).

Figure 31. The lateral motion amount of the experimental hand path compared to the corresponding geodesic curve in a selected THLR motion of the SJ1.

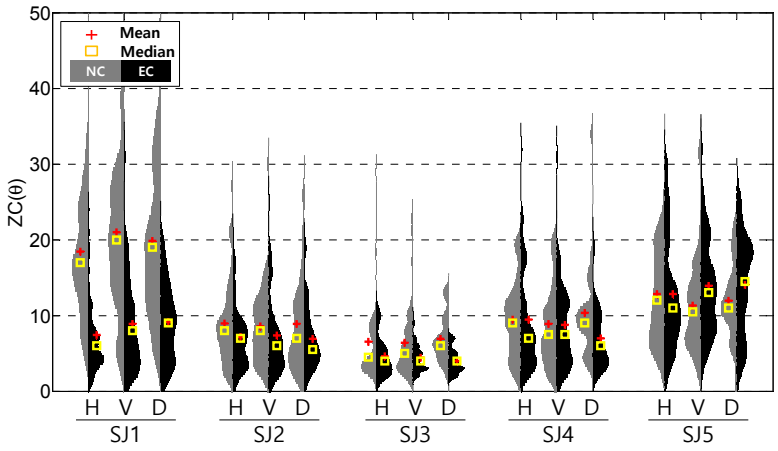

Figure 32. Violin plot of the number of zero crossing (ZC) of the angle ϑ defined in (105) across all trials of each subject.

We use Pearson's correlation coefficient (PCC) to measure the dependence between two data samples. In order to quantify the geometrical similarity between two different 3D curves (i.e., model output and experimental data), PCC for x, y, and z positions of the curves are computed and averaged as [93]:

$$\mathrm{PCC} = \frac{1}{3}\sum_{i=x,y,z} \frac{\sum_{j=1}^{N}\left(X_{ij}-\bar{X}_i\right)\left(M_{ij}-\bar{M}_i\right)}{\sqrt{\sum_{j=1}^{N}\left(X_{ij}-\bar{X}_i\right)^2\sum_{j=1}^{N}\left(M_{ij}-\bar{M}_i\right)^2}}, \tag{106}$$

where N is the number of data point within the curve. The X_{ij} and M_{ij} indicate position value of observed data and model output while $\bar{X}_i$ and $\bar{M}_i$ represent mean values. The subscript $_j$ indicates index of j-th data point and $_i$ specifies x, y, z position components. To exclude any temporal information within the path, the same equally spaced intermediate points used for the ϑ calculation in (105) are used. The closer to 1 PCC value implies that the two curves are geometrically similar. The PCC values are computed across all trials of each subject and represented in Figure 33 as violin plots. The abbreviations $\mathrm{PCC_{GC}}$ and $\mathrm{PCC_{RL}}$ refer to the PCC of geodesic curves and rhumb lines compared to corresponding actual hand paths, respectively. As shown in the Figure 33(b), geodesic curves and rhumb lines show no significant difference for the EC case in terms of geometrical similarity with the experimental data regardless of reaching directions. Note that since the PCC values depend on the curve geometry with respect to the given coordinate system, they cannot be compared between different reaching directions. In other words, higher PCC values for

diagonal motions than other reaching directions do not necessarily mean closer geometrical similarity between the experimental data and the two model outputs. For the NC case (see Figure 33(a)), PCC_{RL} is consistently higher than PCC_{GC} except for few cases (e.g., D of SJ3, and H and V of SJ5). This partially supports the observation on the HPLI (see Figure 30(a)) that the CNS prefers ETC rather than Cartesian coordinates to generate reaching motions.

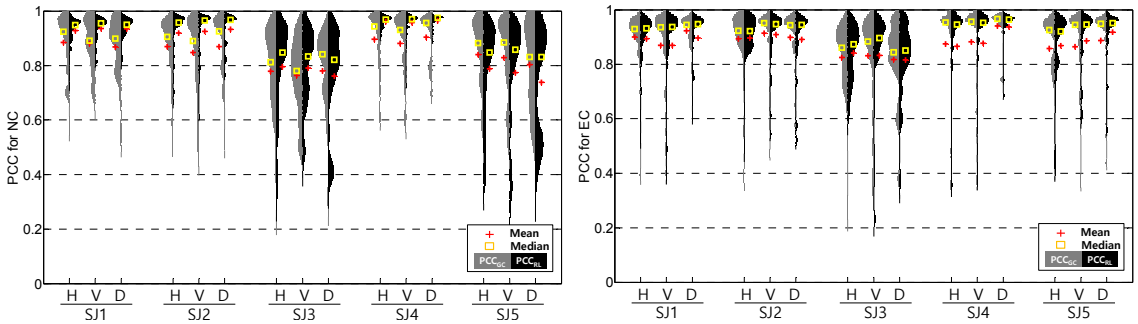

(a) Without elbow constraint (NC). **(b) 60° elbow constraint (EC).**

Figure 33. Computed PCC values across all trials of each subject.

From observations, geodesic curves and rhumb lines show no significant differences with experimental data in terms of the geometrical similarity and the arc length for the EC case. In the NC case, however, rhumb lines show better approximation to experimental hand paths than geodesics. This finding is against previous kinematic models of 2D reaching motions that approximate the hand path as a straight line connecting two task points [98, 127]. From this, we can infer that the CNS prefers spherical coordinates than Cartesian coordinates to generate hand path geometries in reaching motions on the frontal plane. It can be further considered that though the CNS focuses on the hand

kinematics in its motion planning process, there are other factors that the CNS takes into account for the motion planning. In addition, such motion planning is processed in an intrinsic coordinate that has direct mapping with the Cartesian interpretation (e.g., for the ETC, the position of hand can be defined by its latitude, longitude angles and distance with respect to a center point within the body).

In this dissertation, it is originally hypothesized that the hand path is formulated to cost LKE (least kinematic effort). Euclidean geodesic curves and rhumb lines are the shortest and the straightest paths in the Cartesian coordinates and in the ETC, respectively. Mostly, actual hand paths closely follow proposed LKE models regardless of reaching directions. From detailed quantitative observations, however, it was found that actual hand paths are more curved and wavier than corresponding LKE models especially for some subjects. This can explain that the hand path planning process (see Figure 22(a)) is not solely governed by kinematic aspects of the motion. It is pondered that the CNS also incorporates other motion aspects (e.g., dynamics) into the governing strategies of motion planning process. From following observations on the temporal control, it is partially supported by the correlation between the movement speed and the hand path geometry.

3.6.3. Observations on the temporal control strategy

The intrinsic relationship between the hand path geometry and the speed profile is studied. The planned hand path needs to be segmented into small pieces as to form a real-time reference trajectory by a governing rule in the CNS. Such temporal strategy has been approximated by modeling characteristics of natural hand speed profiles in empirical studies. Flash and Hogan [127] focused on the gracefulness of human motion and

developed the minimum jerk (MJ) model that minimizes the sum of squared hand jerks (i.e., the third time derivative of the hand position) over time in the Cartesian coordinates. The MJ model output reproduces a smooth hand speed profile in a uni-modal symmetric bell-shape [127]. Despite its good approximation of the actual speed profile, the original MJ model has a limitation in its geometrical aspect that it solely generates a straight line hand path for discrete actions (i.e., when velocities and accelerations at two task points are zeros).

Recently, Biess *et al*. [64] modified the MJ (m-MJ) model for manipulating only the time course of the hand path while its geometrical shape is preserved. Its cost function adopts the third time derivative of the arc length:

$$C_{MJ} = \int_0^T \left(\frac{d^3 s(t)}{dt^3} \right)^2 dt, \tag{107}$$

where $s(t)$ is the arc length along the experimental hand path at time t, and T refers to the total movement time. This optimization problem can be analytically solved for two point boundary conditions (i.e., $s(0)=0$ and $s(T)=S$ where S refers to the total arc length; all first and second time derivatives of $s(t)$ at both points are set as zeros) as introduced in [127]:

$$s(t) = S t_n^3 \left(10 - 15 t_n + 6 t_n^2 \right), \tag{108}$$

where $t_n = t/T$ is a normalized time frame. The optimal speed profile of the m-MJ model can be obtained by differentiating (108) over time t as:

$$v(t) = 30 v_{avg} \left[t_n \left(1 - t_n \right) \right]^2 , \tag{109}$$

where the average speed $v_{avg} = S/T$ [64]. This optimal speed profile has always the identical uni-modal bell-shape as the original MJ model regardless of the path geometry. In other words, the m-MJ model assumes the CNS' independent control on the movement speed and the hand path geometry.

In contrast to the m-MJ model, Todorov and Jordan [157] introduced the constrained MJ (c-MJ) concept that models the intrinsic relationship between the path geometry and the movement speed. The c-MJ model derives the maximally smooth speed profile along the predefined path by re-parameterizing the cost function in terms of the arc length as:

$$C_{c-MJ} = \int_0^T \left\| \frac{d^3}{dt^3} \mathbf{x_h} \left[s(t) \right] \right\|^2 dt, \tag{110}$$

where $s(t)$ is the arc length along the experimental hand position $\mathbf{x_h}$ at time t. According to the differential geometry transformation shown in [157], (110) can be represented with the curvature $\kappa(s)$ and the torsion $\tau(s)$ of the curve as:

$$C_{c-MJ} = \int_0^T \left\| \mathbf{n}\left(\kappa' \dot{s}^3 + 3\kappa \dot{s} \ddot{s}\right) + \mathbf{t}\left(\dddot{s} - \kappa^2 \dot{s}^3\right) + \mathbf{b}\left(\dot{s}^3 \kappa \tau\right) \right\|^2 dt, \tag{111}$$

where prime and dot denote derivatives with respect to the arc length s and the time parameter t, respectively. In the equation, **t**, **n** and **b** refer to the unit tangent, the unit normal and the unit binormal vectors in the Frenet-Serret frame defined on the hand path. Note that the m-MJ model counts only a part of the tangential component of the hand jerk compare to the c-MJ model. For generating the solution of the c-MJ model, a MATLAB function developed by Todorov (min_jerk.m available at [158]) is utilized.

Another regularity of the hand speed profile has been confirmed from the Isogony principle in writing and drawing tasks: hand trajectory proceeds equal angles in equal times [123]. Lacquaniti *et al*. [124] proposed the two-third power law (2/3-PL) that represents the instantaneous hand velocity as a power function of path curvature in 2D motions. For its relatively simple formula and almost universal description of actual speed profiles for arbitrary hand paths, multiple studies adopted the 2/3-PL or its modified versions to represent the experimental data. However, due to its limited performance especially on 1) inflection points or straight segments of the path and 2) the two end points of discrete movements, Todorov and Jordan [157] concluded that the c-MJ model fits better than the modified version of the 2/3-PL. Also, in their observations on the constrained hand movements, Liebermann *et al*. [93] found that the MJ model shows better approximation than the 2/3-PL.

As extended versions of the 2/3-PL, Pollick *et al*. [159] proposed the curvature-torsion power laws ($\kappa\tau$-PL) that link both curvature and torsion of the path to the

instantaneous hand velocity in 3D drawing motions. Two types of $\kappa\tau$-PL are adopted in this study to approximate the temporal governing rule in the CNS. The constrained curvature-torsion power law (c- $\kappa\tau$-PL) imposes a constraint between the curvature κ_{EXP} and the torsion τ_{EXP} to obtain the hand speed v of 3D movement as:

$$v = \lambda_{c-PL}\left(\kappa_{EXP}\sqrt{|\tau_{EXP}|}\right)^{\mu}. \tag{112}$$

In order to find the optimal speed gain $\lambda_{c\text{-}PL}$ and exponent μ, a polynomial fitting (polyfit.m in MATLAB) was applied on equation (112) after taking the log on both sides. Then, the optimal parameters were searched by a nonlinear least square curve fitting (lsqcurvefit.m in MATLAB) from initial values computed in the previous polynomial fitting. The curvature κ_{EXP} and the torsion τ_{EXP} in (112) with respect to the time parameter t are derived as [160]:

$$\kappa_{EXP} = \frac{\left|\dot{p}(t)\times\ddot{p}(t)\right|}{\left|\dot{p}(t)\right|^3}, \tag{113}$$

$$\tau_{EXP} = \frac{\left(\dot{p}(t)\times\ddot{p}(t)\right)\cdot\dddot{p}(t)}{\left|\dot{p}(t)\times\ddot{p}(t)\right|^2}, \tag{114}$$

where $p(t)=[x(t), y(t), z(t)]$ is the position vector of the curve in the Cartesian coordinates at time t. Dots refer to derivatives over time. If those time derivatives are derived by

numerical differentiations, noises in the measured position data can be significantly magnified and contaminate the resultant computations in (113) and (114). Therefore, the captured position data $p(t)$ was curve fitted by smoothing splines and analytically differentiated over the time parameter t. Also, for handling the torsion cusps, the minimum magnitude of the torsion was constrained by a threshold as stated in [159], which was set as 0.05 mm^{-1} after numbers of trial and error.

The unconstrained curvature-torsion power law (uc-$\kappa\tau$-PL) unchains the constraint relationship between the curvature and the torsion to find the best fit:

$$v = \lambda_{uc-PL}\left(\kappa_{EXP}{}^{\eta}\tau_{EXP}{}^{\rho}\right). \tag{115}$$

Here, the initial speed gain $\lambda_{uc\text{-}PL}$ and exponents η and μ were obtained from the multiple linear regression (regress.m in MATLAB), and then the optimal parameter values were searched by the same method as for the c-$\kappa\tau$-PL.

The experimental hand speed profiles are compared to the model outputs. In order to compare the speed profiles in a unified metric, the normalized time frame t_n is utilized and the magnitude of speed is scaled over an average speed $v_{avg} = S/T$, as described in [64]. The normalized hand speed profiles of each subject are compared in Figure 34 for a selected trials of THLR reaching with and without 60° of elbow constraint. In the figure, the abscissa and the ordinate represent the normalized time frame t_n and the scaled speed $|v|/v_{avg}$, respectively. For each subject, the model outputs (m-MJ, c-MJ, c-$\kappa\tau$-PL and uc-$\kappa\tau$-PL) are compared with the experimental data (EXP). Remember that there was no

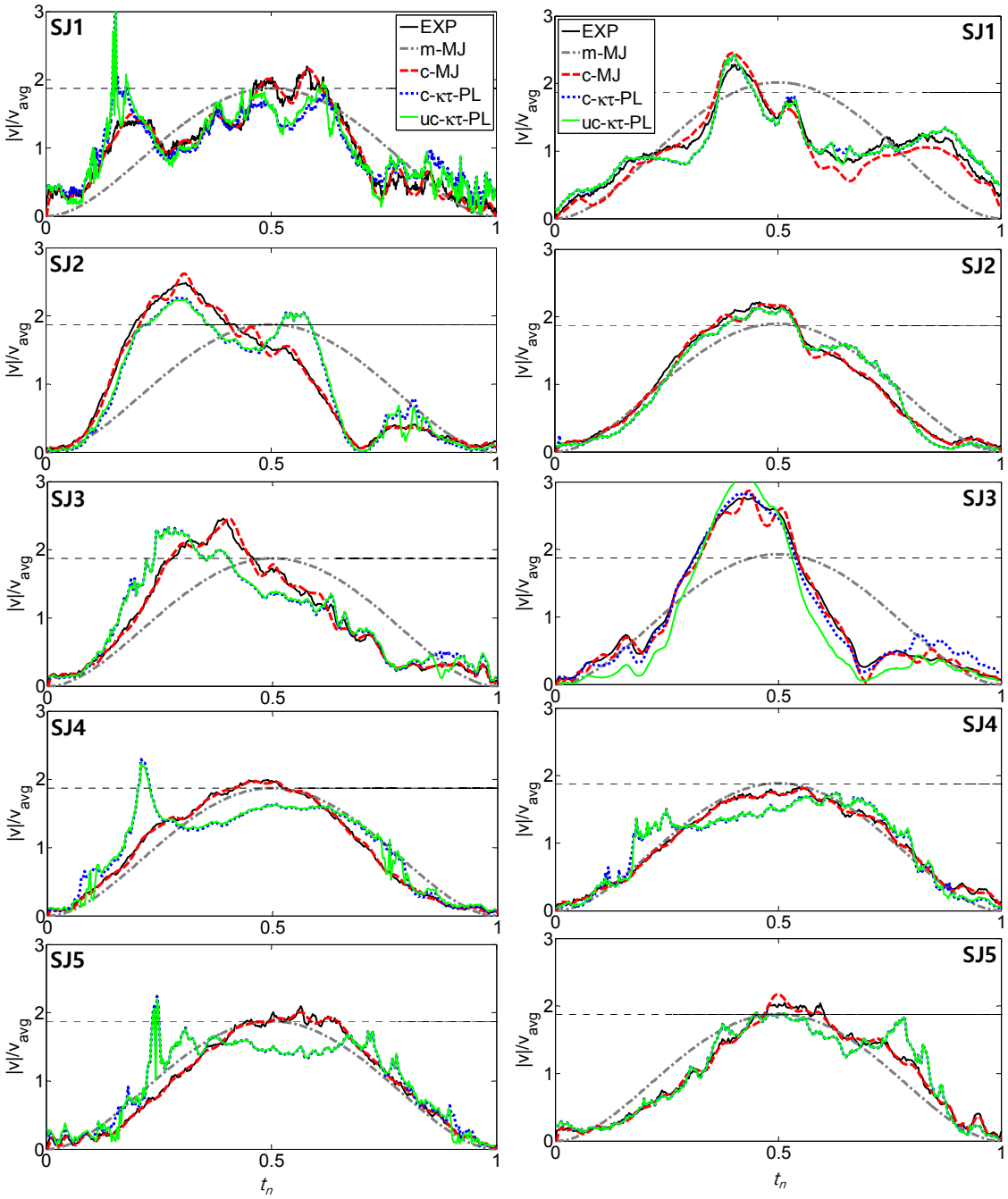

(a) Without elbow constraint (NC). **(b) With elbow constraint (EC).**

Figure 34. Normalized hand speed profile comparison of each subject for selected THLR motions.

instruction regarding the movement speed during the experiment and each subject performed the motions with their self-selected speed. Richardman and Flash [161] studied how the speed profile is changed by varying n that is the order of the mean squared derivative cost function to generate a speed profile. According to their study, higher n induces a larger r that is a ratio of a peak speed v_{peak} over an average speed v_{avg}. Analytic solutions of the m-MJ model shown in (109) always have $r_{\text{m-MJ}} = 1.875$ which is very close to the ratio, $r \cong 1.8$, of natural and smooth healthy human arm motions observed in [127]. The m-MJ model always generates an uni-modal symmetric bell shaped speed profile with constant r value regardless of any given conditions (i.e., reaching directions, different subjects, forward/backward motions, and elbow constraint angles). In each subplot of Figure 34, the constant $r_{\text{m-MJ}}$ is marked as a horizontal grid line. It can be noticed that every m-MJ model profile matches its peak amplitude to the grid line. Notice that some speed profiles have more local peaks than the others. This characteristic is matched with the waviness of the hand path geometry which is quantified by the angle ϑ defined in (105). Figure 35 shows the distribution of the number of local peaks (NLP) in the speed profile for each subject. The threshold of the local peak was set as 0.1 normalized speed amplitude over v_{avg} beside local valleys. The SJ1 and the SJ5 show wider range of NLP (see Figure 35) and ZC(ϑ) (see Figure 32). From this we can infer that the NLP of the speed profile is correlated with the waviness of the path geometry. It is partially confirmed from scatter plots shown in Figure 36. Correlations of the NLP and the ZC for each subject in NC and EC cases are shown in Figure 36(a) and Figure 36(b), respectively. In the figure, for subjects who have wider distribution range of the ZC(ϑ) and the NLP

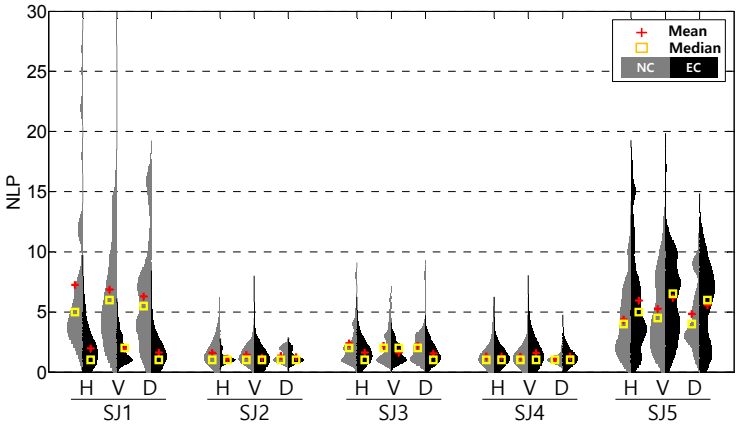

Figure 35. Distribution plot of the NLP (number of local peaks) in speed profiles for each subject

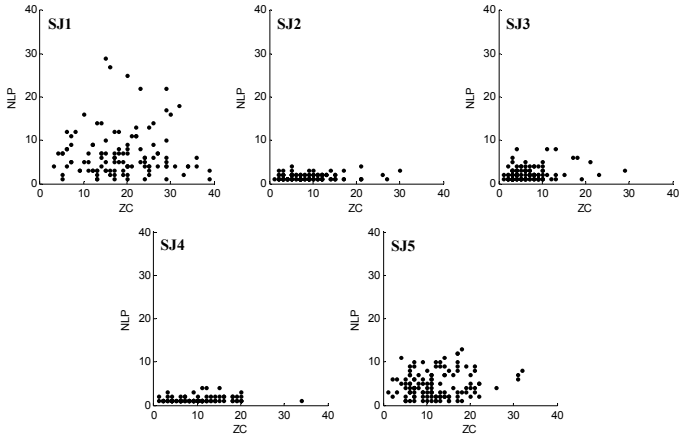

(a) Without elbow constraint (NC)

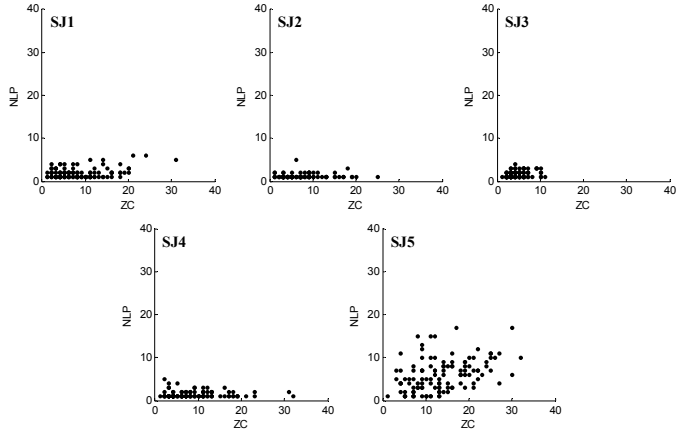

(b) With elbow constraint (EC)

Figure 36. Scatter plot of the ZC and the NLP for each subject

show more correlated scatter plots (see SJ1 and SJ5 in Figure 36(a) and SJ5 in Figure 36(b)). However, the degree of manifestation of such relation between the hand path geometry and the speed profile seems depending on the subject's ability of motor control. In Figure 36, some subjects (i.e., SJ2, SJ3 and SJ4) show better control on smoothing the speed profile regardless of the curviness of the hand path (i.e., they hold constant NLP for wide ranges of ZC). On the other hands, the SJ5 always reveals a trend of proportional relation between the complexity of the hand path geometry and the roughness of the hand speed profile.

It is considered that such deviations of motor control ability are due to proportions of the feed forward and the feedback control efforts in the control engineering viewpoint:

1) The control command from the CNS is composed of a feed forward signal u_{ff} and a corrective feedback signal u_{fb} (see Figure 23),
2) Since the u_{ff} is generated based on an internal inverse model without a time delay (theoretically), well-trained (or skillful) actions are dominated by it,
3) Therefore, the total motion kinematics is an outcome of an initial burst driven by the u_{ff} and the corrective motion by the u_{fb},
4) As the subject is more relying on the feed forward control, the resulting motion gets more relying on the initial burst by the u_{ff} or vice versa,
5) The faster motion induces higher proportion of the kinetic torque, which is a function of the movement speed, in the total joint torque (see (90)), and
6) Since the kinetic torque is equivalent to the dynamic torque (i.e., the summation of inertia, centrifugal and Coriolis torques), the hand kinematics is mostly derived

by the natural arm dynamics without much of the corrective control effort from the CNS during the travel.

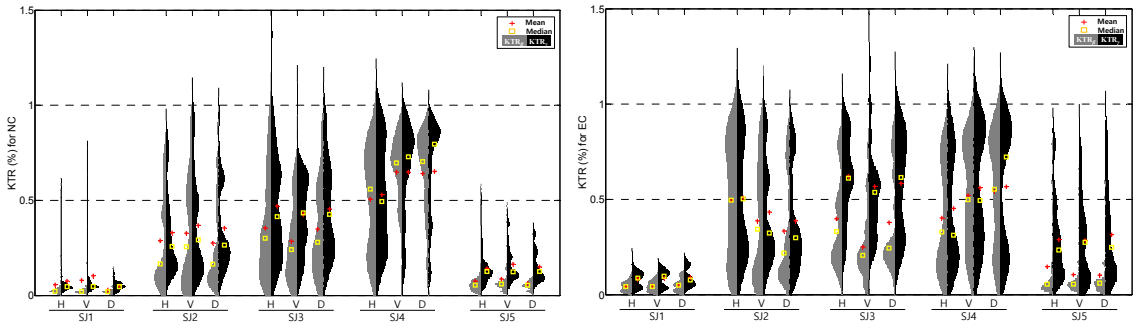

(a) Without elbow constraint (NC) **(b) With elbow constraint (EC)**

Figure 37. Violin plots of the KTR (kinetic torque ratio) of the shoulder elevation β and the humeral rotation γ for each subject

Figure 37 represents the kinetic torque ratio (KTR) of the shoulder elevation β and the humeral rotation γ over the total IJC torque derived as:

$$KTR_i = \frac{\sum |\tau_{k,i}|}{\sum |\tau_i|} \times 100\,(\%), \tag{116}$$

where τ_i and $\tau_{k,i}$ are the total and the kinetic torque of the i-th IJC DOF (i=1 for β and i=2 for γ, see (90)). The shoulder azimuth α is not taken into account since it is driven solely by the kinetic torque without any gravitational torque (see the joint DOF definition in Figure 24(b) for the clarification). In violin plots, subjects who showed consistent control over the smoothness of speed profile (i.e., SJ2, SJ3 and SJ4) have higher proportion of τ_k

than other subjects both in β and γ DOF regardless of the elbow constraint condition. This can be an evidence supporting 5) in the list above. Overall, a feed forward dominant control effort induces a stronger initial burst. Such control strategy increases the proportion of the dynamic torque compare to the static torque and decreases relative chances of the CNS to intervene and to make corrective efforts. This leads to smoother hand speed profiles. According to this reasoning, the temporal control of a hand motion is closely related to the motor control strategy of the CNS. In this sense, the m-MJ model is generally a good fit since it reflects the feed forward dominant nature of well-trained reaching movements. Due to its constant amplitude ratio and the identical bell shape independent of the hand path geometry, however, the m-MJ is not the best model that can explain the governing rule of temporal control. In this context, other models (i.e., c-$\kappa\tau$-PL, uc-$\kappa\tau$-PL and c-MJ) that reflect the differential kinematics of the hand path can be better interpretation tools to understand the human strategy (see better fits of such models compared to the m-MJ in Figure 34).

In order to find the best model that describes the governing rule of temporal control, quantitative analysis indices are adopted. SID is a dissimilarity index that quantifies the amount of non-overlapped area between two speed profiles as introduced in [93, 129]:

$$\text{SID}=\frac{\sum_{j=1}^{N}\left|v_{EXP,j}-v_{M,j}\right|}{\sum_{j=1}^{N}\max\left(v_{EXP,j},v_{M,j}\right)}, \tag{117}$$

where N refers to the number of samples within the trial. The $v_{EXP,j}$ and the $v_{M,j}$ indicate velocities of the experimental data and the model output at the j-th sample index. SID quantifies the dissimilarity between two speed profiles as a proportion of non-overlapped area over total area [93, 129] (see Figure 38 for the clarification on area terms). For given two speed profiles represented on the same time frame, the total area A_{tot} and the overlapped area A_{over} can be approximated by:

$$\begin{aligned} A_{tot} &= \sum_{j=1}^{N} \max\left(v_{EXP,j} - v_{M,j}\right)\Delta t, \\ A_{over} &= \sum_{j=1}^{N} \min\left(v_{EXP,j} - v_{M,j}\right)\Delta t \end{aligned} \tag{118}$$

where $v_{EXP,j}$ and $v_{M,j}$ refer to velocity values of the experimental data and of the model output at j-th data point. The notation N is the total number of data point in the trial and Δt is the sampling time. Thus SID can be derived as:

$$\begin{aligned} SID &= \frac{A_{tot} - A_{over}}{A_{tot}} \\ &= \frac{\sum_{j=1}^{N}\left[\max\left(v_{EXP,j} - v_{M,j}\right) - \min\left(v_{EXP,j} - v_{M,j}\right)\right]\Delta t}{\sum_{j=1}^{N}\max\left(v_{EXP,j} - v_{M,j}\right)\Delta t} \\ &= \frac{\sum_{j=1}^{N}\left|v_{EXP,j} - v_{M,j}\right|}{\sum_{j=1}^{N}\max\left(v_{EXP,j} - v_{M,j}\right)}. \end{aligned} \tag{119}$$

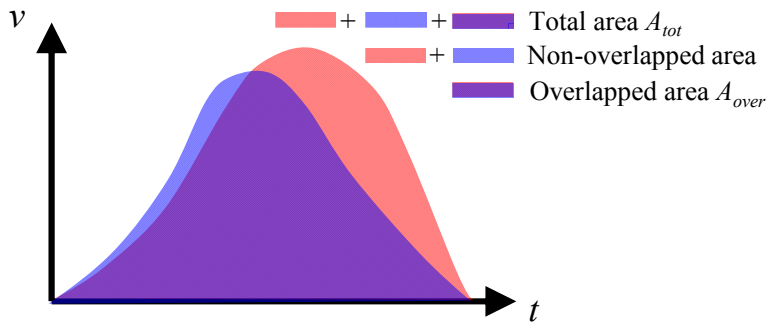

Figure 38. Dissimilarity of two profiles and explanations on each area term [129].

The geometrical similarity of the two speed profiles is measured by the SID. As the SID approaches to zero, two profiles should perfectly match. On the other hand, as the SID is getting closer to one, two profiles do not overlap at all within the given time window [93, 129]. Another index, unexplained variance (UV) is adopted from [157] to measure the complement of the squared correlation coefficient:

$$\mathrm{UV}=1-\left(\frac{\sum_{j=1}^{N}\left(X_j-\bar{X}\right)\left(M_j-\bar{M}\right)}{\sqrt{\sum_{j=1}^{N}\left(X_j-\bar{X}\right)^2\sum_{j=1}^{N}\left(M_j-\bar{M}\right)^2}}\right)^2, \tag{120}$$

where X_j and M_j indicate the experimental data and the model output at j-th sample index. The upper bar represents a mean value. The SID and UV distributions of each model across all trials of all subjects are compared in Figure 39. In the figure, the c-MJ model shows the best fit both in SID and UV measurements. Note that some of the c-MJ solution contain unrealizable peaks spans to the infinity due to ill-conditioned nonlinear

optimization (i.e., the fminsearch.m used in the min_jerk.m code provided by Todorov [158]). Except for those unrealizable peaks, the c-MJ model is obviously the best fit. Next, the c-$\kappa\tau$-PL and the uc-$\kappa\tau$-PL fits the experimental data with almost negligible deviations. As expected, it turns out that the m-MJ model is the worst fit. Figure 40 represents scatter plots of all fitting models for each subject. The models have higher correlations with the experimental speed profile in an order of c-MJ > uc-$\kappa\tau$-PL $\geq$ c-$\kappa\tau$-PL > m-MJ for all subjects regardless of the elbow constraint condition. For most cases, c-MJ model shows the closest data points to the reference line which indicates the perfect match with the experimental data. Some scatter points of the c-MJ model have large deviation from the reference line (see SJ3 for example). Those points are due to unrealizable peaks that are induced by an ill-conditioned nonlinear optimization.

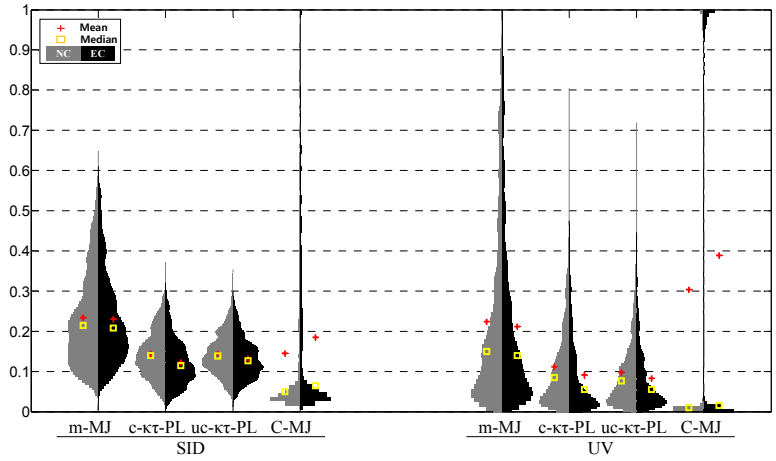

Figure 39. Computed dissimilarity index (SID) and unexplained variance (UV) distributions across all trials of all subjects

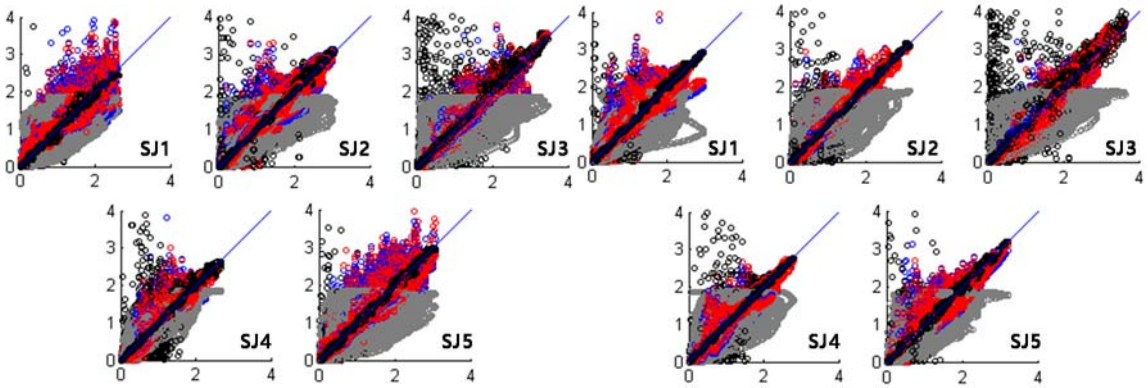

(a) Without elbow constraint (NC) **(b) With elbow constraint (EC)**

Figure 40. Scatter plot of the experimental data and the model data for each subject

Table 12. Adjusted exponents of the $\kappa\tau$-PL models for each subject

		SJ1	SJ2	SJ3	SJ4	SJ5
NC	μ	-0.354±0.084	-0.611±0.150	-0.417±0.092	-0.501±0.131	-0.430±0.109
	η	-0.355±0.077	-0.629±0.145	-0.480±0.136	-0.569±0.162	-0.433±0.111
	ρ	-0.664±0.409	-1.17±1.06	-1.13±0.799	-1.10±0.844	-1.17±0.733
EC	μ	-0.528±0.159	-0.605±0.137	-0.423±0.061	-0.566±0.164	-0.573±0.161
	η	-0.538±0.160	-0.657±0.129	-0.536±0.143	-0.621±0.160	-0.577±0.164
	ρ	-1.05±0.858	-0.844±0.760	-1.22±0.969	-1.15±0.928	-1.18±1.02

According to the equi-affine speed concept explained in [159], exponents μ and η of power laws are theoretically $-1/3 \approx -0.333$, and the ρ is close to $-1/6 \approx -0.167$ to preserve the isogony principle based on the path geometry. The mean and standard deviation of those exponents adjusted for each experimental subject are presented in Table 12.

Overall, the c-MJ model shows the best fit to the experimental speed profile across all trials of all subjects. This implies that the temporal control tends to minimizes the full hand jerk components to maximize the smoothness of motion. Therefore, it is confirmed that the temporal governing rule for the healthy arm reaching shown in [127] and [157] is

preserved against the elbow constrained condition. From the observations, it is considered that the smoothness is the best feature that the CNS tries to keep during the motion coordination regardless of the hand path geometry. The ability of temporal control to maximize such smoothness depends on the control strategy utilized by the CNS. As the feed forward control effort gets more dominant, the entire motion profile is relying on the initial burst with lesser corrective efforts along the motion (i.e., feedback control from the sensory inputs). Though the c-MJ model, which minimizes true hand jerk magnitude in the differential kinematics sense, is the best fitting model to approximate the temporal strategy of the CNS, it requires a time-consuming nonlinear optimization process. For this reason, it is considered that the curvature-torsion power laws are more efficient with good approximations in the computational cost viewpoint. In a real-time application, such as HIR controller design, the curvature-torsion power laws are better choices for generating the end-effector speed profile. In addition, in-accurate approximations of the power laws especially at low speed points can be adjusted by combining the minimum jerk model concept.

3.6.4. Redundant inverse kinematics: arm posture selection

In the ETC, the elbow swivel angle ψ is the single variable to govern the arm posture selection for a given hand position. Since most of the conscious attention is on the hand trajectory formulation during a point-to-point reaching, the arm posture selection mechanism should be considered in internal body coordinates (i.e., IJC), which is considered to be directly linked to the unconscious level of the CNS. Therefore, kinematic/dynamic contributions of the IJC angles/torques on each motion component

represented by an ETC angle/torque are computed by (91) to (96). Figure 41 shows the overall information captured from a subject's selected THLR motion with 60° elbow constraint. The arm posture history is represented by triangular arm plane along the hand path in Figure 41(a). The ETC angles are shown in the uppermost subfigure of Figure 41(b). The middle and the lowermost subfigures in Figure 41(b) refer to the kinetic torque $\boldsymbol{\tau}_{\boldsymbol{\Theta},\mathbf{k}}$ and the gravitational torque $\boldsymbol{\tau}_{\boldsymbol{\Theta},\mathbf{g}}$ in ETC computed via (96). Each component of $\boldsymbol{\tau}_{\mathbf{A},\mathbf{k}}$ and $\boldsymbol{\tau}_{\mathbf{A},\mathbf{g}}$ calculated in (90) is plotted in the middle and the lowermost subfigures in Figure 41(c). Each of Figure 41(d-f) shows IJC contributions on ETC angle/torque values in Figure 41(b). Each row of the kinematic contributions defined by (93) is drawn in Figure 41(d) as each subfigure. The IJC contributions on each component of the kinetic torque $\boldsymbol{\tau}_{\boldsymbol{\Theta},\mathbf{k}}$ in ETC (i.e., the middle subfigure of Figure 41(b)) are plotted in Figure 41(e). Likewise, Figure 41(f) represents the IJC contributions on $\boldsymbol{\tau}_{\boldsymbol{\Theta},\mathbf{g}}$ shown in the lowermost subfigure in Figure 41(b). Each abscissa of Figure 41(b-f) is the normalized time frame t_n.

Due to horizontal direction of movement (see the solid curve on the spherical surface in Figure 41(a)), the latitude θ is almost constant while the longitude ϕ dominates the hand path geometry as shown in the uppermost subfigure in Figure 41(b). In IJC, the azimuth α and the elevation β behave as the corresponding ETC angles (i.e., ϕ and θ, respectively). This can be confirmed from the kinematic contribution plot shown in Figure 41(d): i.e., ω_α has the largest contribution on ω_ϕ. Regardless of its representation coordinates, the gravitational torque is almost constant (see the lowermost subfigures in Figure 41(b, c) and Figure 41(f)). The longitudinal ETC kinetic torque (i.e., ϕ portion of $\boldsymbol{\tau}_{\boldsymbol{\Theta},\mathbf{k}}$: see dash-dot line in the middle subfigure of Figure 41(b)) is dominated by the

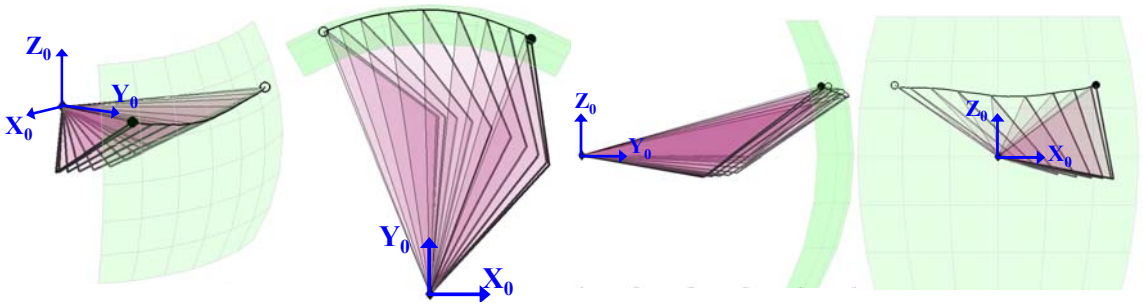

(a) Arm posture history plot in 3D space and its 2D projections. Initial and final hand positions are represented as empty and filled circles, respectively, and they are connected by the hand path (solid line). Black diamond indicates the shoulder position where the global frame $X_0Y_0Z_0$ is located.

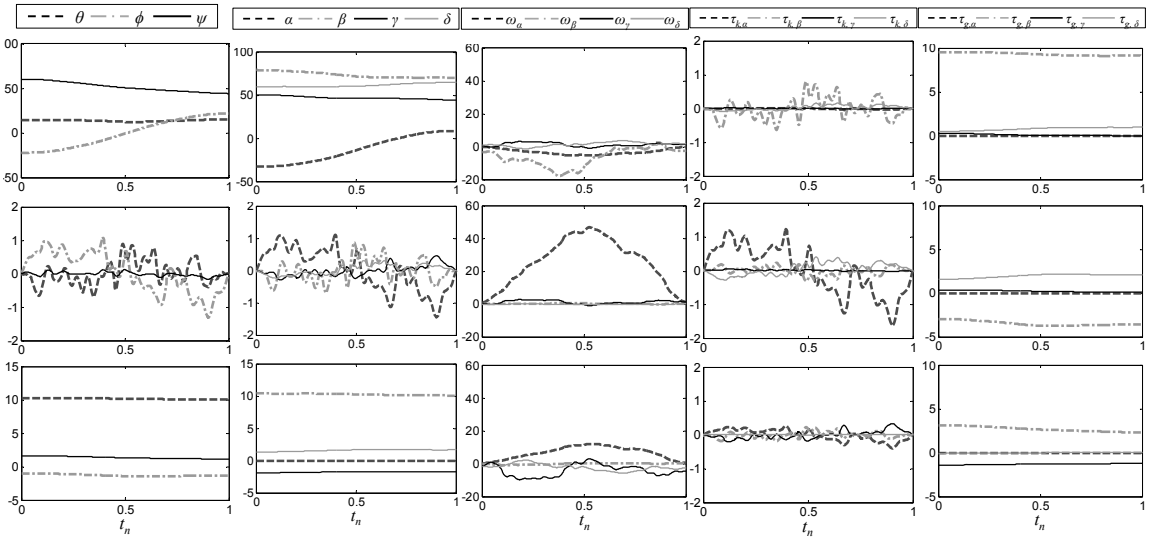

(b) ETC angles and torques | **(c) IJC angles and torques** | **(d) Kinematic contribution** | **(e) IJC contributions on $\tau_{\Theta,k}$** | **(f) IJC contributions on $\tau_{\Theta,g}$**

Figure 41. Overall kinematic/dynamic information captured from a subject's selected THLR motion.

azimuth kinetic torque $\tau_{k,\alpha}$ in IJC (see the middle subfigure in Figure 41(e)). During the THLR motion, the elbow swivel angle ψ constantly decreases and is mostly driven by a combination of the humeral rotation γ and the shoulder azimuth α from kinematic aspect (see the lowermost subfigure in Figure 41(d)). At the same time, in order to keep the constant latitude θ (see dashed line in the uppermost subfigure of Figure 41(b)), the

shoulder elevation β (see dash-dot line in the uppermost subfigure of Figure 41(c)) compensates the θ variation induced by the humeral rotation γ (see black continuous line in the uppermost subfigure of Figure 41(c)). This combinatory action of β and γ induce the arm plane rotation (i.e., elbow swivel angle ψ) that can be seen in the lowermost subfigure of Figure 41(d). From dynamic viewpoint, the generated kinetic torque on humeral rotation (i.e., $\tau_{k,\gamma}$ in the lowermost subfigure in Figure 41(e)) is compensated by the kinetic torque on azimuth DOF (i.e., $\tau_{k,\alpha}$) and its resultant torque on the ψ portion of $\boldsymbol{\tau}_{\boldsymbol{\Theta},\mathbf{k}}$ (see the solid line in the middle subfigure of Figure 41(b)) was minimized.

Overall, it is considered that the CNS coordinates the elbow constrained arm to cost minimum kinetic energy (MKE) to drive the arm plane while the hand path geometry tracks LKE (least kinematic effort: i.e., either the geodesic curve or the rhumb line). In order to reach its hand to a given target task point (see filled circles in Figure 41(a)) by drawing a horizontal hand path, the CNS drives the arm plane to rotate about the vertical axis (see Z_0 in Figure 41(a)) and the axis of the elbow swivel angle, simultaneously. Each rotation corresponds to ϕ and ψ in ETC. The ϕ motion, which is dominated by α in IJC, is incorporated only in the hand path geometry formulation. Here, the humeral rotation γ is adopted to reduce the cost of kinetic energy. Compared to α motion, γ costs less rotational kinetic energy due to smaller moment of inertia (i.e., consider a rotation about the longitudinal axis of the upper arm link and compare it with a rotation about Z_0 in the third subfigure of Figure 41(a)). Also, γ rotation can reduce translational kinetic energy cost by lessen translations of the upper arm link, which has larger mass than the forearm link. Since the adopted γ rotation induces changes in θ portion of the hand path geometry, β is

lowered to keep θ as a constant. Consequently, the elbow swivel angle ψ is generated as combinatory motions of β and γ with the minimized kinetic torque on ψ.

In order to verify the inferred arm posture selection strategy (i.e., minimum kinetic energy for driving the arm plane) in another directional motion, overall information captured from the same subject's selected RVDU (right vertical down to up) motion is represented in Figure 42. As expected, the latitude motion dominates the hand path geometry as a combinatory result of β and γ contributions both in kinematic and dynamic aspects (see the uppermost subfigures in Figure 42(d, e)). From the kinetic torque plots, the ψ portion of $\boldsymbol{\tau}_{\boldsymbol{\Theta},\mathbf{k}}$ (see the solid line in the middle subfigure of Figure 42(b)) is minimized by $\tau_{k,\beta}$ and $\tau_{k,\gamma}$ acting in opposite direction. Overall, for drawing a vertical hand path, the shoulder elevation β drives the arm plane against the gravity while the humeral rotation γ helps it to reduce the required kinetic energy cost. Here, in order to keep the constant longitude ϕ, the shoulder azimuth β is incorporated. Therefore, by the combination of α, β and γ motions, the arm plane rotates about the axis of ψ while the hand tends to follow the LKE path (see the solid lines from the empty to the filled circles). It is believed that this arm plane rotation reduces the kinetic energy cost with the same reason as stated in observations of the THLR motion. For diagonal motions, blending of similar phenomena from THLR and RVDU motions were found.

In order to verify in a quantitative manner that the CNS actively incorporates the humeral rotation γ both for hand path formulation and arm posture selection in an elbow constrained reaching, the percentage of each IJC angular contribution within each ETC component is defined as:

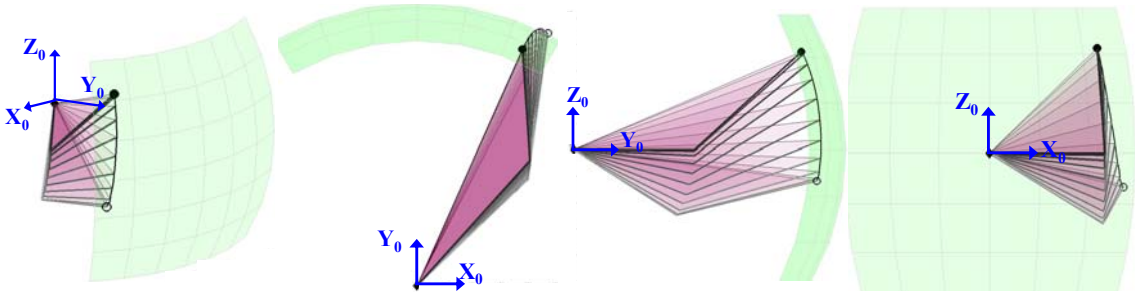

(a) Arm posture history plot in 3D space and its 2D projections. Initial and final hand positions are represented as empty and filled circles, respectively, and they are connected by the hand path (solid line). Black diamond indicates the shoulder position where the global frame $X_0Y_0Z_0$ is located.

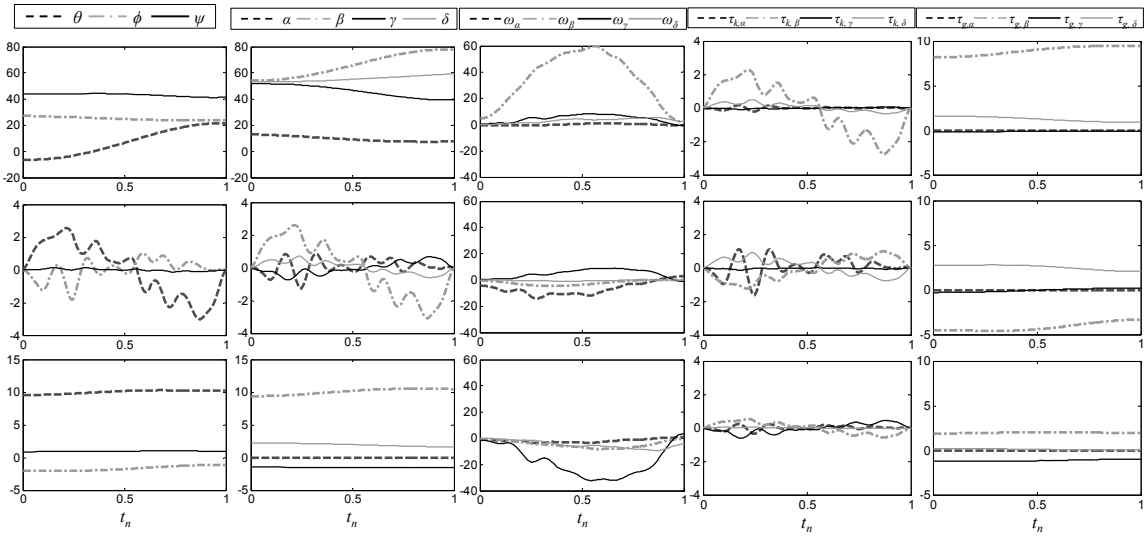

(b) ETC angles and torques **(c) IJC angles and torques** **(d) Kinematic contribution** **(e) IJC contributions on $\tau_{\Theta,k}$** **(f) IJC contributions on $\tau_{\Theta,g}$**

Figure 42. Overall kinematic/dynamic information captured from a subject's selected RVDU motion.

$$KC_i = \frac{1}{N}\sum_{j=1}^{N}\left(\frac{\left|J\omega_i(j)\right|}{\sum_{i=1}^{4}\left|J\omega_i(j)\right|}\times 100(\%)\right), \tag{121}$$

$$DC_i = \frac{1}{N}\sum_{j=1}^{N}\left(\frac{\left|J\tau_{k,i}(j)\right|}{\sum_{i=1}^{4}\left|J\tau_{k,i}(j)\right|}\times 100(\%)\right), \tag{122}$$

where KC_i and DC_i stand for kinematic contribution and dynamic contribution of i-th IJC DOF. The notations $J\omega_i(j)$ and $J\tau_{k,i}(j)$ refer to angular velocity and kinetic torque of i-th IJC DOF multiplied by a corresponding Jacobian component as shown in equation (93) and equation (96) at the j-th data point along the normalized time frame t_n and N is the total number of data point within the trial. The kinematic and dynamic contributions KC_i and DC_i are computed for each component of $\mathbf{\Omega_\Theta}$ and $\boldsymbol{\tau}_{\boldsymbol{\Theta},\mathbf{k}}$ shown in (93) and (96) to quantify mean absolute contribution of each IJC DOF within ETC representation. Figure 43 shows violin plots of the distribution of the calculated (121) and (122) across all trials of all subjects. In the figure, it can be noticed that the humeral rotation γ has significant kinematic contributions in major hand path component (e.g., longitude ϕ in horizontal motions or latitude θ in vertical motions) and arm posture component ψ in ETC regardless of reaching directions. The dynamic contribution of γ is also noteworthy regardless of elbow conditions.

In the kinetic torque contribution plot $\tau_{k,\gamma}$ shows significant contributions regardless of reaching directions (see black distributions in the lowermost subfigures of Figure 43). Note that both kinematic and dynamic contributions of the humeral rotation are the most dominant compared to other IJC DOF. Meanwhile, ω_γ has the second dominant contribution amounts following the dominant hand path directional angular

velocity from the kinematic contribution aspect. This implies that the γ angle induces ψ motion more efficiently than other IJC DOF motions with similar amount of kinetic torque. Therefore, the distributions on computed KC_i and DC_i support the idea that for an elbow constraint point-to-point reaching motions, the motor system actively recruits γ motion to reduce the required kinetic energy cost.

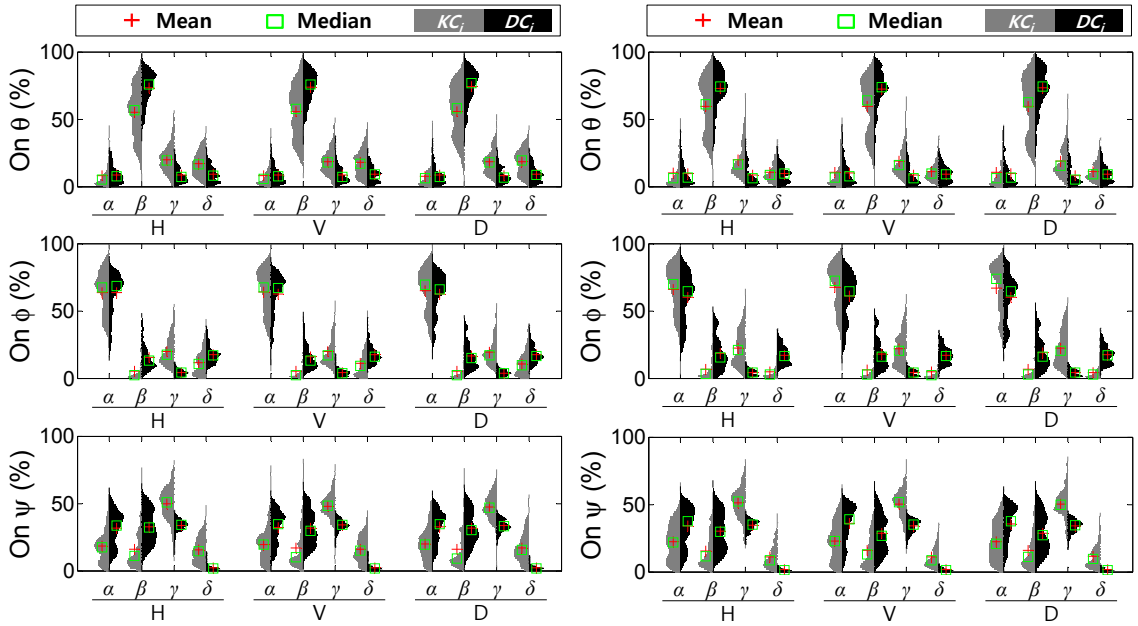

(a) Without elbow constraint (NC) **(b) With elbow constraint (EC)**

Figure 43. Computed KC_i and DC_i values across all trials of all subjects.

3.6.5. Conclusion

The governing strategies implemented in the central nervous system (CNS) that resolves two redundant mapping problems of point-to-point reaching (the hand path formulation and the arm posture selection) were identified from experimental observation approach. The novelty of this study is on the imposed elbow joint kinematic constraint during the

experiment which enables us to tap into fundamental principles of motor coordination by inducing resultant feature of the governing rules despite the given constraint condition.

For the hand path geometry formulation, the least kinematic effort (LKE) models (i.e., geodesic curves and rhumb lines on the constraint workspace) were compared with the experimental data. For the constraint elbow case (EC), both LKE models have insignificant deviations with the experimental data while the non-constraint case (NC) shows larger deviations of the hand path geometry. It can be explained that the distance control DOF (i.e., elbow joint DOF) has a significant contribution on the hand path geometry formulation. From better approximations of rhume lines than geodesics in the NC case, we can infer that the CNS prefers spherical coordinates than perpendicular Cartesian coordinates to generate reaching motions. This finding was confirmed by qualitative analyses of the arc length comparison and the geometrical similarities. As the designed experimental motions are defined on a frontal plane of subjects, LKE models showed generally good approximations to experimental hand paths. However, nontrivial lateral motions were observed from the experimental hand paths which induce wavy path geometries. The waviness of the path geometry was quantified by an angle between tangential vectors of the geodesic curve and the experimental hand path at equally spaced intermediate points. From the detailed quantitative analysis in terms of arc length and geometrical similarity of curves, it was concluded that the actual hand path is not solely planned by LKE principle.

For the temporal control of motion, the modified minimum jerk (m-MJ) model and the constrained minimum jerk (m-MJ) model are adopted to focus on the smoothness of

natural human hand speed profiles. In addition, the constrained and the unconstrained versions of the curvature torsion power law ($\kappa\tau$-PL) models are also used to represent the isogony principle in writing and drawing actions. From the comparison with the experimental data, the c-MJ model shows the best fit which implies that the best explanation of the temporal control of the CNS is the smoothness maximization. However, the c-MJ model requires a non-linear optimization process that is computationally expensive especially for real-time applications. For this reason, curvature and torsion power laws can be employed to predict/reproduce natural hand speed profile with a relative good approximations and an affordable computational cost for real-time applications such as the HIR control. As the geometrical complexity of the hand path is quantified by the zero crossing of deviation angles, $ZC(\vartheta)$, the complexity of the hand speed profile is determined by the NLP (number of local peaks). Generally, a proportional relationship between two complexities were found from the experimental data. From the observation on the statistical analysis, however, an interesting inter-subject difference of the proportionality was found that some subjects have better control ability to generate smoother speed profile regardless of geometrical complexity of the hand path. It is explained from the control engineering viewpoint. As a subject depends more on the feed forward control, the initial burst dominates the corrective efforts along a motion, and this enables smoother speed profiles. This finding is supported by the kinetic torque ratio (KTR) that the KTR gets higher for those subjects who are more depending on the initial burst.

For identifying the arm posture selection strategy, kinematic and dynamic contribution amount of IJC DOF on each component of ETC representation were

quantified. From the analysis, it was inferred that the CNS actively recruits the humeral rotation both for hand path formulation and arm posture selection to minimize the required kinetic energy. This finding is supported from examples of THLR and RVDU motions with 60° elbow. Distributions of mean contribution values also confirmed the idea of minimum kinetic energy (MKE) principle.

4. APPROXIMATING CONSTRAINED HAND PATHS VIA KINEMATIC SYNTHESIS WITH CONTACT SPECIFICATIONS*

4.1.Introduction

In this section, it is hypothesized that the hand contact conditions play an important role in governing rules to coordinate a point-to-point reaching in a stereotyped manner. Contact conditions of a hand with one or more objects can define velocity and acceleration specifications in the vicinity of those contact points based on theoretical backgrounds by Rimon and Burdic [162, 163]. Recently, Robson and McCarthy [164] introduced a systematic method for the kinematic synthesis of planar mechanical linkages such that they do not violate normal direction and curvature constraints imposed by contacts with objects. Using the geometry of the task, they showed how to transform these constraints into velocity and acceleration specifications of the moving body/end-effector. Their work was further continued by Robson and Tolety [165], who extended the contact geometry problem to the three dimensional case.

In this dissertation, it is believed that the CNS senses directional constraints on hand velocity, acceleration and higher derivative vectors due to relative curvatures of contact geometries and utilizes them while generating a hand profile. Consider that a targeting hand position is assigned as an only input for planning and executing a point-to-

* Reprinted with kind permission from Springer Science+Businees Media: *Advances in Robot Kinematics*, "Approximating Constrained Hand Paths via Kinematic Synthesis with Contact Specification", 2014, pp. 375-384, H. Moon, N. Robson and R. Langari.

point reaching. Then, the CNS needs to generate a hand path to fill out a gap to the targeting hand position from an initial state. When there is a contact condition imposed at each task point, directions of hand velocity and acceleration vectors are constrained by contact geometries in the vicinity of each task point. As a result, the specified contact conditions can assist the CNS to reduce a range of possible hand profile solutions: i.e., the solution set can be filtered to meet those kinematic specifications simultaneously. In this manner, it is believed that the entire hand profile can be approximated, reproduced or predicted by using the linkage kinematic synthesis techniques with the given contact conditions. In this study, elbow constrained reaching movements on a spherical workspace are approximated via the previously developed spatial SS linkage synthesis for contact specifications shown in [165]. The spherical contact condition was realized by an elbow joint constraint with a medical brace in the experiment as described in Section 3.5.

4.2. Human Arm Kinematic Model with a Constrained Elbow Joint

As introduced in Section 3.4.1, human arm kinematics can be simplified as a seven DOF SRS chain. When the elbow joint is fixed, the arm kinematics changes to a serial SS chain, characterized by a spherical workspace centered at the shoulder. In order to represent the motion kinematics of the elbow constrained arm, an extended version of the intrinsic joint coordinates (IJC) defined in Figure 25(b) is utilized. The coordinate system consists of the shoulder azimuth α, the humeral elevation β, the humeral rotation γ, and the elbow flexion δ. Note that δ is fixed as a constant in this study due to the elbow joint constraint condition.

For the sake of simplicity, the three wrist DOF are neglected and considered as fixed due to their minor roles in pointing motions.

The hand location $(X_h, \Theta_h)^T = (x_h, y_h, z_h, \theta_h, \phi_h, \psi_h)^T$ in the Cartesian space can be obtained by the forward kinematics:

$$\begin{bmatrix} x_h \\ y_h \\ z_h \\ \theta_h \\ \phi_h \\ \psi_h \end{bmatrix} = \begin{bmatrix} l_u s_\alpha s_\beta - l_f \left(s_\delta \left(c_\alpha s_\gamma - s_\alpha c_\beta c_\gamma \right) - s_\alpha s_\beta c_\delta \right) \\ l_u c_\alpha s_\beta + l_f \left(s_\delta \left(s_\alpha s_\gamma + c_\alpha c_\beta c_\gamma \right) + c_\alpha s_\beta c_\delta \right) \\ -l_u c_\beta - l_f \left(c_\beta c_\delta - s_\beta c_\gamma s_\delta \right) \\ \text{asin}\left(c_\delta \left(s_\alpha s_\gamma + c_\alpha c_\beta c_\gamma \right) - c_\alpha s_\beta s_\delta \right) \\ \text{atan2}\left(s_\alpha c_\gamma - c_\alpha c_\beta s_\gamma, s_\delta \left(s_\alpha s_\gamma + c_\alpha c_\beta c_\gamma \right) + c_\alpha s_\beta c_\delta \right) \\ \text{atan2}\left(c_\delta \left(c_\alpha s_\gamma - s_\alpha c_\beta c_\gamma \right) + s_\alpha s_\beta s_\delta, -c_\beta s_\delta - s_\beta c_\gamma c_\delta \right) \end{bmatrix}, \quad (123)$$

where l_u and l_f indicate the upper arm and the forearm link lengths, and cos(.) and sin(.) are noted as $c_{(.)}$ and $s_{(.)}$, respectively. Here, θ_h, ϕ_h and ψ_h refer pitch, yaw and roll orientation angles of the hand that are corresponding to directions of anatomical joint articulations: wrist flexion, radial deviation and forearm pronation, respectively. Each joint angle can be derived from the hand position vector $\mathbf{X_h} = (x_h, y_h, z_h)^T$ and the elbow position vector $\mathbf{X_e} = (x_e, y_e, z_e)^T$ by using the inverse kinematics defined in (26) in Section 2.4.2.2. In the following subsection, a brief review of the background, described in detail in [165], needed for the development of the approximation model of the elbow joint constrained hand path.

4.3. Higher Order Motion Specifications Defined from Relative Curvatures of Contact Geometries: Background

Let the movement of the moving frame M, located at the wrist joint, be defined by the parameterized set of 4 × 4 homogeneous transforms $[T(t)]=[R(t), \mathbf{d}(t)]$ constructed from a rotation matrix $R(t)$, composed of roll $\psi(t)$, pitch $\theta(t)$ and yaw $\phi(t)$ angles, and translation vector $\mathbf{d}(t) = (d_x(t), d_y(t), d_z(t))^{\mathrm{T}}$:

$$\left[T(t)\right]=\begin{bmatrix} c_{\phi(t)}c_{\psi(t)}+s_{\theta(t)}s_{\phi(t)}s_{\psi(t)} & s_{\theta(t)}c_{\phi(t)}s_{\psi(t)}-s_{\phi(t)}c_{\psi(t)} & c_{\theta(t)}s_{\psi(t)} & d_x(t) \\ c_{\theta(t)}s_{\phi(t)} & c_{\theta(t)}c_{\phi(t)} & -s_{\theta(t)} & d_y(t) \\ s_{\theta(t)}s_{\phi(t)}c_{\psi(t)} & s_{\phi(t)}s_{\psi(t)}+s_{\theta(t)}c_{\phi(t)}c_{\psi(t)} & c_{\theta(t)}c_{\psi(t)} & d_z(t) \\ 0 & 0 & 0 & 1 \end{bmatrix}. \quad (124)$$

A point $\mathbf{p}$ fixed in the moving frame M traces a trajectory $\mathbf{P}(t)$ in a fixed global frame F by the $[T(t)]$ and can be approximated by the Taylor series expansion,

$$\mathbf{P}(t)=\left[T(t)\right]\mathbf{p}=\left[T_0+T_1t+\frac{1}{2}T_2t^2+\ldots\right]\mathbf{p} \text{ where } [T_i]=\left.\frac{d^i\left[T(t)\right]}{dt^i}\right|_{t=0}. \quad (125)$$

The matrices $[T_0^j]$, $[T_1^j]$ and $[T_2^j]$ are defined by the position, velocity and acceleration of the end-effector in the vicinity of the two task positions.

Figure 44 presents a schematic plot of an elbow constrained arm, as well as the geometry of the spatial contact problem in the vicinity of a particular position. It can be assumed that the hand is in contact at three points with three spherical objects, with radii

of curvature R_A, R_B and R_C, defined from object geometries at three points. The orientation angles $\theta(t)$, $\phi(t)$ and $\psi(t)$ of the moving frame M are directly derived from hand contact positions, which are obtained from the motion capture system in this study, as presented in [165]. Note that the forward kinematics (123) requires an additional step of deriving IJC joint angles from the captured motion data through the inverse kinematics (26) to obtain orientation angles. The position coordinate transformation $[T_0]$ in (125) can be specified by the derived orientation angles:

$$\begin{aligned}
\theta(t) &= \text{atan2}\left(\frac{\hat{j}\bullet(\mathbf{B}-\mathbf{A})}{|\mathbf{B}-\mathbf{A}|}, \frac{\hat{i}\bullet(\mathbf{B}-\mathbf{A})}{|\mathbf{B}-\mathbf{A}|} \right), \\
\phi(t) &= \text{atan2}\left(\frac{\hat{k}\bullet\big((\mathbf{B}-\mathbf{A})\times(\mathbf{C}-\mathbf{A})\big)\times(\mathbf{B}-\mathbf{A})}{\big|\big((\mathbf{B}-\mathbf{A})\times(\mathbf{C}-\mathbf{A})\big)\times(\mathbf{B}-\mathbf{A})\big|}, \frac{\hat{k}\bullet\big((\mathbf{B}-\mathbf{A})\times(\mathbf{C}-\mathbf{A})\big)}{\big|(\mathbf{B}-\mathbf{A})\times(\mathbf{C}-\mathbf{A})\big|} \right), \\
\psi(t) &= -\text{asin}\left(\frac{\hat{k}\bullet(\mathbf{B}-\mathbf{A})}{|\mathbf{B}-\mathbf{A}|} \right),
\end{aligned} \tag{126}$$

where $\hat{i}$, $\hat{j}$ and $\hat{k}$ are unit vectors along each axis of the fixed frame F.

From the geometry of contact conditions shown in Figure 44, the velocity specifications of contact points can be derived using:

$$\begin{aligned}
\dot{\mathbf{A}} &= \mathbf{w}\times(\mathbf{A}-\mathbf{d}) + \dot{\mathbf{d}} = \mathbf{w}_{\mathbf{O_1A}}\times(\mathbf{A}-\mathbf{O_1}), \\
\dot{\mathbf{B}} &= \mathbf{w}\times(\mathbf{B}-\mathbf{d}) + \dot{\mathbf{d}} = \mathbf{w}_{\mathbf{O_2B}}\times(\mathbf{B}-\mathbf{O_2}), \\
\dot{\mathbf{C}} &= \mathbf{w}\times(\mathbf{C}-\mathbf{d}) + \dot{\mathbf{d}} = \mathbf{w}_{\mathbf{O_3C}}\times(\mathbf{C}-\mathbf{O_3}),
\end{aligned} \tag{127}$$

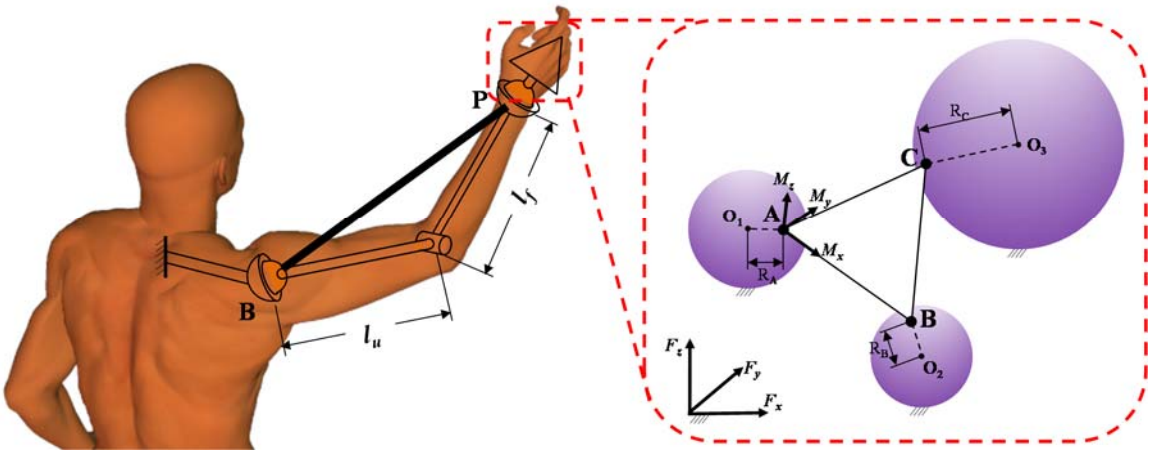

Figure 44. Schematic plot of an elbow constrained arm with contact specifications. B and P refer positions of the base and the moving pivots, respectively

where **w** is a function of $\dot{\theta}$, $\dot{\phi}$ and $\dot{\psi}$. By solving (127) for **w**, the velocity coordinate transformation $[T_1]$ in (125) can be specified. In the same manner, the acceleration specifications at the contact points are:

$$\begin{aligned}
\ddot{\mathbf{A}} &= \mathbf{a}_{\mathrm{O_1A}} \times (\mathbf{A}-\mathbf{O}_1) + \mathbf{w}_{\mathrm{O_1A}} \times \left(\mathbf{w}_{\mathrm{O_1A}} \times (\mathbf{A}-\mathbf{O}_1)\right) = \mathbf{a} \times (\mathbf{A}-\mathbf{d}) + \mathbf{w} \times \left(\mathbf{w} \times (\mathbf{A}-\mathbf{d})\right) + \ddot{\mathbf{d}}, \\
\ddot{\mathbf{B}} &= \mathbf{a}_{\mathrm{O_2B}} \times (\mathbf{B}-\mathbf{O}_2) + \mathbf{w}_{\mathrm{O_2B}} \times \left(\mathbf{w}_{\mathrm{O_2B}} \times (\mathbf{B}-\mathbf{O}_2)\right) = \mathbf{a} \times (\mathbf{B}-\mathbf{d}) + \mathbf{w} \times \left(\mathbf{w} \times (\mathbf{B}-\mathbf{d})\right) + \ddot{\mathbf{d}}, \\
\ddot{\mathbf{C}} &= \mathbf{a}_{\mathrm{O_3C}} \times (\mathbf{C}-\mathbf{O}_3) + \mathbf{w}_{\mathrm{O_3C}} \times \left(\mathbf{w}_{\mathrm{O_3C}} \times (\mathbf{C}-\mathbf{O}_3)\right) = \mathbf{a} \times (\mathbf{C}-\mathbf{d}) + \mathbf{w} \times \left(\mathbf{w} \times (\mathbf{C}-\mathbf{d})\right) + \ddot{\mathbf{d}},
\end{aligned} \tag{128}$$

where **a** is the time derivative of **w**. In order to calculate the acceleration coordinate transformation $[T_2]$ in (125), (128) is solved for **a** which is a function of $\ddot{\theta}$, $\ddot{\phi}$ and $\ddot{\psi}$. In this study, higher order motion specifications (i.e., linear and angular velocities and accelerations in Cartesian space) can be numerically computed from a motion capture data.

4.4. Elbow Constrained Trajectory Generation in Joint Space

The hand trajectory of the elbow constrained arm in the vicinity of the specified task positions can be generated by using (125). In order to produce an entire hand trajectory with a smooth speed profile, a standard robotic trajectory planning technique introduced in [115] is adopted to approximate the elbow constrained hand path, which can be modeled as a spatial SS linkage kinematics. At each task point, the inverse kinematics of the elbow constrained arm shown in (26) enables the conversion of a specified hand position into IJC joint angles. The joint angular velocity vector $\dot{\mathbf{q}}_i = \left(\dot{\alpha}_i, \dot{\beta}_i, \dot{\gamma}_i, \dot{\delta}_i\right)^{\mathrm{T}}$ at the task point i can be solved by

$$V_i = J_i \dot{\mathbf{q}}_i, \tag{129}$$

where $V_i = (\mathbf{v}_i^{\mathrm{T}}, \omega_i^{\mathrm{T}})$ is linear and angular velocity specifications of the moving frame M in Cartesian coordinates and J_i refers the Jacobian of the forward kinematics (see (123)) at the task point i. Since the Jacobian J_i is not a square matrix, a pseudo-inverse is utilized to solve (129).

The prescribed linear and angular accelerations of the moving frame M in Cartesian coordinates, $A_i = (\mathbf{a}_i^{\mathrm{T}}, \alpha_i^{\mathrm{T}})$, can be mapped to a corresponding joint angular acceleration vector $\ddot{\mathbf{q}}_i = \left(\ddot{\alpha}_i, \ddot{\beta}_i, \ddot{\gamma}_i, \ddot{\delta}_i\right)^{\mathrm{T}}$ by the time derivative of (129),

$$A_i = \dot{J}_i \dot{\mathbf{q}}_i + J_i \ddot{\mathbf{q}}_i. \tag{130}$$

Since $j_i\dot{\mathbf{q}}_i$ is known from (129), the acceleration conversion (130) can be solved with a Jacobian pseudo-inverse,

$$\ddot{\mathbf{q}}_i = \left[J_i^{\mathrm{T}} J_i\right]^{-1}\left[J_i^{\mathrm{T}}\right]\left(A_i - \dot{J}_i\dot{\mathbf{q}}_i\right). \tag{131}$$

Following [115], a set of fifth order polynomials is defined as

$$\mathbf{q}(t) = D\begin{bmatrix}1 & t & t^2 & t^3 & t^4 & t^5\end{bmatrix}^{\mathrm{T}}, \tag{132}$$

where the coefficient matrix D can be solved to generate a smooth joint trajectory between $\left(\mathbf{q}_1, \dot{\mathbf{q}}_1, \ddot{\mathbf{q}}_1\right)$ and $\left(\mathbf{q}_2, \dot{\mathbf{q}}_2, \ddot{\mathbf{q}}_2\right)$ over the time range $t_1 \le t \le t_2$.

4.5. Experimental Setup for Obtaining Elbow Constrained Hand Paths

In order to acquire actual human hand profiles with an elbow joint constraint, a point-to-point reaching experiment was designed. The identical experiment as introduced in Section 3.5 was performed with the same elbow and the wrist braces. Note that the linkage synthesis derives the kinematic specifications of contact geometries solely from the motion kinematics. Therefore, in this experiment, the motion kinematics was recorded by an optical motion capture system (Vicon, OMG Plc., UK) instead of the developed mobile MCS for its more accurate measurement. Three reflective markers were attached to each shoulder, elbow and wrist joint regions of the author as shown in Figure 45, and their

spatial positions were tracked by the Vicon system with 100 Hz sampling rate. The origin of the moving frame M was defined on the marker **A**. Its x-axis M_x was defined as **B** – **A**, the z-axis M_z was computed by (**B** – **A**) × (**C** – **A**) and the y-axis was determined by another cross product, $M_z \times M_x$.

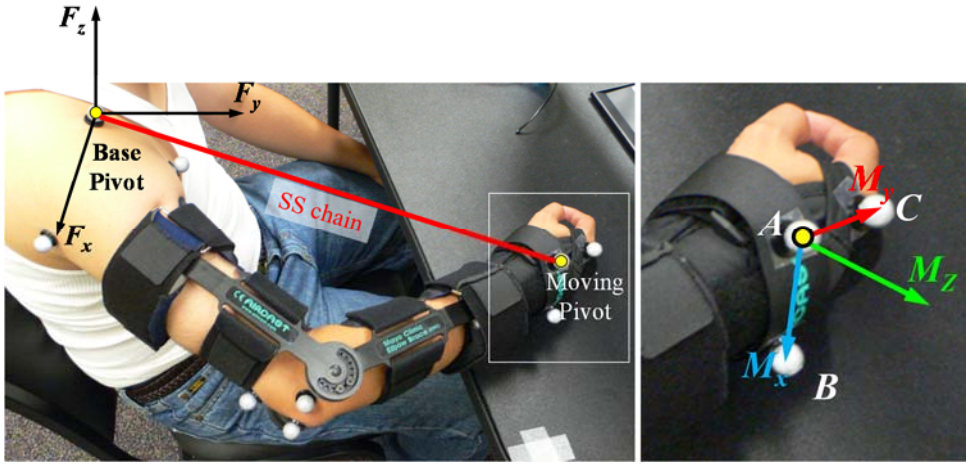

Figure 45. Attached markers on the elbow constrained arm. Three contact points of the hand are indicated as A, B and C

4.6. Comparison Between the Approximated and the Experimentally Obtained Elbow Constrained Hand Paths: A Preliminary Result

A diagonal point-to-point reaching task was selected to demonstrate the result of the approximation. From the captured motion data, contact specification of the hand in the vicinity of each task point were computed as shown in Table 13 by numerically differentiating linear positions and solving equations (126) to (128). The contact specifications at the two task positions in Cartesian space are then converted into joint

space (i.e., IJC – intrinsic joint coordinates) via (26) and (129) to (131). Finally, the joint trajectory is formulated by (132), and the hand path in Cartesian space is recovered by the forward kinematics (123).

Table 13. Task specifications captured and computed at two task points

Position Spec. (mm;rad)	$\left(d_x, d_y, d_z; \theta, \phi, \psi\right)$
Initial Location	(-47.10, 543.7, 51.89; -0.897, -0.853, 0.869)
Final Location	(210.0, 493.5, -113.5; -0.561, -0.612, 1.260)
Velocity Spec. (mm/s;rad/s)	$\left(\dot{d}_x, \dot{d}_y, \dot{d}_z; \dot{\theta}, \dot{\phi}, \dot{\psi}\right)$
Initial Location	(11.88, 0.8770, 1.589; 0.0314, -0.0326, 0.0696)
Final Location	(-5.084, 5.984, 16.60; -0.0297, -0.0280, 0.0257)
Acceleration Spec. (mm/s^2;rad/s^2)	$\left(\ddot{d}_x, \ddot{d}_y, \ddot{d}_z; \ddot{\theta}, \ddot{\phi}, \ddot{\psi}\right)$
Initial Location	(222.4, 24.25, -55.30; -0.562, -2.91, 3.63)
Final Location	(-93.72, 41.28, 9.978; -1.35, 0.380, 1.27)

The approximated hand path profile with higher order motion constraints for the selected trial is compared with the experimental data and shown in Figure 46. In Figure 46(a), two spatial curve geometries are compared in Cartesian space. The approximation result (see grey dotted line) closely follows the experimental hand path (see black continuous line) with no significant deviations. In order to take a closer look, two curves are compared in the geometry and the spatio-temporal perspectives. First, each curve is re-parameterized by one's arc length and its Cartesian coordinates are plotted over the normalized arc length (see Figure 46(b)). By the re-parameterization, we can purely compare the geometries of the two curves without any temporal effects. Next, each *x*-, *y*-, and *z*-axis component of two trajectories along the normalized time is compared (see

Figure 46(c)). As shown in those detailed figures, the proposed method closely approximates both the geometry and the spatio-temporal aspects of the actual hand path.

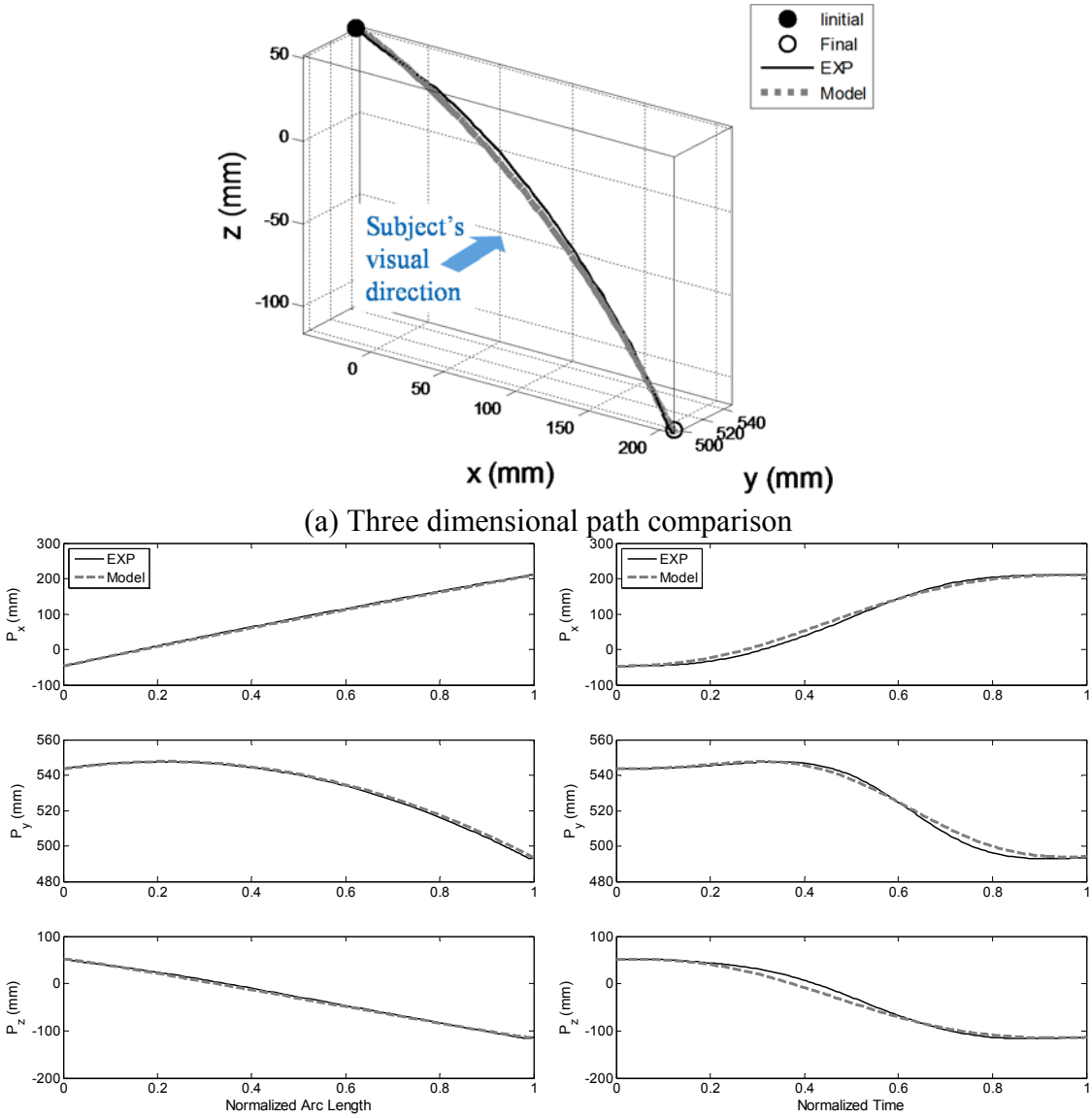

(a) Three dimensional path comparison

(b) Coordinate comparison with respect to the normalized arc length

(c) Coordinate comparison with respect to the normalized time

Figure 46. Spatial comparison of the approximated hand path with the selected experimental data

It can be noticed that deviations between the two trajectories are relatively more significant when they are compared along the normalized time than along the normalized arc length. This can be explained by different temporal characteristics reflected in their speed profiles (see Figure 47). Since the approximated model trajectory is formulated by the analytical solution of the minimum jerk model in the joint space, it shows smoother speed profile than the experimentally obtained profile. Here, it should be noted, that despite the deviations during the reaching, the approximated and the obtained hand paths overlap in the vicinity of the two positions where the higher motion constraints have been defined.

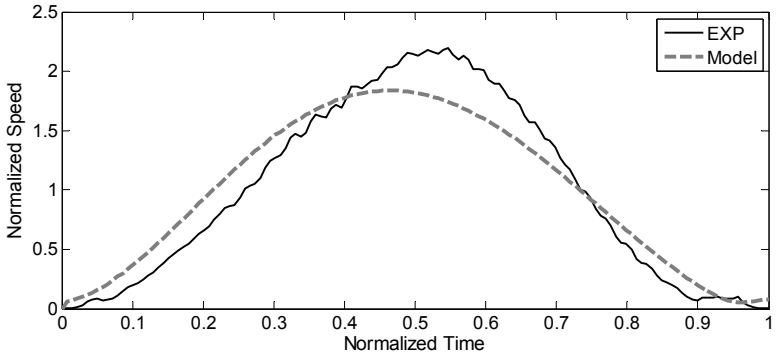

Figure 47. Temporal comparison of two curves

4.7. Conclusion

Hand path formulation in a point-to-point reaching is a highly redundant mapping problem in mathematics which is easily resolved by the CNS almost unconsciously. In order to explain such an efficient and optimal redundancy resolution scheme, it is proposed that

contact conditions at the reaching hand can be taken into account. These contact conditions are related to higher order kinematic task constraints such as velocities and accelerations. In order to validate this viewpoint, an elbow constrained reaching motion profile is approximated using recently developed kinematic synthesis techniques.

As a preliminary result, an approximation model output is generated for geometrical and spatio-temporal comparisons with a selected experimental data. From qualitative analysis, the model output closely follows the experimental data. Therefore, it can be considered that the CNS takes the hand contact conditions into account when it plans reaching profiles. It is expected that this finding can be extensively applied to approximate non-constraint arm reaching movements, which are highly patterned, by assuming that characteristics of governing rules within the CNS can be modeled as imaginary hand contact conditions.

5. FUTURE APPLICATION: TOWARDS A NOVEL MYO-PROSTHETIC ARM CONTROLLER CONCEPT

5.1. Introduction

Almost every work/motion that you perform in your daily life ends up with a combination of upper extremity actions, such as reaching, pointing and grasping. In order to open a door, for instance, an arm reaching motion is first conducted to place the end-effector (i.e. a hand) on the door knob. Then a hand grasping motion is followed to give a proper pressure to induce a firm friction on the interface between the hand and the door knob. In this grasping motion, redundant DOF (degrees-of-freedom) in the hand are controlled according to the geometric shape of contact object. After the grasping, a wrist turning motion, which rotates the end-effector orientation, and an arm extending or contracting motion are combined to complete the overall action sequence. Since all these sequential movements are well trained in the CNS and performed almost automatically, it is often forgotten that how much the life will be challenging if those basic motor functions are restricted due to any physical impairments or amputations.

In the United States, approximately 1.6 million amputees were living in 2005 which means that one in 190 Americans were living with limb amputation. Among those numbers, 38% had an amputation secondary to dysvascular diseases. The authors projected the number of amputee populations will be more than double by year 2050 to 3.6 million [166]. In a study of Dillingham *et al*., dysvascular amputations accounted for 82% of limb loss discharges and increased over the period studied [167]. According to the

2010 United States military casualty statistics report, number of 5,283, 112 and 1,112 service members lost their limbs in the Vietnam War, the Operation Enduring Freedom and the Operation Iraq Freedom, respectively [168]. These numbers and statistics emphasis that the development of technologies for improving amputee population's quality of life is important.

In this section, a novel myo-prosthetic arm control concept is introduced as a future application of findings and efforts that are made in this dissertation. In order to substitute an amputee operator's missing limb DOF, the prosthesis needs to 1) detect the operator's original motion intent and 2) generate the prosthetic DOF as close as possible to the natural human limb DOF. In this context, a control concept that utilizes the developed mobile MCS and a computational model, which can be constituted by experimental results presented in Section 3, to control a transhumeral prosthetic arm for achieving natural point-to-point reaching actions in ADL (activities of daily life).

5.2. Background

5.2.1. Control paradigms of upper limb prostheses

Mainly four different paradigms have been used or developed to control upper extremity artificial limbs. The most commonly used method is a body-powered control which is based on the mechanical control paradigm. The first body-powered transradial (i.e. below elbow amputation) prosthesis was developed by a German dentist, Peter Baliff, after the Napoleonic Wars in 1818 [169]. The device used a spring mechanism, which connected from the artificial fingers to the shoulder harness, to control the hand gripping motion

powered by trunk and shoulder girdle muscles. In 1844, utilizing the Baliff's principle, the first transhumeral (i.e. above elbow amputation) body-powered prosthesis was introduced by a Dutch sculptor, Van Peeterssen [169]. After these first kinds, body-powered prosthesis designs have been improved. However, the basic principle, controlling the desired DOFs motion via transferring residual limb DOF motions through mechanical components (e.g. springs and cables), has been kept until the recent designs (see Figure 48). The body–powered prostheses are still widely used due to its simplicities in design and control, and cost effectiveness. Also, its passive mechanisms guarantee the operator from unexpected malfunctions of active systems. Disadvantages of the device are 1) limited controllable DOF (usually hand gripping and additional elbow flexion/extension is considered for transhumeral prostheses) and 2) control performance is solely dependent on the user's training.

Figure 48. Body-powered upper limb prostheses

As a next generation technology, the first working electrically powered artificial arm was developed by Alderson with support from United States government and IBM about 1949 [169, 170]. In 1957, USSR Academy of Sciences and the Central Prosthetics Research Institute at Moscow had begun researches on myoelectric control [171] and its

first product, a transradial electric hand controlled by EMG, was announced in 1958 [170, 172]. Although the rights to manufacture this product was sold to groups in Canada and United Kingdom [170, 173], it seems that commercializing attempts were not widely accepted at that time [170]. After then, Otto Bock in Austria developed a first commercialized myoelectric hand Model Z1 based on the Russian design. After that, a modified version Model Z6 was developed by Otto Bock in Germany in 1967 as the first system for clinical use [171]. In that era, those devices were innovative enough to be called as *"thought-controlled prostheses"* as mentioned in [170] due to adoption of a biological command signal (i.e. EMG) to represent the user's intention. In the earlier stage, the acquired EMG signal was simply utilized as a binary action signal (i.e. on or off) for an active prosthetic DOF. Later, the proportionality of EMG to the actual muscle force was implemented in the control algorithms for more natural and finer control of force and speed. Figure 49 shows the Otto Bock's recent myoelectic hand and arm respectively. So far, only basic DOF, which are far insufficient for the desired natural human limb motion, are implemented in these off-the-shelf myoelectric prostheses due to limitations that will be discussed later in Section 5.3.

(a) MyoHand VariPlus Speed

(b) DynamicArm

Figure 49. Recent myoelectric prostheses developed by Otto Bock Inc.

In order to overcome practical limitations of myo-prostheses, an advanced control paradigm that incorporates surgical methodology was introduced to realize natural and simultaneous multi-DOF control [25, 174-176]. Even after the amputation, neural commands from the CNS are transmitted to the peripheral nerve ends when the amputee subject tries to move his/her phantom limb. Thus, by connecting these nerve ends to the prosthetic controller, the prosthesis can be controlled by the subject's thoughts. However, the magnitude of those neural signals at the nerve ends is insufficient to capture directly from electrodes. Kuiken *et al*., [25, 174, 176] resolved this problem by the targeted muscle reinnervation (TMR) surgery. In the TMR, the desired peripheral nerve ends are transferred to the chest muscle, and this chest muscle is separated into several electrically isolated substrates. As a result, when the subject intents to control his/her missing limb DOF, the neural command is projected to one of the isolated substrates in the chest muscle. Then the contraction of the targeted substrate muscle generates an EMG signal that is large enough to be measured. As each substrate is connected to each nerve ending, multiple missing limb DOF are mapped to corresponding channels of EMG. In other words, the chest muscle becomes a biological amplifier of the missing limb's peripheral nerve endings. Figure 50(a) and (b) show schematic plot of the TMR control and human subjects in clinical studies after successful TMR, respectively. Though this technology opened a new era of prostheses control, it has intrinsic disadvantages for wide usage such as 1) high costs, 2) invasive surgery, 3) risky possible side-effects (e.g. phantom limb pain and permanent limb paralysis [175]), 4) real estate problem (i.e., spatial limitations of the

EMG electrode implantation in the chest muscle), and 5) long period of recovery and rehabilitation.

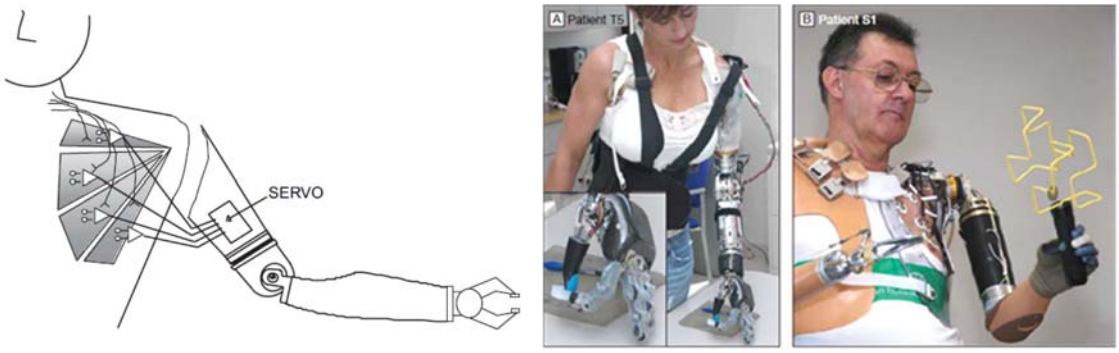

(a) Schematic plot of TMR control [174] **(b) Subjects after TMR surgery [25]**

Figure 50. Targeted muscle reinnervation (TMR) control paradigm

The concept of thought-controlled artificial limbs has continued to the next level technology, brain machine interface (BMI). In this control paradigm, the user's motion intention is captured directly from the motor cortex area of the brain through micro electrode arrays and transferred to the prosthesis controller. Georgopoulos *et al.*, [177] discovered an interesting discharge phenomenon of motor cortex cells from the monkey's two-dimensional arm movement. Over 74% of motor cortex cells vary their frequency of discharge in an orderly fashion with the direction of arm movement. In other words, by interpreting the preferred direction of each motor cortex cell, user's motion intention can be captured as a desired hand direction. Wessberg *et al*., [178] implanted microwire arrays in two monkey's multiple cortical areas (i.e. premotor, primary motor and posterior parietal cortical areas) and predicted the monkey's motion intention in both one–

dimensional and three–dimensional tasks through machine learning algorithms. The prediction method ran in real–time so that a robotic manipulator could be controlled according to the predicted direction as the monkey thought. In their experimental study, Velliste *et al*., [179] enabled a proportional control of the BMI. As a result, a monkey could control a prosthetic arm by her thought to feed herself (see Figure 51(a)).

Despite its advanced technology, the BMI control paradigm has significant problems for its practical usage:

1) Like the TMR control method, an invasive brain surgery should be incorporated which induces similar disadvantages of the TMR method,
2) Advanced brain signal interpretation technologies are required to capture the operator's intent in robust and real-time manners, and
3) For the current state of technology, the microwire electrode array implant cannot last longer than a year.

Especially for 3), the BMI technology may ask multiple times of brain surgeries to replace the sensor arrays for the maintenance of the prosthetic limb. From their survey on advanced neuro-technologies, Kipke, *et al*., [180] mentioned that:

"*However, there is a large degree of variability and unpredictability in chronic performance that results from an incomplete understanding of the failure (and success) modes of implantable microscale devices. At present, the state of the art for implantable arrays is that recording quality typically degrades and uniformly fails over time (life-times ranging from several weeks to several months).*

Also, the statistical results of Rosenow, *et al*., [181] showed that the required revision rate of implanted spinal cord stimulation device was 46% of total 577 procedures of 289 patients. Even though the spinal cord is an active moving part, we have to note that the spinal cord device itself has much larger dimensions which can stand for larger stresses and strains. Since inside the human body is a harsh environment for the elctromechanical devices, further studies are required for the enhanced reliability of the microwire electrode arrays.

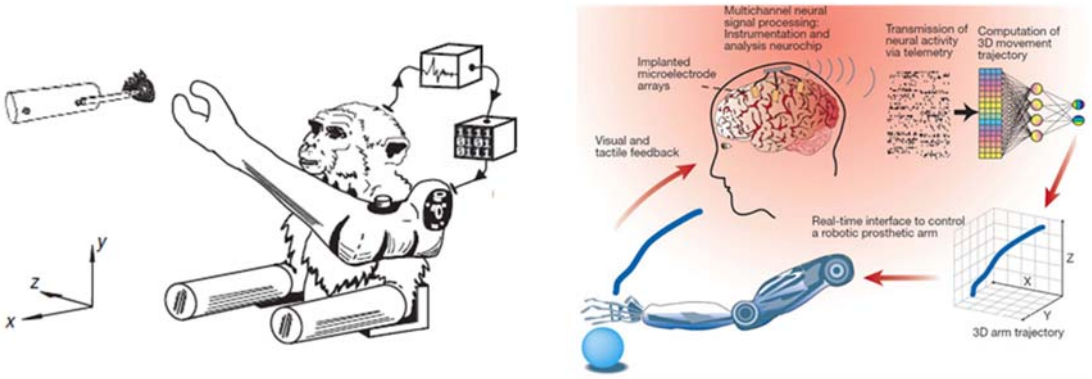

(a) A monkey feed herself via BMI prosthesis [179]

(b) A schematic plot of the BMI prosthetic control [182]

Figure 51. Brain Machine Interface (BMI) control paradigm

5.2.2. Previous studies on the myo-prosthesis control

Various EMG prosthesis control scheme have been studied to achieve 1) multi-DOF control and 2) real-time control. In general, feature extraction methods or pattern recognition algorithms have been adopted to discriminate (i.e. classify) patterned hand motions (i.e. gestures) or to extract multiple proportional command signals.

Ajiboye and Weir [183] applied a heuristic fuzzy logic to extract multiple independent features to map with each prosthetic DOF. Similar solutions were introduced by Chan and Englehart [184], adopting Hidden Markov Model. Chan *et al*., [185] proposed a combination of fuzzy and artificial neural network algorithms. Ito *et al*., [186] utilized three different artificial neural network modules to represent classified hand DOF motions. Kato *et al*., [187] suggested an online learning mechanism to adapt the mapping between EMG signals and desired motions. Soares *et al*. [188] applied association of autoregressive models and an artificial neural network to extract independent command signals for elbow flexion/extension and wrist pronation/supination motions. Instead of connecting features to each joint DOF, some research groups mapped features to pre-defined possible hand gestures (e.g. power grasp, hook grasp, cylindrical grasp and centralized grip) [189-191].

The most inspiring control scheme for this dissertation was introduced by Kaliki *et al*., [192, 193]. In their works, EMG signals are not adopted to drive the prosthesis. Instead, a neural network is designed to model a synergistic kinematics of the shoulder and the elbow DOF during arm reaching movements. By approximating the human motor behavior in reaching, the elbow DOF can be driven to achieve a harmony with captured shoulder DOF motions. The proposed neural network has a similar concept as of a computational model on human arm reaching that will be introduced in Section 5.4.

5.3. Problem Statement and Control Objective

The myo-prosthesis control scheme is limited by the driving signal's intrinsic nature of irregularities and nonlinearities. For instance, the EMG pattern can be changed depending on the posture though the signal is acquired at the same spot. The variance of skin impedance due to humidity change can also affect the signal. In addition, unlike needle type electrode, surface electrode signal can be affected by multiple muscles around the measuring location (i.e. muscle crosstalk).

The ultimate goal of the proposed myo-prosthesis control concept is on the simultaneous multi-DOF motion control in real-time for 3D reaching movements of a transhumeral prosthetic arm according to the user's motion intent. For this purpose, three main objectives are set: 1) standardized quantification of the driving signal, 2) capturing motion intent, and 3) generate reference motion according to the natural human limb motion profiles. In this context, the developed mobile MCS and experimental results can be adopted as plausible tools for above objectives.

5.4. Idea Representation

Figure 52 represents the schematic diagram of the proposed control concept. First, the operator's motion intent needs to be captured in a non-invasive way. For this purpose, an IMU integrated binocular gaze tracker is utilized. As the hand kinematics gets the greatest attention of the CNS during a reaching action [89], the location of a targeting object can be defined as the operator's motion intent. The eye tracker (see Figure 52(c)) captures the gaze direction to find the position of the operator's greatest attention (i.e., targeting object)

in a head centered coordinate system (see Figure 52(a)). By capturing gazes of both eyes (i.e., binocular), not just the direction but also the distance to the reaching target can be determined by the angle of focus [194]. The pinpointed targeting position in the head coordinates is converted into the prosthesis coordinates (see Figure 52(b)) by putting the head IMU readings into the rigid body orientation estimation algorithm introduced in 2.4.1. Consequently, the targeting object in the subject's visual field can be mapped to the desired final hand position in the prosthesis coordinate system. The captured motion intent is confirmed by the brainwave signal recorded from an EEG (electroencephalography) device (see Figure 52(d)). Once the motion intention detector (see Figure 52(e)) outputs the final hand position, a computational model on human arm reaching (see Figure 52(f)) generates the reference motion profile in accordance to the modeled human motor behavior. In other words, desired motion profile is planned in joint space to fill out the gap between the captured final hand position and the initial posture. From this reference motion, the residual limb kinematics that is acquired from the attached mobile MCS is subtracted to specify the reference motion of the prosthetic limb DOF. The prosthesis controller (see Figure 52(h)) finalizes the control command to track the desired reference motion. Here, the driving signal (i.e., multi -channels of the surface EMG) is utilized as a proportional control command. Myoprocessors integrated in the developed mobile MCS quantify the EMG signal in a standardized way as a muscular force value. This enables the prosthesis to acquire a reliable proportional control command in accordance to the operator's motion intent.

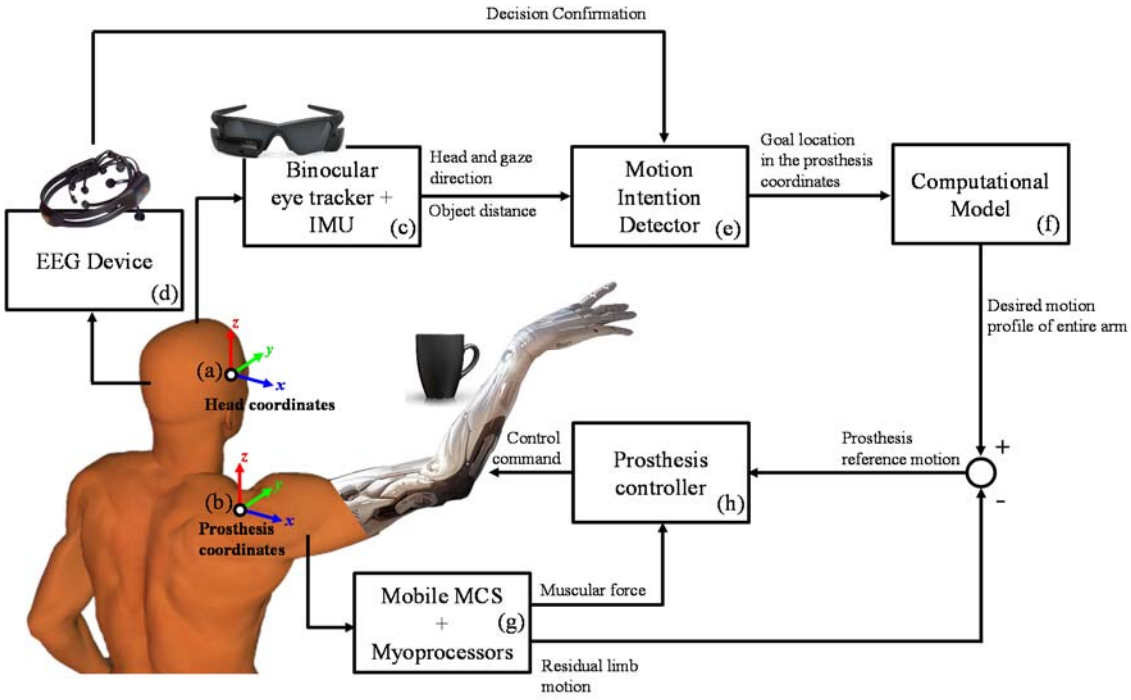

Figure 52. Schematic plot of the proposed control concept of a myo-prosthetic arm

6. CONCLUSIONS

Throughout the dissertation, efforts have made to resolve three main challenges in the advanced HIR control. A mobile motion capture system (MCS) enhanced by myoprocessors is introduced as the first main contribution. By adopting the inertial navigation system of MEMS (micro-electromechanical system) IMU (inertial measurement unit) sensors, a source-less and untethered MCS is developed that can capture the human arm motion of reaching in ADL (activities of daily life). For a robust motion capture in a model-free manner, a time varying complementary filter (TVCF) that is adapting its cut-off frequency according to the motion dynamics is adopted. Furthermore, the dynamics of captured motions is computed by an integration of multi-channel surface EMG (electromyography) sensors and myoproessors. By a combination of the EMG processing module, the varying moment arm module and the Hill-based muscle model, the recorded EMG signal is quantified in a standardized way to overcome its innate characteristics of irregularity and nonlinearity. The developed mobile MCS was utilized as an experimental apparatus in the experimental observation of the human arm with and without a reduced mobility. In future applications, it is expected that the proposed MCS can be a plausible tool for reliable motion intent detection for its standardized way of quantification on one of the most frequently used driving signal of the HIR, EMG.

Once the operator's motion intent is detected, the HIR needs to control its motion to either assist or resist the human motion according to its specific purpose. For the design of such high-level control architecture of the HIR, which can determine the direction and

the magnitude of robotic forces/motions, it is better for the HIR to understand the motor coordination strategies and/or motor behaviors of the human operator. For this purpose, a computational model on reaching is required. In this dissertation, an experimental study is conducted to identify governing rules within the CNS (central nervous system) by extracting invariant motion features of captured motion data with and without an elbow joint constraint. For a designed experiment, acquired motion data from the developed mobile MCS is compared with hypothesized models of each motion components, hand path geometry, hand speed profile and arm postural configuration. From observations on quantitative and statistical analyses, it was found that the hand path geometry, temporal control and arm posture selection are generally governed by the LKE (least kinematic effort) principle, smoothness maximization and the kinetic torque minimization, respectively.

Though a computational model can be developed based on the experimental findings, the computational cost is a critical criterion especially for real-time applications such as the HIR control. For instance, a real-time loop cannot afford expensive computational efforts of multiple optimization processes to get the best approximation result. In this context, theories in robotics can be applied to make a reasonable approximation with relatively affordable computational cost. In this dissertation, a higher order kinematic synthesis of mechanical linkage systems is adopted to approximate natural human hand profiles. From geometries of hand contact objects, directional constraints on the velocity and the acceleration vector of the hand at the initial and the final location in a reaching can be derived. In this manner, a natural hand trajectory connecting the two task

points was defined by satisfying contact conditions in the vicinity of the task points, simultaneously. By comparing the model output with an example hand profile data, its good approximation performance was verified.

Finally, a novel control concept of a myo-prosthetic arm is proposed as an application of all findings and efforts made in this dissertation. In the proposed control concept, the human motion intent is captured as the position of a targeting object by using a binocular gaze tracker and an EEG (electroencephalography) device. From the pin-pointed final hand location, a computational model on human arm reaching generates a reference motion for the entire arm. By subtracting the residual limb kinematics captured from the developed mobile MCS, a desired motion of prosthetic DOF is determined.

REFERENCES

[1] T. Nef, M. Guidali, and R. Riener, "ARMin III-Arm Therapy Exoskeleton with an Ergonomic Shoulder Actuation," *Applied Bionics and Biomechanics,* vol. 6, pp. 127-142, 2009.

[2] K. Kong, J. Bae, and M. Tomizuka, "Control of rotary series elastic actuator for ideal force-mode actuation in human–robot interaction applications," *Mechatronics, IEEE/ASME Transactions on,* vol. 14, pp. 105-118, 2009.

[3] F. Amirabdollahian, R. Loureiro, E. Gradwell, C. Collin, W. Harwin, and G. Johnson, "Multivariate analysis of the Fugl-Meyer outcome measures assessing the effectiveness of GENTLE/S robot-mediated stroke therapy," *Journal of NeuroEngineering and Rehabilitation,* vol. 4, p. 4, 2007.

[4] R. Loureiro, F. Amirabdollahian, M. Topping, B. Driessen, and W. Harwin, "Upper limb robot mediated stroke therapy—GENTLE/s approach," *Autonomous Robots,* vol. 15, pp. 35-51, 2003.

[5] N. Hogan, H. I. Krebs, A. Sharon, and J. Charnnarong, "Interactive robotic therapist," ed: Google Patents, 1995.

[6] M. L. Aisen, H. I. Krebs, N. Hogan, F. McDowell, and B. T. Volpe, "The effect of robot-assisted therapy and rehabilitative training on motor recovery following stroke," *Archives of Neurology,* vol. 54, p. 443, 1997.

[7] S. E. Fasoli, H. I. Krebs, J. Stein, W. R. Frontera, and N. Hogan, "Effects of robotic therapy on motor impairment and recovery in chronic stroke," *Archives of physical medicine and rehabilitation,* vol. 84, pp. 477-482, 2003.

[8] B. Volpe, H. Krebs, N. Hogan, L. Edelstein, C. Diels, and M. Aisen, "A novel approach to stroke rehabilitation Robot-aided sensorimotor stimulation," *Neurology,* vol. 54, pp. 1938-1944, 2000.

[9] B. T. Volpe, M. Ferraro, H. I. Krebs, and N. Hogan, "Robotics in the rehabilitation treatment of patients with stroke," *Current atherosclerosis reports,* vol. 4, pp. 270-276, 2002.

[10] I. M. Technologies. (December 2013). *Interactive Motion Technologies*. Available: http://interactive-motion.com/

[11] B. R. Brewer, S. K. McDowell, and L. C. Worthen-Chaudhari, "Poststroke upper extremity rehabilitation: a review of robotic systems and clinical results," *Topics in stroke rehabilitation,* vol. 14, pp. 22-44, 2007.

[12] H. S. Lo and S. Q. Xie, "Exoskeleton robots for upper-limb rehabilitation: State of the art and future prospects," *Medical engineering & physics,* 2011.

[13] R. J. Sanchez, J. Liu, S. Rao, P. Shah, R. Smith, T. Rahman*, et al.*, "Automating arm movement training following severe stroke: functional exercises with quantitative feedback in a gravity-reduced environment," *Neural Systems and Rehabilitation Engineering, IEEE Transactions on,* vol. 14, pp. 378-389, 2006.

[14] M. Guidali, A. Duschau-Wicke, S. Broggi, V. Klamroth-Marganska, T. Nef, and R. Riener, "A robotic system to train activities of daily living in a virtual

environment," *Medical and Biological Engineering and Computing,* vol. 49, pp. 1213-1223, 2011.

[15] J. C. Perry, J. Rosen, and S. Burns, "Upper-limb powered exoskeleton design," *Mechatronics, IEEE/ASME Transactions on,* vol. 12, pp. 408-417, 2007.

[16] E. Cavallaro, J. Rosen, J. C. Perry, S. Burns, and B. Hannaford, "Hill-based model as a myoprocessor for a neural controlled powered exoskeleton arm-parameters optimization," in *Robotics and Automation, 2005. ICRA 2005. Proceedings of the 2005 IEEE International Conference on*, 2005, pp. 4514-4519.

[17] E. E. Cavallaro, J. Rosen, J. C. Perry, and S. Burns, "Real-time myoprocessors for a neural controlled powered exoskeleton arm," *Biomedical Engineering, IEEE Transactions on,* vol. 53, pp. 2387-2396, 2006.

[18] S. Balasubramanian, R. Wei, M. Perez, B. Shepard, E. Koeneman, J. Koeneman*, et al.*, "RUPERT: An exoskeleton robot for assisting rehabilitation of arm functions," in *Virtual Rehabilitation, 2008*, 2008, pp. 163-167.

[19] C. Carignan, J. Tang, and S. Roderick, "Development of an exoskeleton haptic interface for virtual task training," in *Intelligent Robots and Systems, 2009. IROS 2009. IEEE/RSJ International Conference on*, 2009, pp. 3697-3702.

[20] S. J. Ball, I. E. Brown, and S. H. Scott, "MEDARM: a rehabilitation robot with 5DOF at the shoulder complex," in *Advanced intelligent mechatronics, 2007 IEEE/ASME international conference on*, 2007, pp. 1-6.

[21] Y. Ren, H. S. Park, and L. Q. Zhang, "Developing a whole-arm exoskeleton robot with hand opening and closing mechanism for upper limb stroke rehabilitation,"

in *Rehabilitation Robotics, 2009. ICORR 2009. IEEE International Conference on*, 2009, pp. 761-765.

[22] Myomo. (December 2013). *Myomo, Inc.* Available: http://www.myomo.com/

[23] Hokoma. (December 2013). *Hokoma*. Available: www.hocoma.com

[24] S. Adee. (2008) Dean Kamen's "Luke Arm" Prosthesis Readies for Clinical Trials. *IEEE Spectrum*.

[25] T. A. Kuiken, G. Li, B. A. Lock, R. D. Lipschutz, L. A. Miller, K. A. Stubblefield, *et al.*, "Targeted Muscle Reinnervation for Real-time Myoelectric Control of Multifunction Artificial Arms," *Journal of American Medical Association,* vol. 301, pp. 619-628, 2009.

[26] J. H. U. A. P. Laboratory. (June 2014). *The Official Press Release on Modular Prosthetic Limb System*. Available: http://www.jhuapl.edu/newscenter/pressreleases/2010/100714.asp

[27] D. Novak and R. Riener, "Enhancing patient freedom in rehabilitation robotics using gaze-based intention detection," in *Rehabilitation Robotics (ICORR), 2013 IEEE International Conference on*, 2013, pp. 1-6.

[28] C. Loconsole, F. Banno, A. Frisoli, and M. Bergamasco, "A new Kinect-based guidance mode for upper limb robot-aided neurorehabilitation," in *Intelligent Robots and Systems (IROS), 2012 IEEE/RSJ International Conference on*, 2012, pp. 1037-1042.

[29] W. Huo, J. Huang, Y. Wang, and J. Wu, "Control of a rehabilitation robotic exoskeleton based on intentional reaching direction," in *Micro-NanoMechatronics and Human Science (MHS), 2010 International Symposium on*, 2010, pp. 357-362.

[30] R. Gopura and K. Kiguchi, "Electromyography (EMG)-signal based fuzzy-neuro control of a 3 degrees of freedom (3DOF) exoskeleton robot for human upper-limb motion assist," *Journal of the National Science Foundation of Sri Lanka,* vol. 37, pp. 241-248, 2009.

[31] M. H. Lee, J. Son, J. Y. Kim, and Y. H. Kim, "Development and Assessment of an EMG-Based Exoskeleton System," in *6th World Congress of Biomechanics (WCB 2010). August 1-6, 2010 Singapore*. vol. 31, C. T. Lim and J. C. H. Goh, Eds., ed: Springer Berlin Heidelberg, 2010, pp. 648-650.

[32] A. Frisoli, C. Loconsole, D. Leonardis, F. Banno, M. Barsotti, C. Chisari*, et al.*, "A New Gaze-BCI-Driven Control of an Upper Limb Exoskeleton for Rehabilitation in Real-World Tasks," *Systems, Man, and Cybernetics, Part C: Applications and Reviews, IEEE Transactions on,* vol. 42, pp. 1169-1179, 2012.

[33] E. A. Clancy and N. Hogan, "Relating Agonist-Antagonist Electromyograms to Joint to Torque During Isometric, Quasi-isotonic, Nonfatiguing Contractions," *IEEE Transactions on Biomedical Engineering,* vol. 44, pp. 1024-1028, 1997.

[34] H. S. Lo and S. Q. Xie, "Exoskeleton robots for upper-limb rehabilitation: State of the art and future prospects," *Medical engineering & physics,* vol. 34, pp. 261-268, 2012.

[35] J. S. Albus, "A New Approach to Manipulator Control: The Cerebellar Model Articulation Controller (CMAC)," *Journal of Dynamic Systems, Measurement, and Control,* vol. 97, pp. 220-227, 1975.

[36] R. L. Smith, "Intelligent motion control with an artificial cerebellum," ResearchSpace@ Auckland, 1998.

[37] P.-G. Jung, S. Oh, G. Lim, and K. Kong, "A Mobile Motion Capture System Based on Inertial Sensors and Smart Shoes," *Journal of Dynamic Systems, Measurement, and Control,* vol. 136, p. 011002, 2014.

[38] E. A. Clancy and N. Hogan, "Relating agonist-antagonist electromyograms to joint torque during isometric, quasi-isotonic, nonfatiguing contractions," *Biomedical Engineering, IEEE Transactions on,* vol. 44, pp. 1024-1028, 1997.

[39] S. Lee and Y. Sankai, "Power assist control for walking aid with HAL-3 based on EMG and impedance adjustment around knee joint," in *Intelligent Robots and Systems, 2002. IEEE/RSJ International Conference on*, 2002, pp. 1499-1504.

[40] K. Kiguchi, M. H. Rahman, M. Sasaki, and K. Teramoto, "Development of a 3DOF mobile exoskeleton robot for human upper-limb motion assist," *Robotics and Autonomous Systems,* vol. 56, pp. 678-691, 2008.

[41] J. M. Winters, "Hill-based muscle models: a systems engineering perspective," in *Multiple muscle systems*, ed: Springer, 1990, pp. 69-93.

[42] S. Research. (May 2014). *Shimmer Research*. Available: www.shimmersensing.com

[43] G. Grenon, P. E. An, S. M. Smith, and A. J. Healey, "Enhancement of the inertial navigation system for the morpheus autonomous underwater vehicles," *Oceanic Engineering, IEEE Journal of,* vol. 26, pp. 548-560, 2001.

[44] W. Zhang, M. Ghogho, and B. Yuan, "Mathematical model and matlab simulation of strapdown inertial navigation system," *Modelling and Simulation in Engineering,* vol. 2012, p. 1, 2012.

[45] A. M. Sabatini, "Quaternion-based extended Kalman filter for determining orientation by inertial and magnetic sensing," *Biomedical Engineering, IEEE Transactions on,* vol. 53, pp. 1346-1356, 2006.

[46] X. Yun and E. R. Bachmann, "Design, implementation, and experimental results of a quaternion-based Kalman filter for human body motion tracking," *Robotics, IEEE Transactions on,* vol. 22, pp. 1216-1227, 2006.

[47] M. D. Shuster and S. D. Oh, "Three-axis attitude determination from vector observations," *Journal of Guidance, Control, and Dynamics,* vol. 4, pp. 70-77, 1981.

[48] H. J. Luinge and P. H. Veltink, "Inclination measurement of human movement using a 3-D accelerometer with autocalibration," *Neural Systems and Rehabilitation Engineering, IEEE Transactions on,* vol. 12, pp. 112-121, 2004.

[49] H. Luinge and P. H. Veltink, "Measuring orientation of human body segments using miniature gyroscopes and accelerometers," *Medical and Biological Engineering and computing,* vol. 43, pp. 273-282, 2005.

[50] D. Roetenberg, H. J. Luinge, C. T. Baten, and P. H. Veltink, "Compensation of magnetic disturbances improves inertial and magnetic sensing of human body segment orientation," *Neural Systems and Rehabilitation Engineering, IEEE Transactions on,* vol. 13, pp. 395-405, 2005.

[51] H. M. Schepers, D. Roetenberg, and P. H. Veltink, "Ambulatory human motion tracking by fusion of inertial and magnetic sensing with adaptive actuation," *Medical & biological engineering & computing,* vol. 48, pp. 27-37, 2010.

[52] D. Roetenberg, H. Luinge, and P. Slycke, "Xsens MVN: full 6DOF human motion tracking using miniature inertial sensors," *Xsens Motion Technologies BV, Tech. Rep,* 2009.

[53] A. Young, "Comparison of orientation filter algorithms for realtime wireless inertial posture tracking," in *Wearable and Implantable Body Sensor Networks, 2009. BSN 2009. Sixth International Workshop on*, 2009, pp. 59-64.

[54] J. Calusdian, X. Yun, and E. Bachmann, "Adaptive-gain complementary filter of inertial and magnetic data for orientation estimation," in *Robotics and Automation (ICRA), 2011 IEEE International Conference on*, 2011, pp. 1916-1922.

[55] E. Chang-Siu, M. Tomizuka, and K. Kong, "Time-varying complementary filtering for attitude estimation," in *Intelligent Robots and Systems (IROS), 2011 IEEE/RSJ International Conference on*, 2011, pp. 2474-2480.

[56] Y. Xiaoping, E. R. Bachmann, and R. B. McGhee, "A simplified quaternion-based algorithm for orientation estimation from earth gravity and magnetic field

measurements," *Instrumentation and Measurement, IEEE Transactions on,* vol. 57, pp. 638-650, 2008.

[57] G. Wahba, "A least squares estimate of satellite attitude," *SIAM review,* vol. 7, pp. 409-409, 1965.

[58] M. Anderton, M. N. Ede, and E. Holt, "Normal range of motion of the shoulder: an imprecise benchmark," *Journal of Bone & Joint Surgery, British Volume,* vol. 94, pp. 127-127, 2012.

[59] T. T. Manson, H. J. Pfaeffle, J. H. Herndon, M. M. Tomaino, and K. J. Fischer, "Forearm rotation alters interosseous ligament strain distribution," *The Journal of hand surgery,* vol. 25, pp. 1058-1063, 2000.

[60] J. B. Kuipers, *Quaternions and rotation sequences* vol. 66: Princeton university press Princeton, 1999.

[61] R. Challis and R. Kitney, "The design of digital filters for biomedical signal processing Part 3: The design of Butterworth and Chebychev filters," *Journal of biomedical engineering,* vol. 5, pp. 91-102, 1983.

[62] B. A. Garner and M. G. Pandy, "A kinematic model of the upper limb based on the visible human project (vhp) image dataset," *Computer methods in biomechanics and biomedical engineering,* vol. 2, pp. 107-124, 1999.

[63] D. A. Winter, *Biomechanics and Motor Control of Human Movement*, 4 ed. New Jersey: John Wiley & Sons Inc., 2009.

[64] A. Biess, D. G. Liebermann, and T. Flash, "A Computational Model for Redundant Human Three-Dimensional Pointing Movements: Integration of Independent

Spatial and Temporal Motor Plans Simplifies Movement Dynamics," *The Journal of Neuroscience,* vol. 27, pp. 13045-13064, 2007.

[65] X. Wang, M. Maurin, F. Mazet, N. D. C. Maia, K. Voinot, J. P. Verriest*, et al.*, "Three-dimensional modelling of the motion range of axial rotation of the upper arm," *Journal of biomechanics,* vol. 31, pp. 899-908, 1998.

[66] D. Magermans, E. Chadwick, H. Veeger, and F. Van Der Helm, "Requirements for upper extremity motions during activities of daily living," *Clinical Biomechanics,* vol. 20, pp. 591-599, 2005.

[67] L. Ricci, D. Formica, L. Sparaci, F. R. Lasorsa, F. Taffoni, E. Tamilia*, et al.*, "A New Calibration Methodology for Thorax and Upper Limbs Motion Capture in Children Using Magneto and Inertial Sensors," *Sensors,* vol. 14, pp. 1057-1072, 2014.

[68] A. Hill, "The heat of shortening and the dynamic constants of muscle," *Proceedings of the Royal Society of London. Series B, Biological Sciences,* vol. 126, pp. 136-195, 1938.

[69] M. Hayashibe and D. Guiraud, "Voluntary EMG-to-force estimation with a multi-scale physiological muscle model," *Biomedical engineering online,* vol. 12, p. 86, 2013.

[70] B. Freriks and H. Hermens, *European recommendations for surface electromyography: results of the SENIAM project*: Roessingh Research and Development, 2000.

[71] T. S. Buchanan, D. G. Lloyd, K. Manal, and T. F. Besier, "Neuromusculoskeletal modeling: estimation of muscle forces and joint moments and movements from measurements of neural command," *Journal of applied biomechanics,* vol. 20, p. 367, 2004.

[72] D. G. Lloyd and T. F. Besier, "An EMG-driven musculoskeletal model to estimate muscle forces and knee joint moments in vivo," *Journal of biomechanics,* vol. 36, pp. 765-776, 2003.

[73] A. Perotto and E. F. Delagi, *Anatomical guide for the electromyographer: the limbs and trunk*: Charles C Thomas Publisher, 2005.

[74] W. M. Murray, S. L. Delp, and T. S. Buchanan, "Variation of muscle moment arms with elbow and forearm position," *Journal of biomechanics,* vol. 28, pp. 513-525, 1995.

[75] J. C. Otis, C.-C. Jiang, T. L. Wickiewicz, M. Peterson, R. F. Warren, and T. J. Santner, "Changes in the moment arms of the rotator cuff and deltoid muscles with abduction and rotation," *The Journal of Bone & Joint Surgery,* vol. 76, pp. 667-676, 1994.

[76] P. Pigeon, L. H. Yahia, and A. G. Feldman, "Moment arms and lengths of human upper limb muscles as functions of joint angles," *Journal of Biomechanics,* vol. 29, pp. 1365-1370, 1996.

[77] S. S. Blemker and S. L. Delp, "Three-dimensional representation of complex muscle architectures and geometries," *Annals of biomedical engineering,* vol. 33, pp. 661-673, 2005.

[78] B. A. Garner and M. G. Pandy, "Musculoskeletal model of the upper limb based on the visible human male dataset," *Computer methods in biomechanics and biomedical engineering,* vol. 4, pp. 93-126, 2001.

[79] B. A. Garner and M. Pandy, "The obstacle-set method for representing muscle paths in musculoskeletal models," *Computer methods in biomechanics and biomedical engineering,* vol. 3, pp. 1-30, 2000.

[80] A. Seireg and R. Arvikar, "A mathematical model for evaluation of forces in lower extremeties of the musculo-skeletal system," *Journal of biomechanics,* vol. 6, pp. 313-326, 1973.

[81] J. M. Winters and L. Stark, "Analysis of fundamental human movement patterns through the use of in-depth antagonistic muscle models," *Biomedical Engineering, IEEE Transactions on,* pp. 826-839, 1985.

[82] R. P. Brent, *Algorithms for minimization without derivatives*: Courier Dover Publications, 2013.

[83] J. M. Winters and L. Stark, "Estimated mechanical properties of synergistic muscles involved in movements of a variety of human joints," *Journal of biomechanics,* vol. 21, pp. 1027-1041, 1988.

[84] R. D. Crowninshield and R. A. Brand, "A physiologically based criterion of muscle force prediction in locomotion," *Journal of biomechanics,* vol. 14, pp. 793-801, 1981.

[85] P. Binding, A. Jinha, and W. Herzog, "Analytic analysis of the force sharing among synergistic muscles in one-and two-degree-of-freedom models," *Journal of biomechanics,* vol. 33, pp. 1423-1432, 2000.

[86] N. A. Bernstein, *The Co-ordination and Regaulation of Movements*. Oxford: Pergamon Press, 1967.

[87] H. Moon, N. P. Robson, R. Langari, and J. J. Buchanan, "Experimental Observations on the Central Nervous System's Governing Strategies on the Arm Reaching with Reduced Mobility," in *ASME International Mechanical Engineering Congress and Exposition (IMECE)* Houston, Texas, USA, 2012.

[88] B. Siciliano and O. Khatib, *Springer handbook of robotics*: Springer, 2008.

[89] V. B. Brooks, *The Neural Basis of Motor Control*. New York: Oxford University Press, 1986.

[90] M. D. K. Breteler and R. G. J. Meulenbroek, "Modeling 3D Object Manipulation: Synchronous Single-Axis Joint Rotations?," *Experimental Brain Research,* vol. 168, pp. 395-409, 2006.

[91] A. Roby-Brami, A. Feydy, M. Combeaud, E. Biryukova, B. Bussel, and M. Levin, "Motor compensation and recovery for reaching in stroke patients," *Acta neurologica scandinavica,* vol. 107, pp. 369-381, 2003.

[92] D. Sha, J. Patton, and F. A. Mussa-Ivaldi, "Minimum Jerk Reaching Movements of Human Arm with Mechanical Constraints at Endpoint," *International Journal of Computers, Systems, and Signals,* vol. 7, pp. 41-50, 2006.

[93] D. G. Liebermann, T. Krasovsky, and S. Berman, "Planning Maximally Smooth Hand Movements Constrained to Nonplanar Workspace," *Journal of Motor Behavior,* vol. 40, pp. 516-531, 2008.

[94] L. E. Brown, D. A. Rosenbaum, and R. L. Sainburg, "Limb Position Drift: Implication for Control of Posture and Movement," *Journal of Neurophysiology,* vol. 90, pp. 3105-3118, 2003.

[95] M. Kawato, "Feedback-error-learning neural network for supervised motor learning," *Advanced neural computers,* vol. 6, pp. 365-372, 1990.

[96] M. Desmurget and S. Grafton, "Forward modeling allows feedback control for fast reaching movements," *Trends in cognitive sciences,* vol. 4, pp. 423-431, 2000.

[97] N. Hogan, "Planning and Execution of Multijoint Movements," *Cannadian Journal of Physiology and Pharmacology,* vol. 66, pp. 508-517, 1988.

[98] P. Morasso, "Spatial Control of Arm Movements," *Experimental Brain Research,* vol. 42, pp. 223-227, 1981.

[99] J. F. Soechting and F. Lacquaniti, "Invariant Characteristics of a Pointing Movement in Man," *The Journal of Neuroscience,* vol. 1, pp. 710-720, 1981.

[100] F. Lacquaniti and J. F. Soechting, "Coordination of Arm and Wrist Motion During a Reaching Task," *The Journal of Neuroscience,* vol. 2, pp. 399-408, 1982.

[101] J. F. Soechting and M. Flanders, "Sensorimotor representations for pointing to targets in three-dimensional space," *Journal of Neurophysiology,* vol. 62, pp. 582-594, 1989.

[102] J. F. Soechting and M. Flanders, "Errors in Pointing are Due to Approximations in Sensorimotor Transformations," *Journal of Neurophysiology,* vol. 62, pp. 595-608, 1989.

[103] J. F. Soechting, S. I. H. Tillery, and M. Flanders, "Transformation from Head-to Shoulder-Centered Representation of Target Direction in Arm Movements," *Journal of Cognitive Neuroscience,* vol. 2, pp. 32-43, 1989.

[104] Y. Uno, M. kawato, and R. Suzuki, "Formation and Control of Optimal Trajectory in Human Multijoint Arm Movement," *Biological Cybernetics,* vol. 61, pp. 89-101, 1989.

[105] P. Haggard and J. Richardson, "Spatial Patterns in the Control of Human Arm Movement," *Journal of Experimental Psychology: Human Perception and Performance,* vol. 22, pp. 42-62, 1996.

[106] C. G. Atkeson and J. M. Hollerbach, "Kinematic Features of Unrestrained Vertical Arm Movements," *The Journal of Neuroscience,* vol. 5, pp. 2318-2330, 1985.

[107] M. D. K. Breteler, S. C. A. M. Gielen, and R. G. J. Meulenbroek, "End-Point Constraints in Aiming Movements: Effects of Approach Angle and Speed," *Biological Cybernetics,* vol. 85, pp. 65-75, 2001.

[108] J. M. Hollerbach, S. P. Moore, and C. G. Atkeson, "Workspace Effect in Arm Movement Kinematics Derived by Joint Interpolation," in *Motor Cotrol*, G. N. Gantchev, B. Dimitrov, and P. Gatev, Eds., ed New York: Plenum Publishing Corporation, 1987, pp. 197-208.

[109] M. D. K. Breteler, R. G. J. Meulenbroek, and C. C. A. M. Gielen, "An Evaluation of the Minimum-Jerk and Minimum Torque-Change Principles at the Path, Trajectory, and Movement-Cost Level," *Motor Control,* vol. 6, pp. 69-83, 2002.

[110] A. P. Georgopoulos, "Spatial Coding of Visually Guided Arm Movements in Primate Motor Cortex," *Cannadian Journal of Physiology and Pharmacology,* vol. 66, pp. 518-526, 1988.

[111] R. Caminiti, P. B. Johnson, Y. Burnod, C. Galli, and S. Ferraina, "Shift of Preferred Directions of Premotor Cortical Cells with Arm Movements Performed Across the Workspace," *Experimental Brain Research,* vol. 83, pp. 228-232, 1990.

[112] R. Caminiti, P. B. Johnson, and A. Urbano, "Making Arm Movements Within Different Parts of Space: Dynamic Aspects in the Primate Motor Cortex," *Journal of Neuroscience,* vol. 10, pp. 2039-2058, 1990.

[113] R. Caminiti, P. B. Johnson, C. GAlli, S. Ferraina, and Y. Burnod, "Making Arm Movements Within Different Parts of Space: the Premotor and Motor Cortical Representation of a Coordinate System for Reaching to Visual Targets," *Journal of Neuroscience,* vol. 11, pp. 1182-1197, 1991.

[114] J. F. Kalaska, "The Representation of Arm Movements in Postcentral and Parietal Cortex," *Cannadian Journal of Physiology and Pharmacology,* vol. 66, pp. 455-463, 1988.

[115] J. J. Craig, *Introduction to Robotics, Mechanics and Control*, 3 ed.: Prentice Hall, 2004.

[116] M. Kawato, "Internal models for motor control and trajectory planning," *Current opinion in neurobiology,* vol. 9, pp. 718-727, 1999.

[117] L. E. Brown, D. A. Rosenbaum, and R. L. Sainburg, "Limb position drift: implications for control of posture and movement," *Journal of Neurophysiology,* vol. 90, pp. 3105-3118, 2003.

[118] J. S. Baizer, I. Kralj-Hans, and M. Glickstein, "Cerebellar lesions and prism adaptation in macaque monkeys," *Journal of neurophysiology,* vol. 81, pp. 1960-1965, 1999.

[119] S. J. Blakemore, D. M. Wolpert, and C. D. Frith, "Central cancellation of self-produced tickle sensation," *Nature neuroscience,* vol. 1, pp. 635-640, 1998.

[120] H. Imamizu, S. Miyauchi, T. Tamada, Y. Sasaki, R. Takino, B. Putz*, et al.*, "Human cerebellar activity reflecting an acquired internal model of a new tool," *Nature,* vol. 403, p. 192, 2000.

[121] R. Miall, J. Keating, M. Malkmus, and W. Thach, "Purkinje cell complex spikes are predicted by simple spike activity," *Nat. Neurosci,* 1998.

[122] F. Campos and J. Calado, "Approaches to human arm movement control—A review," *Annual reviews in control,* vol. 33, pp. 69-77, 2009.

[123] P. Viviani and C. Terzuolo, "Trajectory determines movement dynamics," *Neuroscience,* vol. 7, pp. 431-437, 1982.

[124] F. Lacquaniti, C. Terzuolo, and P. Viviani, "The law relating the kinematic and figural aspects of drawing movements," *Acta psychologica,* vol. 54, pp. 115-130, 1983.

[125] P. M. Fitts, "The information capacity of the human motor system in controlling the amplitude of movement," *Journal of experimental psychology,* vol. 47, p. 381, 1954.

[126] S. E. Engelbrecht, "Minimum principles in motor control," *Journal of Mathematical Psychology,* vol. 45, pp. 497-542, 2001.

[127] T. Flash and N. Hogan, "The Coordination of Arm Movements: An Experimentally Confirmed Mathematical Model," *The Journal of Neuroscience,* vol. 5, pp. 1688-1703, 1985.

[128] A. Datas, P. Chiron, and J.-Y. Fourquet, "On Geodesic Paths and Least-Cost Motions for Human-Like Tasks," in *IEEE International Conference on Robotics and Biomimetics*, 2010, pp. 1025-1031.

[129] E. Nakano, H. Imamizu, R. Osu, Y. Uno, H. Gomi, T. Yoshioka*, et al.*, "Quantitative examinations of internal representations for arm trajectory planning: minimum commanded torque change model," *Journal of Neurophysiology,* vol. 81, pp. 2140-2155, 1999.

[130] M. Dornay, Y. Uno, M. Kawato, and R. Suzuki, "Minimum muscle-tension change trajectories predicted by using a 17-muscle model of the monkey's arm," *Journal of Motor Behavior,* vol. 28, pp. 83-100, 1996.

[131] T. Kang, J. He, and S. I. H. Tillery, "Determining natural arm configuration along a reaching trajectory," *Experimental Brain Research,* vol. 167, pp. 352-361, 2005.

[132] H. Kim, L. M. Miller, N. Byl, G. Abrams, and J. Rosen, "Redundancy resolution of the human arm and an upper limb exoskeleton," *Biomedical Engineering, IEEE Transactions on,* vol. 59, pp. 1770-1779, 2012.

[133] B. Kashi, M. Brand, J. Rosen, and I. Avrahami, "Synthesizing two criteria for redundancy resolution of human arm in point tasks," 2011, pp. 63-68.

[134] J. Yang, R. T. Marler, H. Kim, J. Arora, and K. Abdel-Malek, "Multi-objective optimization for upper body posture prediction," in *10th AIAA/ISSMO multidisciplinary analysis and optimization conference*, 2004.

[135] V. Pareto, *Cours d'economie politique*: Librairie Droz, 1964.

[136] C. M. Harris and D. M. Wolpert, "Signal-dependent noise determines motor planning," *Nature,* vol. 394, pp. 780-784, 1998.

[137] E. Todorov and M. I. Jordan, "Optimal feedback control as a theory of motor coordination," *Nature neuroscience,* vol. 5, pp. 1226-1235, 2002.

[138] A. M. Zanchettin, P. Rocco, L. Bascetta, I. Symeonidis, and S. Peldschus, "Kinematic analysis and synthesis of the human arm motion during a manipulation task," in *Robotics and Automation (ICRA), 2011 IEEE International Conference on*, 2011, pp. 2692-2697.

[139] S. Kim, C. H. Kim, and J. H. Park, "Human-like arm motion generation for humanoid robots using motion capture database," in *Intelligent Robots and Systems, 2006 IEEE/RSJ International Conference on*, 2006, pp. 3486-3491.

[140] P. K. Artemiadis, P. T. Katsiaris, and K. J. Kyriakopoulos, "A biomimetic approach to inverse kinematics for a redundant robot arm," *Autonomous Robots,* vol. 29, pp. 293-308, 2010.

[141] D. Bullock, S. Grossberg, and F. H. Guenther, "A self-organizing neural model of motor equivalent reaching and tool use by a multijoint arm," *Journal of Cognitive Neuroscience,* vol. 5, pp. 408-435, 1993.

[142] D. A. Rosenbaum, L. D. Loukopoulos, R. G. Meulenbroek, J. Vaughan, and S. E. Engelbrecht, "Planning reaches by evaluating stored postures," *Psychological review,* vol. 102, pp. 28-66, 1995.

[143] E. Saltzman and J. Kelso, "Skilled actions: A task-dynamic approach," *Psychological Review,* vol. 94, p. 84, 1987.

[144] F. M. Ivaldi, P. Morasso, and R. Zaccaria, "Kinematic networks," *Biological Cybernetics,* vol. 60, pp. 1-16, 1988.

[145] H. Moon, N. Hoang, N. P. Robson, and R. Langari, "Human arm motion planning against a joint constraint," in *Biomedical Robotics and Biomechatronics (BioRob), 2012 4th IEEE RAS & EMBS International Conference on*, 2012, pp. 401-406.

[146] H. Moon, N. P. Robson, R. Langari, and S. Shin, "An experimental study on redundancy resolution scheme of postural configuration in human arm reaching with an elbow joint kinematic constraint," in *Biomedical Engineering (MECBME), 2014 Middle East Conference on*, 2014, pp. 257-260.

[147] J. M. Hollerbach, "Optimum Kinematic Design for a Seven Degree of Freedom Manipulator," in *Robotics Research: the Second International Symposium*, H. Hanafusa and H. Inoue, Eds., ed Cambridge: MIT, 1985, pp. 215-222.

[148] X. Wang, "Three-Dimensional Kinematic Analysis of Influence of Hand Orientation and Joint Limits on the Control of Arm Postures and Movements," *Biological Cybernetics,* vol. 80, pp. 449-463, 1999.

[149] J. M. Hollerbach, "Optimum kinematic design for a seven degree of freedom manipulator," in *Robotics Research: The Second International Symposium*, 1985, pp. 215-222.

[150] J. Denavit, "A kinematic notation for lower-pair mechanisms based on matrices," *Trans. of the ASME. Journal of Applied Mechanics,* vol. 22, pp. 215-221, 1955.

[151] J. L. Pons, *Wearable robots: biomechatronic exoskeletons* vol. 70: Wiley Online Library, 2008.

[152] Q. Fu, J. Suarez, and T. Ebner, "Neuronal specification of direction and distance during reaching movements in the superior precentral premotor area and primary motor cortex of monkeys," *Journal of Neurophysiology,* vol. 70, pp. 2097-2116, 1993.

[153] J. Soechting and F. Lacquaniti, "Invariant characteristics of a pointing movement in man," *The Journal of Neuroscience,* vol. 1, pp. 710-720, 1981.

[154] M. Flanders and J. F. Soechting, "Parcellation of sensorimotor transformations for arm movements," *The Journal of Neuroscience,* vol. 10, pp. 2420-2427, 1990.

[155] O. Khatib, "A unified approach for motion and force control of robot manipulators: The operational space formulation," *Robotics and Automation, IEEE Journal of,* vol. 3, pp. 43-53, 1987.

[156] A. Biess, T. Flash, and D. G. Liebermann, "Riemannian Geometric Approach to Human Arm Dynamics, Movement Optimization, and Invariance," *Physical Review E,* vol. 83, p. 031927, 2011.

[157] E. Todorov and M. I. Jordan, "Smoothness maximization along a predefined path accurately predicts the speed profiles of complex arm movements," *Journal of Neurophysiology,* vol. 80, pp. 696-714, 1998.

[158] E. Todorov. (July 2013). *Movement Control Laboratory, University of Washington*. Available: http://homes.cs.washington.edu/~todorov/

[159] F. E. Pollick, U. Maoz, A. A. Handzel, P. J. Giblin, G. Sapiro, and T. Flash, "Three-dimensional arm movements at constant equi-affine speed," *Cortex,* vol. 45, pp. 325-339, 2009.

[160] J. Oprea, *Differential geometry and its applications*: MAA, 2007.

[161] J. E. Richardson and T. Flash, "Comparing Smooth Arm Movements with the Two-Thirds Power Law and the Related Segemented-Control Hypothesis," *The Journal of Neuroscience,* vol. 22, pp. 8201-8211, 2002.

[162] E. Rimon and J. W. Burdick, "A configuration space analysis of bodies in contact—I. 1st order mobility," *Mechanism and machine theory,* vol. 30, pp. 897-912, 1995.

[163] E. Rimon and J. W. Burdick, "A configuration space analysis of bodies in contact—II. 2ND order mobility," *Mechanism and machine theory,* vol. 30, pp. 913-928, 1995.

[164] N. P. Robson and J. M. McCarthy, "Kinematic Synthesis with Contact Direction and Curvature Constraints on the Workpiece," in *ASME International Design Engineering Technical Conferences (IDETC/MECH)*, Las Vegas, Nevada, 2007, pp. 581-588.

[165] N. Robson and A. Tolety, "Geometric Design of Spherical Serial Chains With Curvature Constraints in the Environment," in *ASME International Design Engineering Technical Conferences & Computers and Information in Engineering Conference (IDETC/CIE)*, 2011.

[166] K. Z. Graham, E. J. Mackenzie, P. L. Ephraim, T. G. Travision, and R. Brookmeyer, "Estimating the Prevalence of Limb Loss in the United States: 2005 to 2050," *Achieves of Physical Medicine and Rehabilitation,* vol. 89, pp. 422-429, 2008.

[167] T. R. Dillingham, L. E. Pezzin, and E. J. Mackenzie, "Limb Amputation and Limb Deficiency," *Southern Medical Journal,* vol. 95, pp. 875-883, 2002.

[168] A. Leland and M. Oboroceanu, "American War and Military Operations Casualties: List and Statistics," Congressional Research Service2010.

[169] R. H. M. III, "History of Arm Amputation, Prosthetic Restoration, and Arm Amputation Rehabilitation," in *In Functional Restoration of Adults and Children*

with Upper-Extremity Amputation, R. H. M. III and D. H. Atkins, Eds., ed New York: Demos Medical Publishing, Inc., 2004.

[170] A. B. Willson, "History of Amputation Surgery and Prosthetics," in *Atlas of Limb Prosthetics: Surgical, Prosthetic, and Rehabilitation Principles*, J. H. Bowker and J. W. Michael, Eds., ed St. Louis: Mosby, 1992.

[171] A. Muzumdar, *Powered Upper Limb Prostheses: Control, Implementation and Clinical Application*: Springer, 2004.

[172] A. E. Kobrinski, S. V. Bolhovitin, L. M. Voskoboinikova, D. M. Ioffe, E. P. Polyan, B. P. Popov*, et al.*, "Problems of Bioelectric Control," presented at the International Congress of the International Federation of Automatic and Remote Control (IFAC), 1960.

[173] E. D. Sherman, "A Russian Bioelectric-Controlled Prosthesis: Report of a Research Team from the Rehabilitation Institute of Montreal," *Canadian Medical Association Journal,* vol. 91, pp. 1268-1270, 1964.

[174] T. Kuiken, "Targeted Reinnervation for Improved Prosthetic Function," *Physical Medicine and Rehabilitation Clinics of North America,* vol. 17, pp. 1-13, 2006.

[175] J. B. Hijjawi, T. A. Kuien, R. D. Lipschutz, L. A. Miller, K. A. Stubblefield, and G. A. Dumanian, "Improved Myoelectric Prosthesis Control Accomplished Using Multiple Nerve Transfers," *Plastic and Reconstructive Surgery,* vol. 118, pp. 1573-1578, 2006.

[176] L. A. Miller, K. A. Stubblefield, R. D. Lipschutz, B. A. Lock, and T. A. Kuiken, "Improved Myoelectric Prosthesis Control Using Targeted Reinnervation Surgery:

A Case Series," *IEEE Transactions on Neural Systems and Rehabilitation Engineering,* vol. 16, pp. 46-50, 2008.

[177] A. P. Georgopoulos, J. F. Kalaska, R. Caminiti, and J. T. Massey, "On the Relations Between the Direction of Two-Dimensional Arm Movements and Cell Discharge in Primate Motor Cortex," *The Journal of Neuroscience,* vol. 2, pp. 1527-1537, 1982.

[178] J. Wessberg, C. R. Stambaugh, J. D. Kralik, P. D. Beck, M. Laubach, J. K. Chapin*, et al.*, "Real-time Prediction of Hand Trajectory by Ensembles of Cortical Neurons in Primates," *Nature,* vol. 408, pp. 361-365, 2000.

[179] M. Velliste, S. Perel, M. C. Spalding, A. S. Whitford, and A. V. Schwartz, "Cortical Control of a Prosthetic Arm for Self-Feeding," *Nature,* vol. 453, pp. 1098-1101, 2008.

[180] D. R. Kipke, W. Shain, G. Buzsaki, E. Fetz, J. M. Henderson, J. F. Hetke*, et al.*, "Advanced Neurotechnologies for Chronic Neural Interfaces: New Horizons and Clinical Opportunities," *The Journal of Neuroscience,* vol. 28, pp. 11830-11838, 2008.

[181] J. M. Rosenow, M. Stanton-Hicks, A. R. Rezai, and J. M. Henderson, "Failure Modes of Spinal Cord Stimulation Hardware," *Journal of Neurosurgery: Spine,* vol. 5, pp. 183-190, 2006.

[182] R. M. Rothschild, "Neuroengineering Tools/Applications for Bidirectional Interfaces, Brain-Computer Interfaces, and Neuroprosthetic Implants - a Review of Recent Progress," *Frontiers in Neuroengineering,* vol. 3, 2010.

[183] A. B. Ajiboye and R. F. Wier, "A Heuristic Fuzzy Logic Approach to EMG Pattern Recognition for Multifunctional Prosthesis Control," *IEEE Transactions on Neural Systems and Rehabilitation Engineering,* vol. 13, pp. 280-291, 2005.

[184] A. D. Chan and L. B. Englehart, "Continuous Myoelectric Control for Powered Prostheses Using Hidden Markov Models," *IEEE Transactions on Biomedical Engineering,* vol. 52, pp. 121-124, 2005.

[185] F. H. Chan, Y. Yang, F. K. Lam, Y. Zhang, and P. A. Parker, "Fuzzy EMG Classification for Prosthesis Control," *IEEE Transactions on Rehabilitation Engineering,* vol. 8, pp. 305-311, 2000.

[186] K. Ito, M. Tsukamoto, and T. Kondo, "Discrimination of Intended Movements Based on Nonstationary EMG for a Prosthetic Hand Control," presented at the International Symposium on Communications, Control and Signal Processing (ISCCSP), 2008.

[187] R. Kato, T. Fujita, H. Yokoi, and T. Arai, "Adaptable EMG Prosthetic Hand Using On-line Learning Method - Investigation of Mutual Adaptation Between Human and Adaptable Machine," presented at the IEEE International Symposium on Robots and Human Interactive Communication (RO-MAN), 2006.

[188] A. Soares, A. Andrade, E. Lamounier, and R. Carrijo, "The Development of a Virtual Myoelectric Prosthesis Controlled by an EMG Pattern Recognition System Based on Neural Networks," *Journal of Intelligent Information Systems,* vol. 21, pp. 127-141, 2003.

[189] J. Zhao, Z. Xie, L. Jiang, H. Cai, H. Kiu, and G. Hirzinger, "EMG Control for a Five-Fingered Prosthetic Hand Based on Wavelet Transform and Autoregressive Model," 2006.

[190] M. Khezri and M. Jahed, "Real-time Intelligent Pattern Recognition Algorithm for Surface EMG Signals," *Biomedical Engineering OnLine,* vol. 6, 2007.

[191] H. Huang, Y. Liu, and C. Wong, "Automatic EMG Feature Evaluation for Controlling a Prosthetic Hand Using a Supervised Feature Mining Method: An Intelligent Approach," presented at the IEEE International Conference on Robotics and Automation (ICRA), 2003.

[192] R. R. Kaliki, R. Davoodi, and G. E. Loeb, "Prediction of Elbow Trajectory from Shoulder Angles Using Neural Networks," *International Journal of Computational Intelligence and Applications,* vol. 7, pp. 333-349, 2008.

[193] R. R. Kaliki, R. Davoodi, and G. E. Loeb, "Prediction of Distal Arm Posture in 3-D Space from Shoulder Movements for Control of Upper Limb Prostheses," *Proceedings of the IEEE,* vol. 96, pp. 1217-1225, 2008.

[194] W. Abbott and A. Faisal, "Ultra-low-cost 3D gaze estimation: an intuitive high information throughput compliment to direct brain–machine interfaces," *Journal of neural engineering,* vol. 9, p. 046016, 2012.